Study on the optical properties of metal-dielectric nanocomposite materials induced by laser

van Doan Le

N°d'ordre NNT : 2023STET026

THÈSE de DOCTORAT
DE L'UNIVERSITÉ JEAN MONNET SAINT-ÉTIENNE

Membre de l'Université de LYON

École Doctorale N° 488
Science Ingénierie Santé
Spécialité / discipline de doctorat :
Optique & Photonique

Soutenue publiquement 22/09/2023**, par :**
Van Doan Le

Study on the optical properties of metal-dielectric nanocomposite materials induced by laser

Devant le jury composé de :

Davy Gerard	Professor, UTT, France	Reviewer
Kevin Vynck	CNRS researcher, ILM, France	Reviewer
Béatrice Dagens	CNRS researcher, Université Paris-Sud 11, France	Examiner
Mathieu Hébert	Professor, UJM, France	Examiner
Nathalie Destouches	Professor, UJM, France	Supervisor
Myriam Zerrad	Resercher, Institut Fresnel, France	Co-supervisor
Nicolas Dalloz	Innovation engineer, HID global, France	Invite

Contents

Acknowledgements

The successful completion of this thesis could not have been achieved without the invaluable contributions and supports from countless individuals, who have aided me along the way. Firstly, I would like to thank my supervisor Nathalie Destouches, who has guided my works with great dedication and insightful guidance, fostering an intellectual environment and pushing me to explore new horizons in my research. Nathalie: Thank you for accepting me in the group and gave me many opportunities to work in a broad range of fields, allowing me to enhance and broaden my knowledges as well as skills. It was a great learning experience for me in the past few years. I would like to extend my gratitude to my co-supervisor, Myriam Zerrad, for selecting me for this position.

Being a part of metallic nanoparticles team, I had been lucky to work and interact with great peoples: Dr. Christophe Hubert, Prof. Francis Vocanson, Dr. Hongfeng Ma, Dr. Nicolas Dalloz, Dr. Balint Eles, Dr. Manuel Figueroa, Thibault Girardin, Robin Mermillod-Blondin. Without your input and comments, my works could have not been completed.

I am indebted to Dr. Amos Egel for your invaluable assistance in utilizing your open source code, which play a pivotal role in my thesis. Additionally, I am deeply thankful to Thomas Gautrais, who constantly supported me solving technical problems while using the simulation code on the server and Arnaud Meyer for your wonderful help in using Zemax.

I would like also acknowledge Yaya Lefkir, Stephanie Reynaud for their contributions to sample characterizations and equipment training. Special thanks go to Jean-Yves Michalon, Anthony Cazier for their mechanical supports, and to Julie Debiesse, Nathalie Peritore, Patrick Vincent for their administrative assistances. My gratitude also goes out to wonderful peoples for our interesting conversations and memorable time: Prof. Youcef Ouerdane, Dr. Huu Dat Nguyen, Arnaud Valour, Dr. Hugo Bruhier, Cédric Maron, Daiwei Zhang, Ilemona S Omeje, Ratish Rao, Dr. Vincenzo De Michele, Dr. Cosimo Campanella.

I also wanted to acknowledge French national research agency (ANR) for their financial support throughout this thesis.

Finally, my profoundest thanks to my parent, sisters and brother, whose unwavering love and support have been my anchor throughout this endeavor.

Abstract

Structural color arises from the interaction between light and nanostructured materials. The ability to control the structural colors of nanomaterials has generated significant interest in metasurface research due to their potential for a wide range of industrial applications, such as vision, display technologies, data encoding, and anti-counterfeiting. However, scaling up production presents a major challenge for customizing the metasurfaces. Laser-based techniques offer a potential approach to overcome such challenge owning to the simplicity, cost-effectiveness and scalability. Nonetheless, the laser-induced materials typically suffer from intrinsic imperfections, including variable particle sizes, imperfect organization, and different surface morphologies. The optical responses of the material are thus characterized by their statistical properties, making the researches in color properties challenging.

This thesis investigates the optical properties of mesoporous TiO_2 thin films impregnated with small silver particles deposited on glass substrates processed by lasers. The main objectives of this thesis are to understand how structural inhomogeneities affect the optical properties of the materials and the mechanisms that lead to different diffracted and dichroic properties arising from their statistical properties.

The thesis consists of five main parts. The first part presents the theoretical background, including the plasmonic resonance properties of silver particles under varying opto-geometrical parameters. The simulation method based on T-matrix and scattering matrix formalisms to solve the multiple scattering problem is also discussed. The second part presents the experimental techniques used in this thesis, including the preparation of sol-gel-based samples, laser printing experiments, and color characterization. The following three parts contain the main results of the thesis. Part 3 focuses on the study of dichroism arising from the coupling between plasmonic and photonic resonances excited within laser-structured films. It investigates how statistical properties affect simulation results and the influence of imperfections on the optical properties. Part 4 concentrates on the colored properties, diffraction, and dichroism of materials controlled by nanosecond laser pulses. The mechanisms by which certain samples exhibit diffraction, some show dichroism, while others exhibit both optical phenomena simultaneously, are also addressed. Finally, Part 5 examines

the diffraction properties of structures with three superimposed gratings induced by a continuous laser.

Introduction

Structural colors,[1–7] which result purely from the interaction between light and the nanostructures, are a promising alternative to other chemical-based coloration mechanisms because they are resistant to photobleaching and provide eco-friendly color expression. Physically, when light impinges on a structure, it is modified and reflected or transmitted at a certain visible wavelength range to our eyes, allowing us to see a specific color. One common way to achieve the modification is to use plasmonic materials to absorb specific wavelength of the incoming wave, which is due to the excitation of the coherent conduction electron of metallic particles known as plasmonic resonances, which is a foundation in the generation and control of plasmonic colors[2,8–11] These resonances enable precise tuning of optical properties by engineering the geometries, dimensions, compositions of nanostructures,[3,12,13] as depicted in Figure I.a-c.

When the plasmonic resonances confined around small nanoparticles, referred as localized surface plasmon resonances (LSPRs),[2,14–19] they possess the remarkable ability to confine light within subwavelength scales. This property contributes to the outstanding spatial resolution achieved by LSPR-based color materials.[20,21] On the other hand, when nanoparticles arrange in a ordered array, they can trigger diffracted waves. The hybridization between the LSPRs of individual nanoparticle with the photonic modes generated from the ordered array provides another mean to change the spectrum of the incoming light.[22,23] Another approach is to use dielectric layers incorporated with plasmonic resonators to generate structural colors, originating from several combination effect of optical mechanisms, such as absorption, reflection, transmission, or interference. [24,25]

Materials exhibiting plasmonic colors have gained considerable interest, primarily for their significant potential applicability in real world optical devices. In contrast to conventional color pigments added as chemical additives, these materials employ texturing methodologies to achieve the desired colors. Numerous studies on plasmonic colors have produced materials with fruitful color through diverse modes of observation, including transmission,[11,26] scattering[27,28] or reflection[29,30] modes.

What make this area even more intriguing is the dynamic modulation of colors filtered through plasmonic resonances, a subject that has attracted significant interest over the past few years,[31–36]

as shown in Figure I.d-i. Unlike static plasmonic colors, this dynamic approach allows for the encoding of multiple distinct colors in one single nanopixel.[37,38] This capability holds a great promise, especially as it aligns with the growing demand for innovative optical engineering like tunable displays or data encryption.

Despite extensive studies and many significant achievements in the field of coloration using plasmonic materials, producing such materials for large-scale industrial applications remains challenging, with a need for low-cost mass production. To this end, laser-based techniques are appeared as a great candidate because they are simple, inexpensive and scalable (Figure I.j-k). In fact, laser-empowered color generations have achieved great success in recent years.[39–42] Laser can induce several mechanisms that modify material morphologies, supporting a wide range optical properties. Different color appearances can be generated depending on particle size, shape and organization, which can be easily directed by laser at different exposure conditions.[42–44] Laser can also trigger self-organization processes,[45–47] enabling grating formations whose period and orientation are tuned by laser wavelength and polarization. These emerging self-organizations can act as diffraction gratings at specific visible wavelength or can give rise to dichroism. Exploiting these diffractive or dichroic properties of plasmonic metamaterials can pave the way for the future development of optical components with high-end applications. Recently, laser-generated plasmonic gratings have demonstrated the ability to hide several diffractive images that can be revealed at different observation angles,[48] or random plasmonic metamaterials induced by laser have been implemented for multiple image multiplexing in a single metasurface,[37,38] with some multiplexed images exploiting the dichroic property. The materials in these studies are characterized by their statistical properties, where laser beam modifies several parameters simultaneously, producing some kind of random metasurfaces with certain size distribution, particle density and organizations. This makes it extremely difficult to do research on the optical properties of these materials. Despite significant efforts to unveil many physical mechanisms of the plasmonic metasurface under the laser illumination, such as the growth and reshaping of metallic particles,[49–51] self-organization processes[52,53] or the link between optical properties and laser processing parameters using machine learning,[54] many questions remain unclear. The latter includes the following questions: how do the characterized size of metasurface, spatial disorders and size distribution affect the overall optical properties of the materials? From the statistical

property of the real sample, how one can unfold the origin of diffraction or dichroism? What are the mechanisms that lead some samples to exhibit both diffraction and dichroism, only dichroism or only diffraction and what are the impacts of the opto-structural parameters on the non-diffractive and non-dichroic colors?

The primary goal of this thesis is to answer above questions in order to gain a deeper understanding on the relation between laser parameters, the induced nanostructures and the resulting optical properties, which can open the door to mass production of optical devices with desirable functionalities. To seek for the answers, we organize the thesis into six chapters. Chapter 1 will present the theoretical background of the studies, including the introduction and physical properties of plasmonic materials, the electromagnetic simulations method that employs T-matrix method and scattering matrix formalism to solve the multiple scattering problem of spherical nanoparticles embedded in thin film layers, and the optical properties of metallic particles with the influence of opto-geometrical parameters. Chapter 2 will introduce the experimental techniques that are used to produced samples. The sample preparation process will be first presented. Continuous (cw) and nanosecond (ns) laser set-ups with be then discussed. And finally, we will explain how the lasers can be used to print plasmonic images. The third chapter will be dedicated to study the hybridization between plasmonic and photonic resonances, occurring in self-organized nanoparticle arrays buried in dielectric thin film. The questions of how the sample inhomogeneities influence the optical behaviors will be answered. By comparing simulation results of real-like and regular samples, the origin of sample dichroism is also revealed. Chapter 4 further explores the physical mechanisms underlying the diffractive and dichroic properties of samples induced by nanosecond laser, where coupling between near-field and farfield contribute to the varying diffractive and dichroic properties of the metasurfaces. At the end of this chapter, we print realistic color images observed in different modes to demonstrate the potential of the laser-based approach in mass production for display or security purposes. In the fifth chapter, interesting asymmetric and circular diffractive behaviors of three superimposed grating structures generated by cw laser will be presented. Finally, I will conclude the thesis and discuss the possible research that can be a continuation of this work.

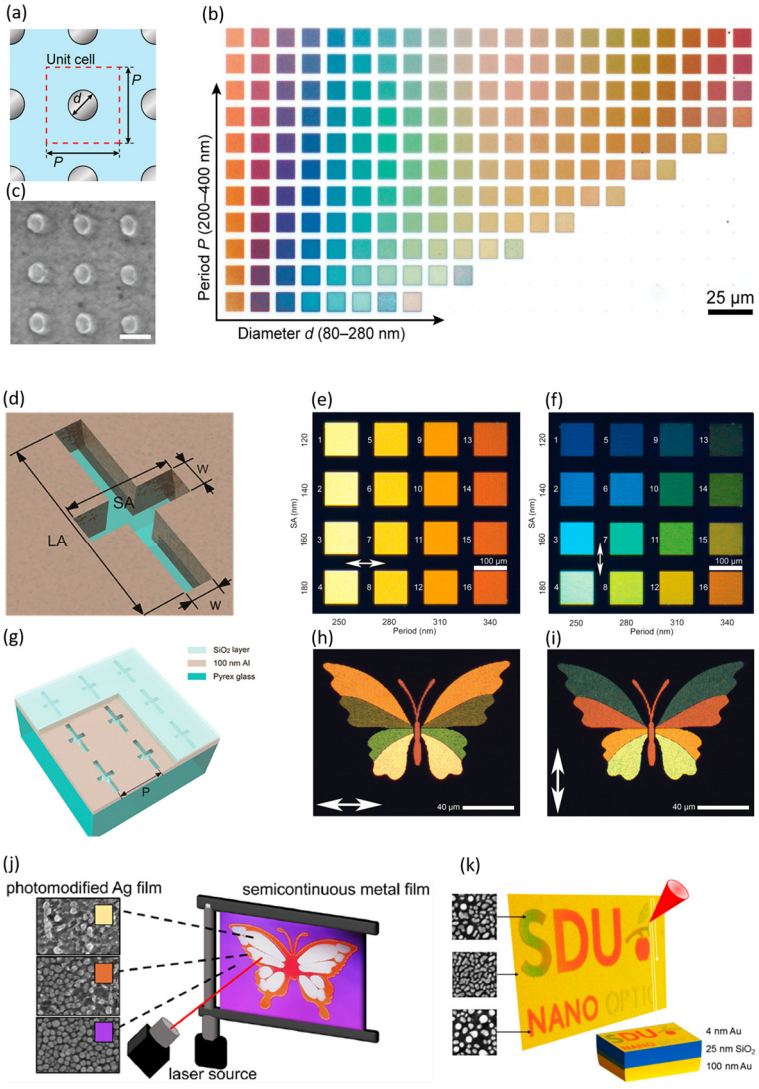

Figure I.(a) Illustration depicted the top view of aluminum nanodisks positioned on an aluminum film coated with aluminum oxide. (b) Scanning electron microscope (SEM) images of nanodisks with an 80 nm diameter and a 300 nm spacing. The scale bar is 200 nm. (c) Color pallets of the nanodisk arrays with diameters, ranging from 80 to 280 nm in 10 nm intervals, and periods varying from 200 to 400 nm in 20 nm increments. The image was captured using a 20x objective (NA = 0.45) under unpolarized white light illumination.[55] (d, g) Schematics of cross-shaped aperture with w = 30 ± 2 nm, P = 340 nm, SA = 120 ± 5 nm and LA = 203 ± 3 nm. (b, f) Color pallet obtained in transmission mode with polarization parallel and perpendicular to SA respectively. (h, i) Micrographs of butterfly with different colors observed under different incident polarizations.[36] (j) Illustration of plasmonic color printing using femtosecond laser on semicontinuous silver films.[56] (k) Illustration of high-resolution laser printing of structural colors of metal films atop dielectric-metal sandwiches.[44]

1 Theoretical Background

In this chapter the concept of plasmonic resonance will be introduced, with the focus on Drude model for dielectric function, the concept of localized surface plasmon resonance, introduction of quasi-static approximation and Mie theory for single sphere particle. The chapter continues by presenting the modeling method for scattering problem of metallic particles based on T-matrix method incorporating with scattering matrix formalism. Finally, it will end with the study on the optical properties of plasmonic nanoparticles under influences of several opto-geometrical parameters and an introduction of coupling between LSPRs with photonic modes arising from diffracted waves of ordered NPs array.

1.1 Introduction of Plasmonics

Plasmonics is a promising field that exploits the collective motion of charge carriers at the interface between a dielectric and a metal under the interaction with electromagnetic fields. Such collective oscillation is either surface plasmon polariton (SPP), when propagating along the interface or localized surface plasmon resonance (LSPR), when localized on a nanostructure. The excitation of plasmons can lead to strong enhancement of electromagnetic field at nanoscale allowing to generate novel optical effects, which can be potential for many applications ranging from chemistry,[57] energy,[58] to structural coloration.[2,8,13] Actually, the use of plasmonic materials can be traced back centuries, when stained glass windows in many churches or Roman Lycurgus cup were used thanks to their vibrant color appearances, which were achieved by doping the materials with gold or silver particles. However, the underlying physics of optical effects can only be revealed beginning with Gustav Mie's work in 1908, where he solved Maxwell's equations to find the scattering and absorption of spherical particles.

To understand the interaction between light and the metallic particles at nanoscale, one must understand the interaction between light and electrons. Lorentz and Drude proposed models to describe the motions of electrons exerted by external electric force. While the Lorentz model takes into account the nature resonance of electrons, which are bound to a nucleus, the Drude model

considers the motion as free electron gas. Therefore, the latter will be used in this thesis to model the motion of electrons in a metallic nanoparticle and will be discussed further below.

1.1.1 The Drude model

The Drude model is introduced to explain the transport properties of electron in metals,[59,60] which is based on a classical representation of kinetic theory. It assumes gas molecules as solid spheres with negative charges that move freely against immobile metallic ions with positive charges. The models neglect the interaction between electrons and between electrons and ions. Instead the damping via collisions is characterized as collision frequency $1/\tau$, where τ is defined as the relaxation time.

Classically, the motion of a free electron gas can be modeled as a damped oscillator under the external electromagnetic field, which can be mathematically described as:

$$m_e \frac{\partial^2 \vec{x}(t)}{\partial t^2} + m_e \Gamma \frac{\partial \vec{x}(t)}{\partial t} = -e\vec{E}(t) \tag{1.1}$$

Where x is position, m_e is electron effective mass, Γ is the damping constant, $\vec{E}(t)$ is the external electromagnetic field. Using the harmonic time dependence forms of the electric field $\vec{E}(t) = E_0 e^{-i\omega t}$ and solving for solutions with $\vec{x}(t) = x_0 e^{-i\omega t}$, we arrive at

$$\vec{x}(\omega) = \frac{e}{m_e} \frac{\vec{E}(\omega)}{\omega^2 \mp j\omega\Gamma} \tag{1.2}$$

leading to the polarization of the material, which is defined as:

$$\vec{P}(\omega) = -ne\vec{x}(\omega) = -\frac{ne^2}{m_e} \frac{\vec{E}(\omega)}{\omega^2 + j\omega\Gamma} \tag{1.3}$$

with n is the number of electrons per unit volume. Under the applied electric field $\vec{E}$, the polarization can be rewritten as:

$$\vec{P}(\omega) = \epsilon_0 \chi(\omega) \vec{E}(\omega) \tag{1.4}$$

Where ϵ_0 is the permittivity of the vacuum and χ is the susceptibility of the material, which is equal to

$$\chi(\omega) = -\frac{ne^2}{\epsilon_0 m_e} \frac{1}{\omega^2 \mp j\omega\Gamma} \tag{1.5}$$

with the induced polarization $\vec{P}$, the dielectric displacement reads:

$$\begin{aligned} \vec{D} &= \epsilon_0 \vec{E} + \vec{P} \\ &= \epsilon_0 \vec{E} + \epsilon_0 \chi_e \vec{E} \\ &= \epsilon_0 (1 + \chi_e) \vec{E} \\ \vec{D} &= \epsilon_0 \epsilon \vec{E} \end{aligned} \tag{1.6}$$

Therefore, the dielectric function of the material becomes

$$\epsilon(\omega) = 1 - \frac{\omega_p^2}{\omega^2 + j\omega\Gamma} \tag{1.7}$$

Where $\omega_p = ne^2/\epsilon_0 m$ is the plasma frequency of the material. Rewrite equation (1.7) in term of the real and imaginary components, we arrive at:

$$\epsilon(\omega) = 1 - \left(\frac{\omega_p^2 \tau^2}{1 + \omega^2 \tau^2} \right) + j \left(\frac{\omega_p^2 \tau}{\omega(1 + \omega^2 \tau^2)} \right) \tag{1.8}$$

where τ is referred to the relaxation time, defined as $\tau = 1/\Gamma$.

Convert the permittivity to the refractive index (we neglect the magnetic response):

$$n + j\kappa = \sqrt{\epsilon} = \sqrt{\epsilon_1 + j\epsilon_2} \tag{1.9}$$

with n the refractive index and κ the extinction coefficient.

From equation (1.9):

$$\begin{aligned} \epsilon_1 &= n^2 - \kappa^2 \\ \epsilon_2 &= 2n\kappa \end{aligned} \tag{1.10}$$

and:

$$\begin{aligned} n &= \sqrt{\frac{|\epsilon| + \epsilon_1}{2}} \\ \kappa &= \sqrt{\frac{|\epsilon| - \epsilon_1}{2}} \end{aligned} \tag{1.11}$$

The Drude model presented above is adequate to describe the optical behavior of metals for photon energy within an electron band. However, when the photon energy exceeds the transition energy between electron bands, the Drude model becomes inadequate and can not fully describe the dielectric response of metals. Because the interband transition may occur in noble metals (e.g. gold, silver or copper), an additional parameter is needed to account for the physical process.[61]

1.1.2 Effect of the interband transitions

To take into account the effect of the interband transition, the dielectric function obtained from equation 1.8 can be modified as:[62]

$$\epsilon(\omega) = 1 + \chi_D(\omega) + \chi_{ib}(\omega) \tag{1.12}$$

in which, $\chi_D(\omega) = -\omega_P^2/(\omega^2 + j\omega\Gamma)$ is the susceptibility from the Drude model (as shown in equation 1.7) and $\chi_{ib}(\omega)$ is susceptibility accounted for the interband transition, which can be calculated either from electron band structure or using experimental data. We will present the latter

here, where Kramers-Kronig relations are used to connect the real part and imaginary part of χ_{ib}, implying that the real part can be calculated from the imaginary part and vice versa[63]

$$\chi_1(\omega) = \frac{2}{\pi} P \int_0^{\infty} \frac{\chi_2(\omega)}{\Omega^2 - \omega^2} d\Omega \tag{1.13}$$

$$\chi_2(\omega) = -\frac{2\omega}{\pi} P \int_0^{\infty} \frac{\chi_1(\omega)}{\Omega^2 - \omega^2} d\Omega \tag{1.14}$$

where P is the integral principal part. The real part (χ_1) corresponds to material polarization while the imaginary part (χ_2) represents energy dissipation, which can be deduced from the imaginary part of the material susceptibility obtained from experiment and of the susceptibility from Drude's model as the follows:

$$\chi_2^{ib}(\omega) = \begin{cases} \chi_2^{exp}(\omega) - \chi_2^{DS}(\omega), & \omega \geq \omega_{ib} \\ 0, & \omega < \omega_{ib} \end{cases} \tag{1.15}$$

with ω_{ib} is the threshold frequency of the interband transition. The real part of the susceptibility is then determined from the Kramers-Kroenig relations:

$$\chi_1^{ib}(\omega) = \lim_{\epsilon \to 0} \left[\frac{2}{\pi} \int_0^{\omega-\epsilon} \frac{\Omega \chi_2^{ib}(\omega)}{\Omega^2 - \omega^2} d\Omega + \frac{2}{\pi} \int_{\omega+\epsilon}^{\infty} \frac{\Omega \chi_2^{ib}(\omega)}{\Omega^2 - \omega^2} d\Omega \right] \tag{1.16}$$

1.1.3 Effects of size on damping rate

For really small particle (radius < 10 nm), additional damping process, can affect the width and the frequency of the resonance band, which is due to the scattering at the surface when the particle size is smaller than the electron mean free path. The damping rate is thus modified by[64]

$$\Gamma(R) = \Gamma_0 + A \frac{v_F}{R} \tag{1.17}$$

with Γ_0 is the damping constant resulting from the scattering of the excited electron with the ionic cores, which is independent to the particle size, $A \approx 1$ is a constant that relies on particle surface features,[65] v_F is the Fermi velocity ($v_F = 1.39 \times 10^6\ m/s$ for silver used in this thesis) and R is the particle radius. The second term in equation (1.19), which is proportional to v_F and $1/R$, indicates the damping rate caused by the scattering of oscillating electrons with the metal surface. Finally, the dielectric function can be generalized as

$$\epsilon(\omega, R) = 1 - \frac{\omega_p^2}{\omega^2 + j\omega\Gamma(\mathrm{R})} + \chi_{ib}(\omega) \tag{1.18}$$

1.1.4 Localized surface plasmon resonance

Plasmon resonances can be supported by metallic particles.[16,17] When an external electromagnetic field impinges on a metallic nanoparticle, it acts as a driving force to displace electrical charges away from its static cores. As the result, positive and negative charges are accumulated on the opposite sides of the particle (see Figure 1.3), inducing an electric field inside the particle with the opposite direction to the external field. The particle is thus polarized and exerts restoring force leading to the natural plasmonic oscillation of the particle. It is intuitive that, if the frequency of the external field matches with plasmonic frequency, the particle will oscillate maximally. For the noble metals, the resonance normally arises at visible wavelength and can be tuned easily by changing particle size, shape, organization, or dielectric medium. Therefore, LSPR-based applications are wildly used and will continue to grow in the future for vision-related applications.[2] To gain a deeper understanding of the underlying physics of LSPRs, it is crucial to quantify the optical properties of the metallic NPs, including scattering, absorption and extinction. To this end, the investigation begins with a simplified model that uses quasi-static approximation, then the Mie theory for the description of a spherical particle, and finally present a full analytical model of scattering problem of multiple spherical particles accompanied by a layered system. Despite not being used for calculating the optical responses, the approximation can provide useful interpretations for the optical behaviors of a metallic particle.

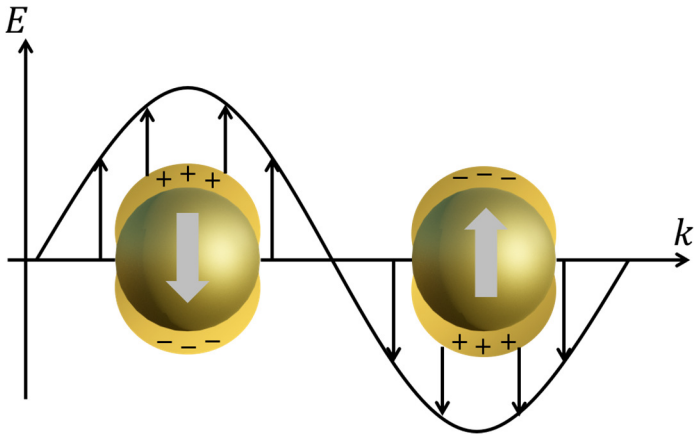

Figure 1.3 Excitation of localized surface plasmon resonance on metallic particles. White arrows depict the induced electric fields due to the displacement of electron charges in the presence of an external electromagnetic field

1.1.5 Quasi-static approximation

One of the simplest ways to gain insights into the LPSRs is to look at the resonance properties of a small nanoparticle using quasi-static approximation. In this regime, the electric field inside the particle is assumed to be in phase and the particle is treated as an oscillating dipole. With the approximation, the polarizability can be defined as:[63,66]

$$\alpha = 4\pi R^3 \frac{\epsilon - \epsilon_m}{\epsilon + 2\epsilon_m} \tag{1.19}$$

with ϵ, ϵ_m are the dielectric functions of the material and surrounding medium respectively. It is obvious from the equation 1.19 that the particle will resonate at the condition of minimum denominator, implying that $\epsilon = -2\epsilon_m$. To find the resonance wavelength, we can use the dielectric function derived from the Drude model as described in equation 1.7, which can be simplified for the visible wavelength range ($\omega \ll \omega_p$):

$$\epsilon = 1 - \frac{\omega_p^2}{\omega^2} \tag{1.20}$$

Using equation 1.20 and combining with the resonance condition ($\epsilon = -2\epsilon_m$), the frequency at the resonance peak is then:

$$\omega_{max} = \frac{\omega_p}{\sqrt{2\epsilon_m + 1}} \tag{1.21}$$

which can then lead to the wavelength at the peak:

$$\lambda_{max} = \lambda_p\sqrt{2\epsilon_m + 1} \tag{1.22}$$

with $\lambda_p = 2\pi c/\omega_p$. An interesting result that can be obtained from the equations is the dependence of the peak to the surrounding environment, where increasing the refractive index results in a redshift of the resonance.

Next, the scattering cross section and absorption cross section can be calculated as:[63]

$$C_{sca} = \frac{8\pi}{3} k^4 R^6 \left|\frac{\epsilon - \epsilon_m}{\epsilon + 2\epsilon_m}\right|^2 \tag{1.23}$$

$$C_{abs} = 4\pi k R^3 \mathrm{Im}\left[\frac{\epsilon - \epsilon_m}{\epsilon + 2\epsilon_m}\right] \tag{1.24}$$

leading to scattering and absorption efficiency:

$$Q_{sca} = \frac{8}{3} k^4 R^4 \left|\frac{\epsilon - \epsilon_m}{\epsilon + 2\epsilon_m}\right|^2 \tag{1.25}$$

$$Q_{abs} = 4kR \mathrm{Im}\left[\frac{\epsilon - \epsilon_m}{\epsilon + 2\epsilon_m}\right] \tag{1.26}$$

with k = $2\pi/\lambda$ and the efficiencies are determined by dividing the cross sections by πR^2. Theoretically, scattering is defined as part of incidence that changes direction without losing energy when impinging on a nanoparticle. Absorption, on the other hand, occurs when part of incident energy is absorbed and transferred to the particle. Extinction is thus the summation of absorption and scattering as they account for total energy removed from the incidence due to the

presence of the particle. Equations 1.25 & 1.26 suggest that small particles are dominated by the absorption efficiency over scattering efficiency.

1.1.6 Mie theory

However, the above approximation has a limitation in term of the influence of particle size on the optical properties, specifically the retardation effect of large particles. Mie theory,[67] on the other hand, provide a rigorous analytical description to solve Maxwell's equations that describes the optical properties of a spherical particle. According to the Mie solution, the scattering, extinction and absorption cross sections can be calculated as:[63]

$$C_{sca} = \frac{2\pi}{k^2}\sum_{n=1}^{\infty}(2n+1)(|a_n|^2 + |b_n|^2) \tag{1.27}$$

$$C_{ext} = \frac{2\pi}{k^2}\sum_{n=1}^{\infty}(2n+1)Re(a_n + b_n) \tag{1.28}$$

$$C_{abs} = C_{ext} - C_{sca} \tag{1.29}$$

where a_n, b_n are the parameters, consisted of the Riccati-Bessel functions, whose explicit expressions can be found in *Bohren and Huffman book*,[63] n is a multipolar coefficient, which $n = 1, 2, 3, ...$ represents the dipole, quadrupole, octupole,…respectively. Mathematically, Mie theory describes an expansion of scattered fields into a complete and orthogonal form of radiating vector spherical harmonics. In comparation to quasi-static approximation, Mie theory provides more information about the scattering properties of a single spherical particle, such as resonances due to the multipolar modes and the redshift as the particle size increases.[14,68] The latter is attributed to the weakening of restoring force when increasing particle size, which will be discussed further in section 1.3.

However, with a complex multiple scattering system incorporated with reflection from plane surfaces, the simple approximation or Mie theory are not adequate for the study of the optical behaviors. In that context, an expansion of Mie theory, accounting for multiple scattering, combines with the scattering matrix method for the multiple reflection problem is needed. To this

end, Amos Egel [69] have presented a full analytical description for the multiple scattering problem combined with layer system response, which will be synthesized as below.

1.2 Electromagnetic modeling of scattering by ensembles of particles in a layered system

This section will present a simulation framework that deals with scattering of multiple particles embedded in layered system. The framework is based on the expansion of T-matrix method for multiple scattering from spherical particles[70,71] and scattering matrix method for the layered system responses, which has already been described by Amos Egel and later translated to the free Python package *Smuthi.*[72] Throughout my thesis, I used this simulation method to calculate the optical responses of my materials, consisting of silver particles embedded in thin films. To be consistent, I will keep the same notations and symbols that Amos used, but I will skip some detailed descriptions that is unnecessary for my thesis. At the beginning of this part, the concept of plane waves and spherical vector wave function as well as their transformation and translation will be introduced (section 1.2.1). Then, section 1.2.2 describes the layered system responses by using transfer matrix method and scattering matrix method. The scattering problems of particles will be calculated using T-matrix method and its expansion to take into account multiple scattering shown in section 1.2.3 and 1.2.4 respectively. Finally, a brief introduction of *Smuthi* code will be presented in section 1.2.5.

1.2.1 Electromagnetic waves

It is assumed that the media in this study are linear, non-magnetic, piecewise homogeneous and isotropic. The section will be started by the definition of the Maxwell equations for electric and magnetic field and the constitutive relations.

$$\nabla \times \vec{E}(r,\omega) = i\omega\vec{B}(r,\omega) \tag{1.30}$$

$$\nabla \times \vec{H}(r,\omega) = -i\omega\vec{D}(r,\omega) + \vec{j}(r,\omega) \tag{1.31}$$

$$\tag{1.32}$$

$$\nabla \cdot \vec{D}(r,\omega) = \rho(r,\omega) \tag{1.33}$$

$$\nabla \cdot \vec{B}(r,\omega) = 0 \tag{1.34}$$

$$\vec{D}(r,\omega) = \epsilon_0 \epsilon_r \vec{E}(r,\omega) \tag{1.35}$$

$$\vec{B}(r,\omega) = \mu_0 \mu_r \vec{H}(r,\omega)$$

These equations show the relation of the electric displacement ($\vec{D}$), electric field ($\vec{E}$), magnetic field ($\vec{H}$), magnetic flux density ($\vec{B}$), external charges (ρ) and the current density ($\vec{j}$), in which ϵ_0, μ_0, ϵ_r, μ_r,are the vacuum and relative permittivity, permeability respectively, ω is angular frequency.

Combining equations (1.25, 1.26, 1.29 and 1.30) and assuming that electric and magnetic fields have the harmonic time dependence forms. The Helmholtz wave equations for the electric and magnetic fields can be then constructed as

$$\nabla \times \nabla \times \vec{E}(\vec{r}) - k^2 \vec{E}(\vec{r}) = i\omega\mu_0\mu_r \vec{j}(\vec{r}) \tag{1.36}$$

$$\nabla \cdot j\vec{E}(\vec{r}) = \frac{\rho(\vec{r})}{\epsilon_r \epsilon_0} \tag{1.37}$$

$$\vec{H}(\vec{r}) = \frac{1}{i\omega\mu_0\mu_r} \nabla \times \vec{E}(\vec{r}) \tag{1.38}$$

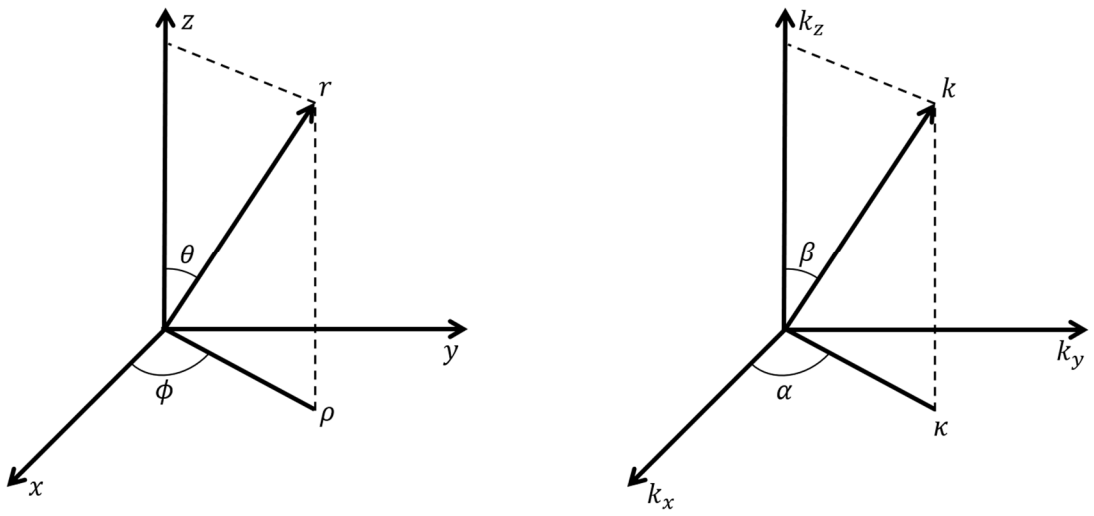

Figure 1.4. Cartesian (x, y, z), cylindrical (ρ, ϕ, z) and spherical (r, θ, ϕ) coordinates systems of vector $\vec{r}$ and the corresponding systems (k_x, k_y, k_z), (κ, α, k_z), (k, β, α) in reciprocal space.

Vector wave functions. The first step is to construct plane vector wave function (PVWFs) and the spherical vector wave functions (SVWFs), represented in different coordinate systems as shown in fig. 1.4, which are basis sets of solution from the Helmholtz equations. The PVWFs can be defined as

$$\overrightarrow{\Phi_j^{\pm}}(\kappa, \alpha; \vec{r}) = e^{ik_{\pm} \cdot r}\, \hat{e}_j^{\pm} \tag{1.39}$$

Note that the plus and minus signs correspond to waves propagated along the positive and negative direction of z-axis, respectively. The index j denotes the transversal electric waves (TE: j =1) and transversal magnetic waves (TM: j = 2), defined by the unit vector $\hat{e}_j$. The vector wave k is written in the cylindrical coordinates ($\kappa, \alpha, \pm k_z$) where κ is the in-plane component , the z-component of the wavevector reads:

$$k_z = \sqrt{k^2 - \kappa^2} \tag{1.40}$$

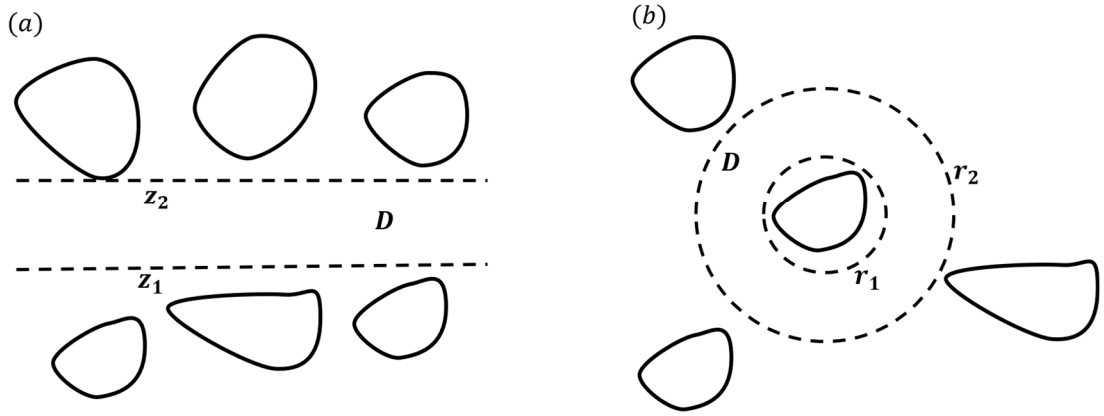

Figure 1.5. Sketch of homogeneous domain D bounded by two plane interfaces, which $D = \{r | z_1 \leq z \leq z_2\}$ with $-\infty \leq z_1 \leq z \leq z_2 \leq \infty$ (a) and two spherical interfaces, which $D = \{r | r_1 \leq r \leq r_2\}$ with $0 \leq r_1 \leq r_2 \leq \infty$ (b). Any electromagnetic fields can be expanded in plane waves (a) or spherical waves (b).

When the refractive index of medium is real and $\kappa \leq k$, the PVWFs are propagating waves in the positive z-direction. Whereas, when $\kappa > k$, k_z become imaginary, the PVWFs correspond to the evanescent waves.

In a homogeneous, source-free medium (D) bounded by two planes as illustrated in fig. 2a, there exist functions $g_1^{\pm}(\kappa, \alpha)$ and $g_2^{\pm}(\kappa, \alpha)$ such that any divergence-free field can be constructed from set of PVWFs that fulfills the Helmholtz equation:

$$\vec{E}(r) = \sum_{j=1}^{2} \int_{R^2} d^2\, k_{||} \left(g_j^{+}(\kappa, \alpha) \overrightarrow{\Phi_J^{+}}(\kappa, \alpha; r) \; + \; g_j^{-}(\kappa, \alpha) \overrightarrow{\Phi_J^{-}}(\kappa, \alpha; r) \right) \tag{1.41}$$

In equation (1.41), $d^2 k_{||}$ is equivalent to $dk_x dk_y$ in Cartesian coordinate or $d\kappa\, \kappa\, d\alpha$ in cylindrical coordinate.

Fig. 1.5b illustrates a domain D that is bounded by two spherical interfaces (r_1 and r_2). Similar to PVWFs, the SVWFs Ψ_{plm}^{v} can form a set of equations that fulfills the Helmholtz equation. The SVWFs[71] are defined as:

$$\overrightarrow{\Psi_{1lm}^{v}}(r) = \frac{1}{\sqrt{2l(l+1)}} z_l^v(kr) \left(im\pi_l^{|m|}(cos\theta)\hat{e}_\theta - \tau_l^{|m|}(cos\theta)\hat{e}_\phi \right) e^{im\phi} \tag{1.42}$$

$$\overrightarrow{\Psi_{2lm}^{v}}(r) = \frac{1}{\sqrt{2l(l+1)}} \left[\frac{z_l^v(kr)}{kr} l(l+1) P_l^{|m|}(cos\theta)\, \hat{e}_r + \frac{\partial_{kr}(krz_l^v(kr))}{kr} \left(\tau^{|m|}(cos\theta)\hat{e}_\theta - im\pi_l^{|m|}(cos\theta)\hat{e}_\phi \right) \right] e^{im\phi} \tag{1.43}$$

with $z_l^v(kr)$ denotes either spherical Bessel functions for the regular solutions ($v = 1$) or the spherical Hankel functions of first kind for the outgoing solutions ($v = 3$). The indices (plm) represent the polarization ($p = 1$: transverse electric field and $p = 2$: transverse magnetic field), multipole degree ($l = 1, \ldots, \infty$) and multipole order ($m = -l, \ldots, l$) respectively. $P_l^{|m|}(x)$ is the normalized Legendre's function:

$$P_l^m(x) = \sqrt{\frac{(2l+1)(l-m)!}{2(l+m)!}}(1-x^2)^{m/2}\frac{d^m P_l(x)}{dx^m} \tag{1.44}$$

where $P_l(x)$ is the l-th Legendre polynomial, and the angular functions are $\pi_l^m(cos\theta) = P_l^m(cos\theta)/sin\theta$ and $\tau_l^m(cos\theta) = dP_l^m(cos\theta)/d\theta$.

In the domain D defined in Figure 1.5, assumed to be homogeneous and source-free medium, bounded by two spherical interfaces-centered at $\vec{r} = 0$ of radii r_1 and r_2, any field can be expanded in the complete form:

$$\vec{E}(r) = \sum_{p=1}^{2}\sum_{l=1}^{\infty}\sum_{m=-l}^{l}(a_{plm}\overrightarrow{\psi_{plm}^{(1)}}(r) + b_{plm}\overrightarrow{\psi_{plm}^{(3)}}(r)) \tag{1.45}$$

Or

$$\vec{E}(r) = \sum_{n=1}^{\infty}(a_n\overrightarrow{\psi_n^{(1)}}(r) + b_n\overrightarrow{\psi_n^{(3)}}(r)) \tag{1.46}$$

with multi-index n represents plm, and a_n is the incoming field coefficient at a considered particle, which will be determined later in this thesis, and b_n is the outgoing field coefficient, which can be calculated from a_n using T-matrix method

Translations and transformations. As the scattering problem involves the interaction of electromagnetic fields with spherical and planar surfaces, it is important to transform and translate back and forth between SVWFs and PVWFs. Translations are also useful to express the field scattered by one particle in the coordinate system of another particle.

The translation of PVWFs corresponds to a phase shift ($\vec{d}$: displacement vector):

$$\overrightarrow{\Phi_J^{\pm}}(r+d) = e^{ik_{\pm}\cdot d}\overrightarrow{\Phi_J^{\pm}}(r) \tag{1.47}$$

While for SVWFs, the translation can be done using addition theorem:[73,74]

$$\overrightarrow{\psi_n^{(3)}}(r+d) = \sum_{n'} A_{nn'}(d)\overrightarrow{\psi_{n'}^{(1)}}(r) \quad for\ |r| < |d| \tag{1.48}$$

in which $A_{nn'}$ is composed of Wigner-3j symbols whose detailed formulas can be referred to Egel's thesis,[69] here I skip the tedious derivatives of the coefficients.

In addition, a PVWFs can be transformed into SVWFs as:

$$\overrightarrow{\psi_n^{(3)}}(r) = \frac{1}{2\pi}\sum_{j=1}^{2}\int_{R^2}\frac{d^2k_{||}}{k_z k}e^{im\alpha}B_{nj}\left(\frac{\pm k_z}{k}\right)\overrightarrow{\Phi_j^{\pm}}(\kappa,\alpha;r), \ \text{for z} \leqslant 0 \tag{1.49}$$

and SVWFs can be written in the form of PVWFs as:

$$\overrightarrow{\Phi_j^{\pm}}(\kappa,\alpha;r) = 4\sum_{n} e^{-im\alpha}B_{nj}^{\dagger}\left(\frac{\pm k_z}{k}\right)\overrightarrow{\psi_n^{(1)}}(r) \tag{1.50}$$

where the operator B is expressed as:

$$B_{nj}(x) = -\frac{1}{i^{l+1}}\frac{1}{\sqrt{2l(l+1)}}\left(i\delta_{j1} + \delta_{j2}\right)\left(\delta_{pj}\tau_l^{|m|}(x) + \left(1-\delta_{pj}\right)m\pi_l^{|m|}(x)\right) \tag{1.51}$$

The operator $B^{\dagger}$ is the same with B except that i is replaced by $-i$

1.2.2 Layered system

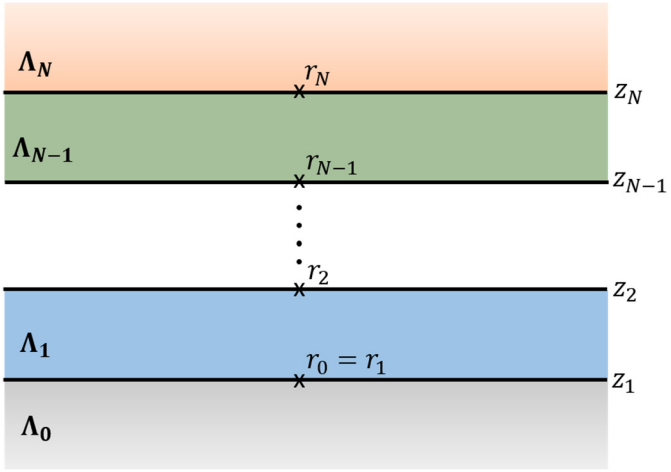

Figure 1.6. Sketch of $N+1$ ($\Lambda_0 \rightarrow \Lambda_N$) multilayer system with layer interfaces z_i and layer anchor points r_i

Figure 1.6 illustrates a multilayer system including N+1 layers (Λ_i, i = 0, …, N). Each layer is bounded by planes z_i and z_{i+1}, which are parallel to the xy-plane, and characterized by the refractive index n_i and the thickness d_i. The first and last layer (Λ_0 and Λ_N) are semi-infinite.

In a homogeneous layer, where there are no sources, the electric field can be expanded as follows:

$$\vec{E}(r) = \sum_{j=1}^{2} \int_{R^2} d^2k_{||} \left[\overrightarrow{\Phi_j^+}(\kappa, \alpha; r - r_i), \overrightarrow{\Phi_j^-}(\kappa, \alpha; r - r_i)\right] \cdot \begin{bmatrix} g_{i,j}^+(\kappa, \alpha) \\ g_{i,j}^-(\kappa, \alpha) \end{bmatrix} \tag{1.52}$$

The coefficients $g_{i,j}^+(\kappa, \alpha)$ and $g_{i,j}^-(\kappa, \alpha)$ are forward and backward PVWFs, defined at anchor point $r_i = (0,\ 0,\ z_i)$ for $i \geq 1$ and $r_0 = r_1$.

Transfer matrix method (TMM).[75] In the context of studying the propagation of an electromagnetic field within a multilayer system, it is crucial to analyze the coefficients associated with the field within each layer. The TMM is used to calculate the PVWF coefficients of the neighboring layers, which are constructed to satisfy the boundary conditions for the parallel components of the electromagnetic fields:

$$\begin{bmatrix} g_{i,j}^{+}(\kappa,\alpha) \\ g_{i,j}^{-}(\kappa,\alpha) \end{bmatrix} = I_j^{i,i+1}(\kappa) \begin{bmatrix} g_{i+1,j}^{+}(\kappa,\alpha) \\ g_{i+1,j}^{-}(\kappa,\alpha) \end{bmatrix} \tag{1.53}$$

with $i = 0$, the transfer matrix reads

$$I_j^{0,1}(\kappa) = \frac{1}{t_{0,1,j}(\kappa)} \begin{bmatrix} 1 & r_{0,1,j}(\kappa) \\ r_{0,1,j}(\kappa) & 1 \end{bmatrix} \tag{1.54}$$

Otherwise

$$I_j^{i,i+1}(\kappa) = \frac{1}{t_{i,i+1,j}(\kappa)} \begin{bmatrix} e^{-ik_{z,i}d_i} & 0 \\ 0 & e^{ik_{z,i}d_i} \end{bmatrix} \begin{bmatrix} 1 & r_{i,i+1,j}(\kappa) \\ r_{i,i+1,j}(\kappa) & 1 \end{bmatrix} \tag{1.55}$$

The Fresnel coefficients in amplitude can be calculated as

$$r_{i,i+1,1}(\kappa) = \frac{k_{z,i} - k_{z,i+1}}{k_{z,i} + k_{z,i+1}} \tag{1.56}$$

$$r_{i,i+1,2}(\kappa) = \frac{n_{i+1}^2 k_{z,i} - n_i^2 k_{z,i+1}}{n_{i+1}^2 k_{z,i} + n_i^2 k_{z,i+1}} \tag{1.57}$$

$$t_{i,i+1,1}(\kappa) = \frac{2k_{z,i}}{k_{z,i} + k_{z,i+1}} \tag{1.58}$$

$$t_{i,i+1,2}(\kappa) = \frac{2n_i n_{i+1} k_{z,i}}{n_{i+1}^2 k_{z,i} + n_i^2 k_{z,i+1}} \tag{1.59}$$

with the z-component of wave vector $k_{z,i} = \sqrt{k_i^2 - \kappa^2}$, where $k_i = n_i\omega/c$ in the layer Λ_i, and c is the light velocity in vacuum. In the case of multilayer, the forward and backward electric field coefficients of any two layers $i_1 < i_2$ can be connected to a global transfer matrix

$$\begin{bmatrix} g_{i_1,j}^{+}(\kappa,\alpha) \\ g_{i_1,j}^{-}(\kappa,\alpha) \end{bmatrix} = I_j^{i_1,i_2}(\kappa) \begin{bmatrix} g_{i_2,j}^{+}(\kappa,\alpha) \\ g_{i_2,j}^{-}(\kappa,\alpha) \end{bmatrix} \tag{1.60}$$

with

$$I_j^{i_1,i_2}(\kappa) = I_j^{i_1,i_1+1}(\kappa) \dots I_j^{i_2-1,i_2}(\kappa) \tag{1.61}$$

Scattering matrix method (SMM).[76] In contrast to the TMM, where it sets the relation between forward and backward propagating waves of two layers, SMM associates the incoming wave coefficients and the outgoing wave coefficients of a considered layer, enabling a more convenient analysis in quantifying the differences of the coefficients[77]

$$\begin{bmatrix} g_{i_2,j}^{+}(\kappa,\alpha) \\ g_{i_1,j}^{-}(\kappa,\alpha) \end{bmatrix} = S_j^{i_1,i_2}(\kappa) \begin{bmatrix} g_{i_1,j}^{+}(\kappa,\alpha) \\ g_{i_2,j}^{-}(\kappa,\alpha) \end{bmatrix} \tag{1.62}$$

The scattering matrix S_j of a multilayer system from i_1 to $i+1$ is defined as

$$S_j^{i_1,i+1}(\kappa) = S' = \begin{bmatrix} S'_{11} & S'_{12} \\ S'_{21} & S'_{22} \end{bmatrix} \tag{1.63}$$

which can be constructed in an iterative manner using the scattering matrix of the previous layer $S = S_j^{i_1,i}(\kappa)$ and the transfer matrix of the current layer $I = I_j^{i_1,i+1}(\kappa)$, starting with

$$S_j^{i_1,i_1}(\kappa) = \begin{bmatrix} 1 & 0 \\ 0 & 1 \end{bmatrix} \tag{1.64}$$

And

$$S'_{11} = \frac{S_{11}}{I_{11} - S_{12}I_{21}} \tag{1.65}$$

$$S'_{12} = \frac{S_{12}I_{22} - I_{12}}{I_{11} - S_{12}I_{21}} \tag{1.66}$$

$$S'_{21} = S_{22}I_{21}S'_{11} + S_{21} \tag{1.67}$$

$$S'_{22} = S_{22}I_{21}S'_{12} + S_{22}I_{22} \tag{1.68}$$

with $I_{11}, I_{12}, I_{21}, I_{22}$ are the elements of the transfer matrix of the current layer and $S_{11}, S_{12}, S_{21}, S_{22}$ are the elements of the scattering matrix of the previous layer.

Layered system response. The transfer matrix and scattering matrix method are efficiently used to calculate the distribution of electric field with an external source. However, our system consists of particles emitting scattered field, which can be seen as internal sources. This makes the source free condition for the expansion of electric field in the layer is not fulfilled. Consequently, no plane wave expansion of the electric field exists that holds everywhere in the layer. To answer the question of how electric field distributed in the layered system with such internal sources**.** What we can do is to split the electric field into two parts including the excitation field E_{exc} and the layered system response E_{exc}^{R} of the excitation field through the layered system:

$$\vec{E}(r) = \delta_{ii_{exc}} \overrightarrow{E_{exc}}(r) + \overrightarrow{E_{exc}^{R}}(r) \tag{1.69}$$

with the $\delta_{ii_{exc}}$ indicates that the excitation is only valid within the excited layer (i_{exc}), and the exciting field can be defined as

$$\overrightarrow{E_{exc}}(r) = \sum_{j=1}^{2} \int_{R^2} d^2 k_{||} \begin{cases} \overrightarrow{\Phi_j^{+}}(\kappa, \alpha; r - r_{i_{exc}}) g_{exc,j}^{+}(\kappa, \alpha)\,, & z \geq z^{+} \\ \overrightarrow{\Phi_j^{-}}(\kappa, \alpha; r - r_{i_{exc}}) g_{exc,j}^{-}(\kappa, \alpha)\,, & z \leq z^{-} \end{cases} \tag{1.70}$$

where $z^{\pm}$ denotes the upper and lower bound of the excitation. The layered system response can be specified by the coefficients $g_{exc,i,j}^{R_{\pm}}(\kappa, \alpha)$

$$\overrightarrow{E_{exc}^{R}}(r) = \sum_{j=1}^{2} \int_{R^2} d^2 k_{||} \left[\overrightarrow{\Phi_j^{+}}(\kappa, \alpha; r - r_i), \overrightarrow{\Phi_j^{-}}(\kappa, \alpha; r - r_i)\right] \cdot \begin{bmatrix} g_{exc,i,j}^{R_{+}}(\kappa, \alpha) \\ g_{exc,i,j}^{R_{-}}(\kappa, \alpha) \end{bmatrix} \tag{1.71}$$

To obtain the value of the layered system response coefficients, we can use the $L_j^{i,i_{exc}}(\kappa)$, which link the layered system response with the coefficients at the excited layer:

$$\begin{bmatrix} g^{R_+}_{exc,i,j}(\kappa,\alpha) \\ g^{R_-}_{exc,i,j}(\kappa,\alpha) \end{bmatrix} = L_j^{i,i_{exc}}(\kappa) \begin{bmatrix} g^{+}_{exc,j}(\kappa,\alpha) \\ g^{-}_{exc,j}(\kappa,\alpha) \end{bmatrix} \tag{1.72}$$

with the layered system response is evaluated as:

$$L_j^{i,i_{exc}}(\kappa) = \begin{cases} \left(I_j^{i_{exc},i}(\kappa)\right)^{-1}\left(L_j^{i_{exc}}(\kappa) + \begin{bmatrix} 1 & 0 \\ 0 & 0 \end{bmatrix}\right), & i > i_{exc} \\ I_j^{i,i_{exc}}(\kappa)\left(L_j^{i_{exc}}(\kappa) + \begin{bmatrix} 0 & 0 \\ 0 & 1 \end{bmatrix}\right), & i < i_{exc} \end{cases} \tag{1.73}$$

where $I_j^{i_1,i_2}$ is the transfer matrix defined in equation 1.61 and $L_j^{i_{exc}}(\kappa)$ can be deduced from scattering matrix method:

$$L_j^{i_{exc}}(\kappa) = \left(1 - \begin{bmatrix} 0 & S_{12}^{0,i_{exc}} \\ S_{21}^{i_{exc},N} & 0 \end{bmatrix}\right)^{-1} \begin{bmatrix} 0 & S_{12}^{0,i_{exc}} \\ S_{21}^{i_{exc},N} & 0 \end{bmatrix} \tag{1.74}$$

1.2.3 Scattering particles in layered system

The goal of this section is to present an approach to compute the electromagnetic field distribution scattered by particles located inside multilayer system. Here I only deal with spherical particles resided in the same layer and the incidence is plane wave illuminating from infinity. Considering a spherical particle S at the position r_S and refractive index n_S, surrounded by layer Λ_i with refractive index of n_i. The total electric field in layer i can be decomposed into four components:

$$\vec{E}(r) = \delta_{ii_{init}}\overrightarrow{E_{init}}(r) + \overrightarrow{E^R_{init}}(r) + \sum_S \left(\delta_{ii_S}\overrightarrow{E^S_{sca}}(r) + \overrightarrow{E^{R,S}_{sca}}(r)\right), \qquad r \in \Lambda_i \tag{1.75}$$

$E_{init}(r)$ is the incoming field in the layered medium. The layered system response of the initial field is denoted as $E^R_{init}(r)$. Whereas, $E^S_{sca}(r)$ and $E^{R,S}_{sca}(r)$ represent the scattered fields from particle S located within the layer Λ_{iS} and its response from multilayer, respectively. Using equation 1.46, SVWFs of the electric field in equation 1.75 can be expressed as

$$\vec{E}(r) = \sum_n (a_n^S \overrightarrow{\Psi_n^{(1)}}(r - r_S) + b_n^S \overrightarrow{\Psi_n^{(3)}}(r - r_S)) \tag{1.76}$$

This total field includes direction scattered field from particle S,

$$\overrightarrow{E_{sca}^S} = \sum_n b_n^S \overrightarrow{\Psi_n^{(3)}}(r - r_S) \tag{1.77}$$

and incoming field of the particle S,

$$\overrightarrow{E_{inc}^S} = \sum_n a_n^S \overrightarrow{\Psi_n^{(1)}}(r - r_S) \tag{1.78}$$

where the incoming field at particle S consists of the initial incident field, the direct scattered field from other particles (S$^{'}$ ≠ S) and the layered system responses of these electric fields. The next step is to find the relation between the incoming field coefficient (a_n^S) and the scattered field coefficient (b_n^S) using T-matrix method.

1.2.4 T-matrix method

The T-matrix method is originally introduced by Peter C. Waterman[78] to solve light scattering problem by non-spherical particle, which sets the relation between incoming field coefficients to scattered field coefficients:

$$b_n^S = \sum_{n'=1}^{\infty} T_{nn'}^S a_{n'}^S \tag{1.79}$$

As discussed previously, the multi-index n accounts for the multipole degrees, multipole orders and the polarization. Practically, the infinite sum in equation 1.79 can be truncated at a finite multi-index $n_{\max}$ that corresponds to the cut-off multipole order $l_{\max}$, which is sufficient for the convergence result.

The T-matrix method have been continuously discussed and updated, a collection of recent publications about the method can be found in the paper.[79] One of the method that are used to compute the T-matrix is Mie solution, which is applied in the case of a spherical particle.

In order to solve the scattering problem using T-matrix method, the incoming field need to be defined and expanded in term of SVWFs. As mentioned earlier, the incoming field comprises of the initial incident field, the scattered field from other particles and the layered system response of initial field and all particles. Note that, in my thesis, I only use propagating plane wave as initial field. Description for other types of initial fields can be found in Egel's thesis.[69] The main task here is to find the coupling matrix V, V^R, corresponding to the transformation of PWE to SWE of the direct coupling and layered system response, and W, W^R representing the direct coupling and layered system response of the SWE, which is illustrated in fig. 1.7. To begin with, we define the

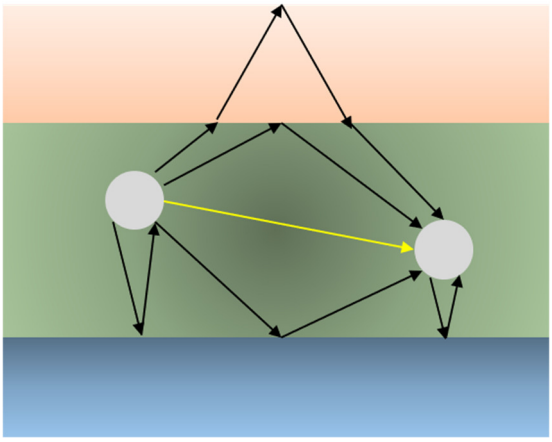

Figure 1.7. Illustration of the coupling between two particles in layered system. Yellow arrow indicates direct coupling, while black arrows represent the layered system response of scattered fields.

electric field at any received point in the layer (r_{rec}) illuminated by an excitation (r_{exc}) within the same layer:

$$\vec{E}(r_{rec}) = \delta_{i_{rec},i_{exc}}\overrightarrow{E_{exc}} + \overrightarrow{E^R_{exc}}(r_{rec}) \tag{1.80}$$

$$\vec{E}(r_{rec}) = \delta_{i_{rec},i_{exc}}\sum_n a_n^{rec,exc}\overrightarrow{\Psi_n^{(1)}}(r - r_{rec}) + \sum_n a_n^{rec,R,exc}\overrightarrow{\Psi_n^{(1)}}(r - r_{rec}) \tag{1.81}$$

Coupling matrices for converting from PWE to SWE. In the case of direct coupling, when the particles are in the same layer as the source, the PVWF is first translated to the reference point (r_{rec}) as following:

$$\overrightarrow{\Phi_{\mathrm{J}}^{\pm}}(\kappa,\alpha;r-r_{i_{exc}})=e^{ik_{i_{exc}}^{\pm}\cdot(r_{i_{exc}}-r_{rec})}\overrightarrow{\Phi_{\mathrm{J}}^{\pm}}(\kappa,\alpha;r-r_{rec}) \tag{1.82}$$

then rewrite PVWFs in term of SVWFs using equation 1.49, and finally the direct coupling coefficient can be deduced as:

$$a_n^{rec,exc}=4\sum_{j=1}^{2}\int_{R^2}d^2\,k_{||}(g_{exc,j}^{\pm}(k_{||})e^{-im\alpha}e^{ik_{i_{exc}}^{\pm}\cdot(r_{i_{exc}}-r_{rec})}\mathrm{B}_{nj}^{\dagger}\left(\frac{\pm k_{z,i_{exc}}}{k_{i_{exc}}}\right) \tag{1.83}$$

where, the plus sign denotes $z_{rec}>z_{exc}$ and minus sign corresponds to $z_{rec}<z_{exc}$. Equation 1.83 can be rewritten in the form of the PWE to SWE coupling operator as

$$a_n^{rec,exc}=4\sum_{j=1}^{2}\int_{R^2}d^2\,k_{||}[V_{nj}^{+}(r_{rec},r_{exc};k_{||}),V_{nj}^{-}(r_{rec},r_{exc};k_{||})].\begin{bmatrix}g_{exc,j}^{+}(k_{||})\\g_{exc,j}^{-}(k_{||})\end{bmatrix} \tag{1.84}$$

where,

$$V_{nj}^{\pm}(r_{rec},r_{exc};k_{||})=e^{-im\alpha}e^{ik_{i_{exc}}^{\pm}\cdot(r_{i_{exc}}-r_{rec})}\mathrm{B}_{nj}^{\dagger}\left(\frac{\pm k_{z,i_{exc}}}{k_{i_{exc}}}\right) \tag{1.85}$$

Next, we calculate the layered system response operator. The electric field of the layered system response can be written through the coefficients $g_{exc,i_{rec},j}^{R\pm}(k_{||})$ as:

$$\overrightarrow{E_{exc}^{R}}(r)=\sum_{j=1}^{2}\int_{R^2}d^2k_{||}\left[\overrightarrow{\Phi_{\mathrm{J}}^{+}}(k_{||};r-r_{i_{rec}}),\overrightarrow{\Phi_{\mathrm{J}}^{-}}(k_{||};r-r_{i_{rec}})\right]\cdot\begin{bmatrix}g_{exc,i_{rec},j}^{R+}(k_{||})\\g_{exc,i_{rec},j}^{R-}(k_{||})\end{bmatrix} \tag{1.86}$$

where the coefficient $g_{exc,i_{rec},j}^{R\pm}$ can be deduced from matrix L according to Equation 1.72.

$$\begin{bmatrix} g^{R_+}_{exc,i_{rec},j}(k_{||}) \\ g^{R_-}_{exc,i_{rec},j}(k_{||}) \end{bmatrix} = L_j^{i_{rec},i_{exc}}(\kappa) \begin{bmatrix} g^{+}_{exc,j}(\kappa,\alpha) \\ g^{-}_{exc,j}(\kappa,\alpha) \end{bmatrix} \tag{1.87}$$

Substitute the coefficient into equation 1.86 then translate the coordinate from $r_{i_{rec}}$ to r_{rec} and finally transform PVWFs to SVWFs, leading to:

$$a_n^{rec,R,exc} = 4\sum_{j=1}^{2}\int_{R^2} d^2\, k_{||} e^{-im\alpha} \cdot \begin{bmatrix} e^{ik^{+}_{i_{rec}}\cdot(r_{rec}-r_{i_{rec}})} B_{nj}^{\dagger}\left(\dfrac{k_{z,i_{rec}}}{k_{i_{rec}}}\right) \\ e^{ik^{-}_{i_{rec}}\cdot(r_{rec}-r_{i_{rec}})} B_{nj}^{\dagger}\left(\dfrac{-k_{z,i_{rec}}}{k_{i_{rec}}}\right) \end{bmatrix} \cdot L_j^{i_{rec},i_{exc}}(\kappa) \cdot \begin{bmatrix} g^{+}_{exc,j}(k_{||}) \\ g^{-}_{exc,j}(k_{||}) \end{bmatrix} \tag{1.88}$$

Introducing the notations

$$\beta^{\pm}_{exc,n,j}(\kappa) = e^{\mp ik_{z,i_{exc}}(z_{exc}-z_{i_{exc}})} B_{nj}\left(\frac{\pm k_{z,i_{exc}}}{k_{i_{exc}}}\right) \tag{1.89}$$

$$\beta^{\pm,\dagger}_{rec,n,j}(\kappa) = e^{\pm ik_{z,i_{rec}}(z_{rec}-z_{i_{rec}})} B_{nj}^{\dagger}\left(\frac{\pm k_{z,i_{rec}}}{k_{i_{rec}}}\right) \tag{1.90}$$

and the coupling operators:

$$\begin{aligned} &\left[V_{n,j}^{R+}(r_{rec},r_{exc};k_{||}), V_{n,j}^{R,-}(r_{rec},r_{exc};k_{||})\right] \\ &\qquad = 4e^{-im\alpha}e^{ik_{||}\cdot r_{rec,||}} \times \left[\beta^{+,\dagger}_{rec,n,j}(\kappa), \beta^{-,\dagger}_{rec,n,j}(\kappa)\right] \cdot L_j^{i_{rec},i_{exc}}(\kappa) \end{aligned} \tag{1.91}$$

The expansion coefficient for the layered system response is then simplified as:

$$a_n^{rec,R,exc} = \sum_{j=1}^{2}\int_{R^2} d^2\, k_{||} \begin{bmatrix} V_{n,j}^{R,+}(r_{rec},r_{exc};k_{||}) \\ V_{n,j}^{R,-}(r_{rec},r_{exc};k_{||}) \end{bmatrix} \cdot \begin{bmatrix} g^{+}_{exc,j}(k_{||}) \\ g^{-}_{exc,j}(k_{||}) \end{bmatrix} \tag{1.92}$$

Excitation by spherical vector wavefunction. A spherical vector wave expansion from an excitation position r_{exc} is expressed as

$$\overrightarrow{E_{exc}}(r) = \sum_{n'} b_{n'}^{exc} \overrightarrow{\Psi_{n'}^{(3)}}(r - r_{exc}) \tag{1.93}$$

In the case of direct coupling, the particles must be within the same layer. Employing the addition theorem, the electric field can be expanded in term of incoming field:

$$\begin{aligned} \overrightarrow{E_{exc}}(r) &= \sum_{n'} b_{n'}^{exc} \sum_{n} A_{n'n}(r_{rec} - r_{exc}) \overrightarrow{\Psi_{n}^{(1)}}(r - r_{exc}) \\ \overrightarrow{E_{exc}}(r) &= \sum_{n} a_{n}^{rec,exc} \overrightarrow{\Psi_{n}^{(1)}}(r - r_{exc}) \end{aligned} \tag{1.94}$$

for $|r - r_{rec}| < |r_{exc} - r_{rec}|$, and the direct coupling coefficient is

$$a_{n}^{rec,exc} = \sum_{n'} W_{n,n'}(r_{rec} - r_{exc}) b_{n'}^{exc} \tag{1.95}$$

with the direct coupling matrix

$$W_{n,n'}(r_{rec}, r_{exc}) = A_{n'n}(r_{rec} - r_{exc}) \tag{1.96}$$

In the case of layered system response, we first transform the SVWFs into PVWFs and translate to the layer anchor point $r_{i_{exc}}$, the electric field then reads:

$$\begin{aligned} \overrightarrow{E_{exc}}(r) &= \sum_{n'} b_{n'} \overrightarrow{\Psi_{n'}^{(3)}}(r - r_{exc}) \\ &= \frac{1}{2\pi} \sum_{j=1}^{2} \sum_{n'} b_{n'} \int_{R^2} \frac{d^2 k_{||}}{k_{z,i_{exc}} k_{i_{exc}}} e^{-im'\alpha} B_{n'j}(\pm k_{z,i_{exc}} / k_{i\_exc}) \\ &\quad \times e^{-ik_{i_{exc}}^{\pm} \cdot (r_{i_{exc}} - r_{rec})} \overrightarrow{\Phi_{j}^{\pm}}(\kappa, \alpha; r - r_{i_{exc}}) \end{aligned} \tag{1.97}$$

for $z \lesseqgtr z_{exc}$. Using the notation $\beta_{exc,n',j}^{\pm}(\kappa)$ defined in equation 1.89, the electric field becomes

$$
\begin{aligned}
&\overrightarrow{E_{exc}}(r) \\
&= \frac{1}{2\pi}\sum_{j=1}^{2}\sum_{n'} b_{n'}\int_{R^2}\frac{d^2k_{||}}{k_{z,i_{exc}}k_{i_{exc}}}e^{-im'\alpha}e^{-ik_{||}\cdot\left(r_{exc,||}-r_{i_{exc},||}\right)}\times\beta^{\pm}_{exc,n',j}(\kappa)\overrightarrow{\Phi^{\pm}_{\mathrm{J}}}\big(\kappa,\alpha;r \\
&- r_{i_{exc}}\big) \\
&= \sum_{1}^{2}\int_{R^2} d^2\,k_{||}[\overrightarrow{\Phi^{+}_{\mathrm{J}}}(\kappa,\alpha;r-r_{i_{rec}}),\overrightarrow{\Phi^{-}_{\mathrm{J}}}(\kappa,\alpha;r-r_{i_{rec}})]\begin{bmatrix}g^{+}_{exc,j}(\kappa,\alpha)\\ g^{-}_{exc,j}(\kappa,\alpha)\end{bmatrix}
\end{aligned}
\tag{1.98}
$$

for $z \lesseqgtr z_{exc}$. The coefficients are thus:

$$
\begin{bmatrix}g^{+}_{exc,j}(\kappa,\alpha)\\ g^{-}_{exc,j}(\kappa,\alpha)\end{bmatrix} = \frac{1}{2\pi}\frac{e^{-ik_{||}\cdot r_{exc,||}}}{k_{z,i_{exc}}k_{i_{exc}}}\sum_{n'} b_{n'}e^{im'\alpha}\,\Psi^{(3)}_{n'}(r-r_{exc})\,L_j^{i_{rec},i_{exc}}(\kappa)\begin{bmatrix}\beta^{+}_{exc,n',j}(\kappa)\\ \beta^{-}_{exc,n',j}(\kappa)\end{bmatrix} \tag{1.99}
$$

Next, translate the reference point of the PVWFs to r_{rec} and then transform PVWFs to SVWFs, which allow us to find the layered system response

$$
\begin{aligned}
a_n^{rec,R,exc} &= \frac{2}{\pi}\sum_{j=1}^{2}\sum_{n'} b_{n'}\int_{R^2}\frac{d^2k_{||}}{k_{z,i_{exc}}k_{i_{exc}}}e^{-i(m'-m)\alpha}e^{ik_{||}\cdot\left(r_{rec,||}-r_{exc,||}\right)} \\
&\qquad\times\left[\beta^{+,\dagger}_{rec,n,j}(\kappa),\beta^{-,\dagger}_{rec,n,j}(\kappa)\right]\cdot L_j^{i_{rec},i_{exc}}(\kappa)\cdot\begin{bmatrix}\beta^{+}_{exc,n',j}(\kappa)\\ \beta^{-}_{exc,n',j}(\kappa)\end{bmatrix} \\
&= \sum_{n'} W^{R}_{n,n'}(r_{rec},r_{exc})\,b^{exc}_{n'}
\end{aligned}
\tag{1.100}
$$

which leads to the response coupling matrix

$$
\begin{aligned}
W^{R}_{n,n'} = \frac{2}{\pi}\sum_{j=1}^{2}\int_{R^2}\frac{d^2k_{||}}{k_{z,i_{exc}}k_{i_{exc}}}e^{i(m'-m)\alpha}e^{ik_{||}\cdot\left(r_{rec,||}-r_{exc,||}\right)}\times\left[\beta^{+,\dagger}_{rec,n,j}(\kappa),\beta^{-,\dagger}_{rec,n,j}(\kappa)\right] \\
\cdot L_j^{i_{rec},i_{exc}}(\kappa)\cdot\begin{bmatrix}\beta^{+}_{exc,n',j}(\kappa)\\ \beta^{-}_{exc,n',j}(\kappa)\end{bmatrix}
\end{aligned}
\tag{1.101}
$$

Multiple scattering. In the context of multiple scattering, the incoming fields at a particle S are coming from the scattered fields and the layered system responses of other particle S' (S'≠S). The direct scattered field from S' reads

$$\overrightarrow{E_{S'}}(r) = \sum_{n'} b_{n'}^{S'} \overrightarrow{\Psi_{n'}^{(3)}}(r - r_{S'}) \tag{1.102}$$

Translating to the incoming field at the center of spherical S as

$$\overrightarrow{E_{sca}^{S'}}(r) = \sum_{n} a_n^{S,S'} \overrightarrow{\Psi_n^{(1)}}(r - r_S) \tag{1.103}$$

with

$$a_n^{S,S'} = \sum_{n'} W_{nn'}(r_S, r_{S'}) \tag{1.104}$$

Similarly, translate the layered system response to the incoming field at the center of particle S

$$\overrightarrow{E_{sca}^{R,S'}}(r) = \sum_{n} a_n^{S,R,S'} \overrightarrow{\Psi_n^{(1)}}(r - r_S) \tag{1.105}$$

with

$$a_n^{S,R,S'} = \sum_{n'} W_{nn'}^{R}(r_S, r_{S'}) \tag{1.106}$$

Using T-matrix method to connect the incoming field coefficient to the scattered field coefficient, we arrive at

$$b_n^S = \sum_{n'} T_{nn'}^S a_{n'}^S \tag{1.107}$$

with $T^S_{nn'}$ is the T-matrix of particle S, and $a^S_{n'}$ is the incoming field coefficient, which includes direct incident and scattered field from other particles and their layered system responses

$$a^S_n = a^{S,init}_n + a^{S,R,init}_n + \sum_{S'}\sum_{n'}\left(W_{n,n'}(r_S, r_{S'}) + W^R_{n,n'}(r_S, r_{S'})\right)b^{S'}_{n'} \tag{1.108}$$

From equations 1.107 & 1.108, we can construct a self-consistent set of equations for the scattered field coefficients as

$$\sum_{S'}\sum_{n'} M^{SS'}_{nn'} b^{S'}_{n'} = \sum_{n'} T^S_{nn'}\,(a^{S,init}_{n'} + a^{S,R,init}_{n'}) \tag{1.109}$$

with

$$M^{SS'}_{nn'} = \delta_{SS'}\delta_{nn'} - \sum_{n''} T^S_{nn''}(W_{n''n'}(r_S, r_{S'}) + W^R_{n''n'}(r_S, r_{S'})) \tag{1.110}$$

Once the scattered field coefficient is known, other quantities, such as near-field, far field and cross section can be determined.

1.2.5 Near-field, far field, cross section, transmission and reflection.

Far field. The far field intensity of the scattered field can be determined as

$$I_{\Omega,j}(\beta, \alpha) = \frac{2\pi^2}{\omega\mu_0} k k_z^2 \left| g^{\pm\infty}_{sca,j}(\kappa, \alpha)\right|^2 \tag{1.111}$$

with plus and minus sign corresponding to the field in the top layer (Λ_N) with $\beta \in [0, \pi/2]$ and in the bottom layer (Λ_0) with $\beta \in [\pi/2, \pi]$ as shown in figure 1.6, and

$$g^{+\infty}_{sca,j}(\kappa, \alpha) = \sum \delta_{Ni_S} g^{+}_{S,j}(\kappa, \alpha) + g^{R,+}_{S,N,j}(\kappa, \alpha) \tag{1.112}$$

$$g_{sca,j}^{-\infty}(\kappa,\alpha) = \sum_{S} \delta_{0i_S} g_{S,j}^{-}(\kappa,\alpha) + \; g_{S,0,j}^{R,-}(\kappa,\alpha) \tag{1.113}$$

with the plane wave expansion coefficient ($g_{S,j}^{\pm}(\kappa,\alpha)$) and its layered system response ($g_{S,N,j}^{R,\pm}(\kappa,\alpha)$) as = shown in equations 1.99 and 1.87 respectively.

Near-field. The near-field at any point is the sum of the initial field, scattered field of all particles and its layered system response, where the direct scattered field from all particles

$$\overrightarrow{E_{sca}^{S}}(r) = \sum_{n} b_n^S \overrightarrow{\Psi_n^{(3)}}(r - r_S) \tag{1.114}$$

and the layered system response

$$\overrightarrow{E_S^R}(r) = \sum_{j=1}^{2} \int_{R^2} d^2k_{||} \left[\overrightarrow{\Phi_j^{+}}(k_{||}; r - r_i), \overrightarrow{\Phi_j^{-}}(k_{||}; r - r_i)\right] \cdot \begin{bmatrix} g_{S,i,j}^{R_+}(k_{||}) \\ g_{S,i,j}^{R_-}(k_{||}) \end{bmatrix} \tag{1.115}$$

In the case of spherical particle, the near-field is valid even inside the particle.

Scattering cross sections. The scattering cross sections can be evaluated as the integral of the differential cross section over a solid angle ($\Omega(\beta,\alpha)$)

$$\sigma_{sca} = \int d^2\Omega \sigma_{\Omega,\mathrm{sca}}(\beta,\alpha) \tag{1.116}$$

with the differential scattering cross section is determined as

$$\sigma_{sca} = I_{A,init}^{-1} \frac{d\,\langle \Phi_{sca,i_\beta} \rangle}{d\Omega} = I_{A,init}^{-1} \sum_{j=1}^{2} I_{\Omega,j}(\beta,\alpha) \tag{1.117}$$

and $I_{A,init}$ is the initial far field intensity per interface area (A), i_β is for the top ($\beta < \pi/2$) or bottom ($\beta > \pi/2$) layer and $\langle \Phi_{sca,i_\beta} \rangle$ is the time-averaged radiant flux of the scattered field in layer i.

Extinction cross section. In the presence of plane interfaces, the extinction cross section is evaluated separately in transmission and reflection sides, indicating the power taken away from the initial field in the transmission and reflection direction. According to Egel,[69] the extinction power in the reflection side (assume that light is coming from the bottom) reads

$$\langle P_{bot,extinct} \rangle = -\frac{4\pi^2 k_{z,0}}{\omega \mu_0} Re(A_p r_{jp}(\kappa_p) e^{ik_{P,i_P} \cdot r_{iP}} g^{-\infty *}_{scat,j}(\kappa_P, \alpha_P)) \tag{1.118}$$

which leads to the extinction cross section in reflection

$$\sigma_R = I^{-1}_{A,init} \langle P_{bot,extinct} \rangle \tag{1.119}$$

Similarly, the extinction power in transmission reads

$$\langle P_{top,extinct} \rangle = \frac{4\pi^2 k_{z,N}}{\omega \mu_0} Re(A_p t_{jp}(\kappa_p) e^{ik_{P,i_P} \cdot r_{iP}} g^{+\infty *}_{scat,j}(\kappa_P, \alpha_P)) \tag{1.120}$$

and the extinction cross section

$$\sigma_T = I^{-1}_{A,init} \langle P_{top,extinct} \rangle \tag{1.121}$$

Note that in the context of scattering problem near or on planar surfaces, extinction cross section in transmission or reflection can be negative, suggesting the enhancement of the electromagnetic intensity due to the presence of the scatterers.

Transmission and reflection coefficients. All of the quantities of interest described above are derived without approximation from the full rigorous analytical description of electromagnetic

field. In most cases, those quantities are adequate to deduce the optical properties of the system. However, when comparing with experimental results, it would be interesting to derive the simulated transmission and reflection coefficients. An mathematical approximation to estimate the transmission and reflection coefficients using the calculated extinction cross section in transmission and reflection sides have been proposed.[38] The transmittance coefficient can be calculated by dividing the transmitted power (P_T) by incident power (P_i), where the transmitted power is the sum of transmitted power by the layered system ($P_{T,layer}$) and scattered power of NPs within a solid angle Ω ($P_{sca}(\Omega)$) minus by the extinguished power from the present of NPs (P_{NP}). For the sake of simplicity, we neglect the scattered power of NPs. Mathematically, the coefficient can be determined as

$$\begin{aligned} T = \frac{P_T}{P_i} &= \frac{P_{T,layer} - P_{NP} + P_{sca}(\Omega)}{P_i} \\ &= \frac{\Delta S I_{T,layer} - C_{ext,T} I_{T,layer} + P_{sca}(\Omega)}{\Delta S I_i} \\ &\approx \frac{I_{T,layer}}{I_i} - \frac{I_{T,layer}}{I_i}\frac{C_{ext,T}}{\Delta S} \\ T &\approx \frac{I_{T,layer}}{I_i}\left(1 - \frac{C_{ext,T}}{\Delta S}\right) \end{aligned} \tag{1.122}$$

with ΔS is the detector size.

Analogously, the reflection coefficient reads

$$R \approx \frac{I_{R,layer}}{I_i}\left(1 - \frac{C_{ext,R}}{\Delta S}\right) \tag{1.123}$$

ΔS can be seen as a normalization term and it can be chosen as the maximum calculated extinction cross sections.

1.2.6 Using *smuthi*

The T-matrix-based modeling method described above was translated to the Python code: *smuthi*, which stands for scattering by multiple particles in thin-film systems. Structure of the software is shown in Fig. 1.8 with a comprehensive description for each building block and basic principles are already discussed by Egel and colleagues,[72] which can be summarized into three steps:

- Define the input of their system, including geometrical parameters and simulation parameters of particles, layered system and initial field.
- Launch the program by using the command *simulation.run()*
- Extract the parameters of interest, such as cross section or electromagnetic near-field using post-processing step.

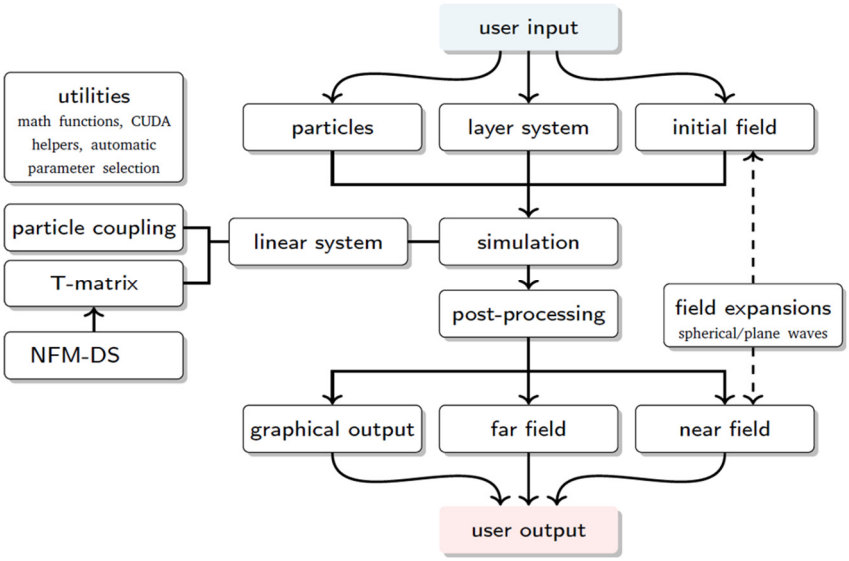

Figure 1.8. Structure and flow chart of *smuthi*. The figure is taken from Egel et al.[72] NFM-DS indicates the Null-field method with discrete sources with FORTRAN code developed by Adrian Doicu, Thomas Wriedt and Yuri Eremin.[71]

To illustrate the use of *smuthi*, an example with a complete script is given to calculate extinction cross section and the contribution of multipole resonances in reflection and transmission of a spherical silver particle buried in thin film, the structure of which is shown in Fig. 1.9.

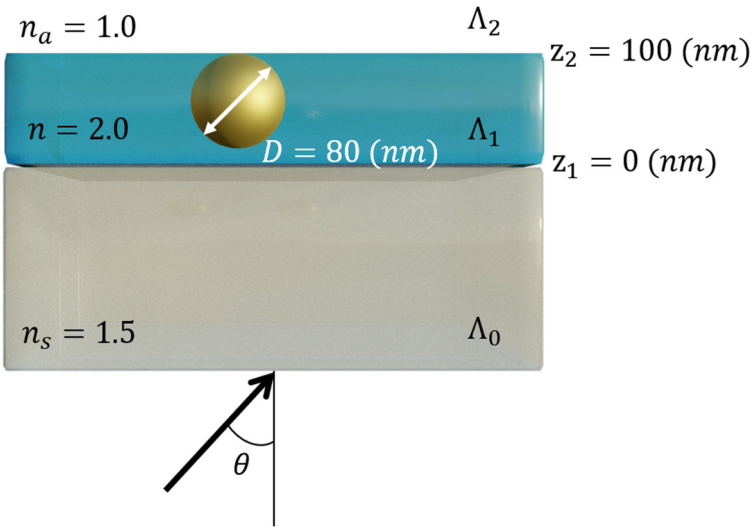

Figure 1.9. A multilayer system with an embedded nanoparticle (diameter = 80 *nm*). Layers are defined from the bottom: Λ_0, Λ_1, Λ_2 respectively, with the first interface z_1 = 0 (nm) and second interface z_2 = 100 (nm)

```
## IMPORT PYTHON AND SMUTHI PACKAGES
import numpy as np
import smuthi.simulation
import smuthi.initial_field
import smuthi.layers
import smuthi.particles
import smuthi.postprocessing.far_field as ff


## DEFINE INPUT PARAMETERS
# Single particle
sphere = smuthi.particles.Sphere(position=[0, 0, 60],
                                 refractive_index = 1.52,
                                 radius = 40,
```

```
                                        l_max=3)
spheres_list = [sphere]
# Define layer
layers = smuthi.layers.LayerSystem(thicknesses = [0, 100, 0],
                                                refractive_indices = [1.5, 2.0, 1.0])
# Define initial field
plane_wave = smuthi.initial_field.PlaneWave(vacuum_wavelength = 550,
                                                    polar_angle = (180/180)*np.pi,
                                                    azimuthal_angle = 0,
                                                    polarization = 0)
# Combine input parameters
simulation = smuthi.simulation.Simulation(layer_system = layers,
                                                    particle_list = spheres_list,
                                                    initial_field = plane_wave)


## IMPORT REFRACTIVE INDEX OF SILVER
silver = np.loadtxt("silver.txt")
wavelengths = np.arange(350, 751, 4)
n_Ag = np.interp(wavelengths, silver[:,0], silver[:,1])


## LANCH THE SIMULATION
for i in range(len(wavelengths)):
    simulation.k_parallel = "default"
```

simulation.initial_field.vacuum_wavelength = wavelengths[i]

simulation.layer_system.refractive_indices= n_Ag[i]

simulation.run()

 # Post processing

ref = ff.extinction_cross_section(simulation,extinction_direction='reflection')

trn = ff.extinction_cross_section(simulation,extinction_direction='transmission')

dipole_trn = ff.extinction_cross_section(simulation,extinction_direction='transmission', only_l =1)

quadrupole_trn = ff.extinction_cross_section(simulation,extinction_direction='transmission', only_l =2)

ref_list.append(ref.real/1e6)

trn_list.append(trn.real/1e6)

dipole_trn_list.append(dipole_trn.real/1e6)

quadrupole_trn_list.append(quadrupole_trn.real/1e6)

In the above simulation:

1) The layered system starts from the bottom (substrate) to the top (superstrate) with the thickness are $\Lambda_0 = \Lambda_2 = 0$, which is defined in the program as "*thicknesses = [0, 100, 0]"* (thicknesses = $[\Lambda_0, \Lambda_1, \Lambda_2]$), the refractive indices are also specified accordingly (refractive_indices = $[n_s, n, n_a]$) . The $z = 0$ position is defined at the interface between the substrate and the first layer.
2) Incidence angle is shown in Fig. 1.9, where it illuminates from the bottom and is defined as *"polar_angle = (θ/180)*np.pi"* with θ is the incidence angle. In the program, I define the

incidence from the top at normal angle, therefore θ is equal to 180 (*polar_angle = (*180*/180)*np.pi*).

3) The unit in *smuthi* is relative and all the lengths defined for layer thickness, particle size and wavelength must be consistent. If the wavelength is in nanometer, the cross section will be in nm^2. In the program, all the cross-section quantities ("post processing" step) are converted to μm^2 by dividing to 10^6 (*1e6*)
4) The multipole degree truncation (l_max) determined multipole expansion cutoff, implying that the T-matrix is truncated at the multipole degree defined by l_max. For example, if l_max = 1, only dipolar resonance is allowed in the system, or l_max = 3 means the system allow up to octupolar mode. In the "post processing" step, the dipolar mode in transmission side is extracted by specifying the parameters: *extinction_direction='transmission'* and *only_l =1*.
5) The parameter "*polarization*" corresponds to the incidence polarization for TE (*polarization = 0*) and TM (*polarization = 1*)
6) The refractive index of silver particle in the "single particle" step is arbitrary, it is overwritten in the "for loop" to adapt the dispersive relation of the silver refractive index.

When using *smuthi* several restrictions need to be considered, which were also listed detailly by Egel et al.[72] It should also be mentioned that the particle must be in the same layer and not intersect with layer interfaces, and it can create artifact when simulating diffractive structures with small array size as shown in Fig. 1.10. However, this issue has been addressed by other groups using different approach.[80] Compared to other simulation approaches such as FDTD or FEM, the T-matrix-based method is much faster. Specifically, for the system shown in figure 1.10, it is required about 20 minus per a simulation, while is can be extended to more than 5 hours for FDTD.

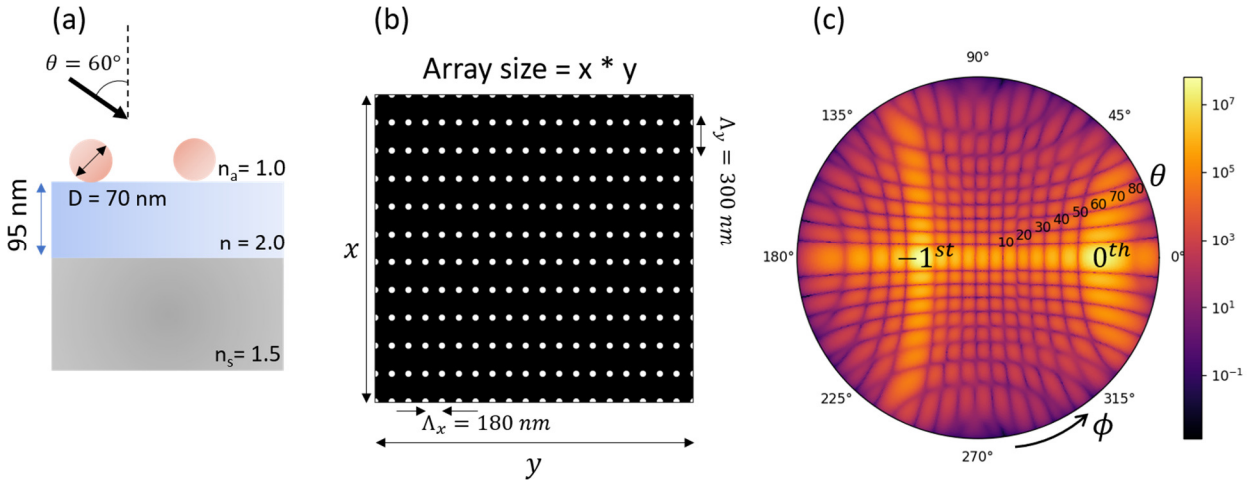

Figure 1.10. Illustration of artifact arising from the simulation of small array size at $\lambda = 520\ nm$. (a, b) cross section and plane view of the simulated structure with $x = 3300\ nm$ and $y = 3420\ nm$. (c) 2D map of scattering cross section as a function of the incidence angle

Figure 1.10c displays 2D map of scattering cross section as a function of polar angle (θ) and azimuth angle (ϕ). Beside the specular reflection peak (0^{th}) and the -1^{th} diffraction order peak from the nanoparticle array, there are several other peaks, arising from the diffraction of the simulated structure's rectangular shape. This artifact appears only when the simulated size and the incidence wavelength are comparable. To avoid the problem, we can apply the periodic boundary condition along x and y directions for T-matrix method (implemented from *smuthi* version 2.0) or simply enlarge the simulated array size by duplicating the size in Fig. 1.10b. The latter is implemented in Chapter 4 to study the diffraction properties of our samples.

1.3 Optical properties of plasmonic nanoparticles

In the subsequent sections, we will delve into the critical geometric parameters governing the optical behaviors in visible wavelength or color responses of plasmonic nanomaterials. Within the scope of this thesis, the investigation will be limited to silver spherical particles, and thus the impact of particle shape and material composition on optical properties will not be addressed. Instead, this section will be devoted to investigate the optical properties as a function of particle

size, surrounding media, the concept of lattice resonances, and it will be finished by giving a brief introduction to the influence of nanoparticle organization on the optical responses.

1.3.1 Influence of nanoparticle size

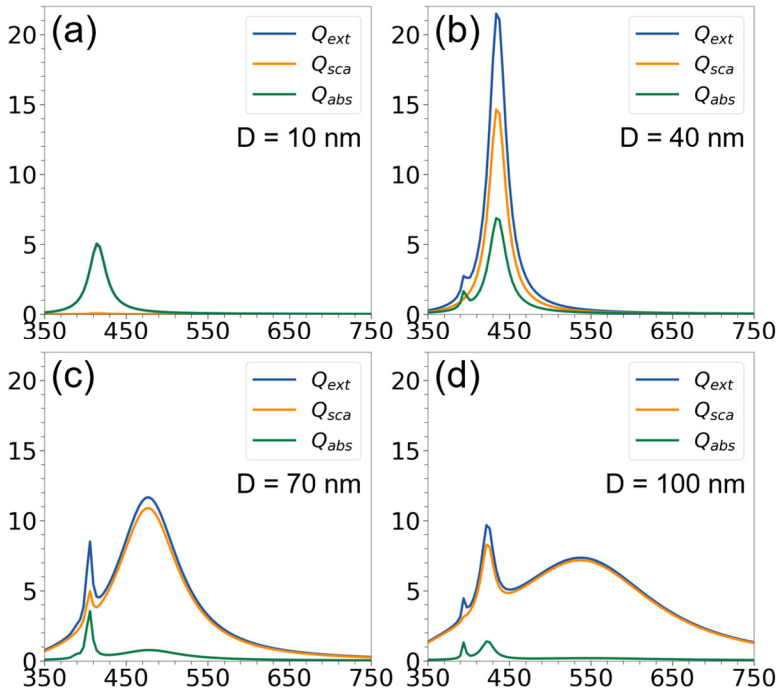

Figure 1.11. Extinction, scattering and absorption efficiencies of silver particles with the diameters of 10, 40, 70, 100 nm respectively. The surrounding medium has the relative permittivity of 2.25

To study the influence of particle size on the optical responses, we consider silver particles with different sizes surrounded by a homogeneous medium with $\epsilon = 2.25$ and the calculation is based on simulation discussed in section 1.2 with no layered system (in the simulation we can define layer system with two media having the same refractive indices). Figure 1.11 shows the extinction, scattering and absorption efficiencies of silver particles with an increasing size. Several interesting optical responses can be observed. First, the relative contribution of the scattering and absorption to the total extinction efficiency increases and decreases, respectively, when increasing the nanoparticle size. Interestingly, in this size range of particle, the quasi-static approximation discussed in section 1.1.5 is still valid to explain the optical behavior, which results from the

dependency of the scattering and absorption efficiency on the scaling factors of k^4R^4 and kR (equations 1.25 & 1.26). Second, increasing particle size also leads to a spectral broadening due to the increase in the radiation damping rate,[81] and a resonance red-shift, attributed to the weakening of the restoring force that is correlated to the accumulated charges at the particle surface and inversely proportional to the distance between excited negative electron charges and positive ion charges. Finally, multiple peaks start to arise in large particles (at lower wavelengths), which are associated with the higher multipolar resonances (quadrupole or

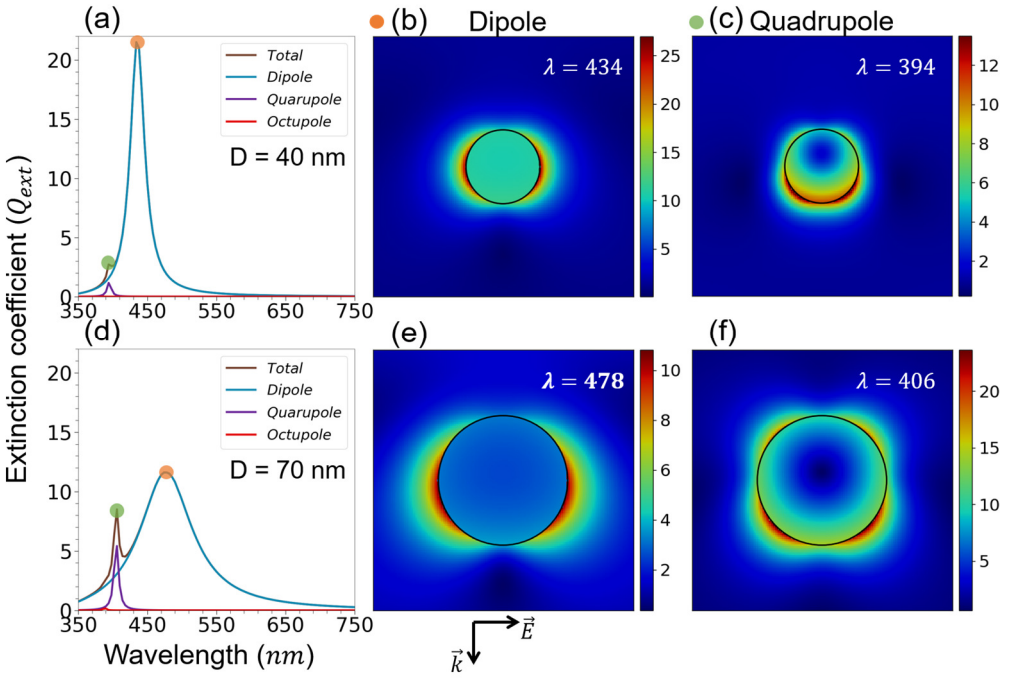

Figure 1.12. Multipole decomposition and electric field enhancement at the selected wavelengths

octupole). To better understand the nature of these multipolar resonances, figure 1.12 is provided, which shows the multipole decomposition and the electric near-field at dipolar and quadrupole resonances of two particles with different sizes. As stated previously, the contribution of higher multipolar resonances to the total efficiency becomes more significant for larger particles (Figure 1.12a & d). While dipole excitation exhibits broad resonance at higher wavelength with two main maxima distributed on the surface the nanoparticle. On the other hand, quadrupole excitation shows a narrower peak at lower wavelength with four main maxima located on the surface of the particle, as depicted in Figure 1.12.

1.3.2 Influence of the surrounding media

The surrounding medium can also influence the plasmonic resonances through the induced polarization. When excited by an external field, polarizations of the particle and the dielectric medium are induced. The latter arises from a charge accumulation in the adjacent of the particle, which can compensate with the induced charges from the polarized particle as illustrated in Fig. 1.13.

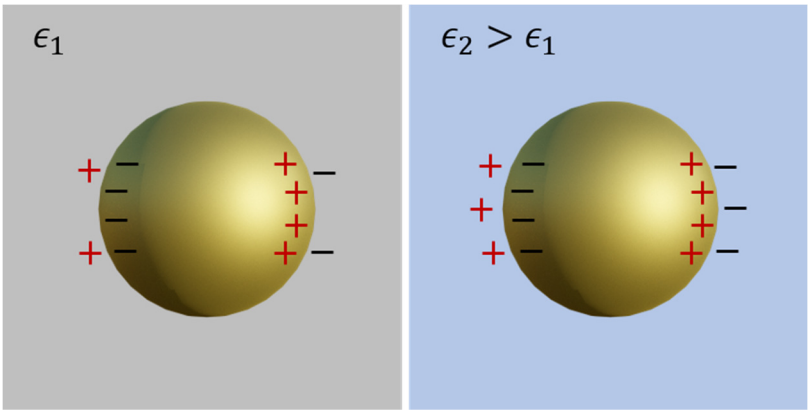

Figure 1.13. Illustration of the charge accumulation in the vicinity of the spherical nanoparticle in the media with different dielectric constants. Higher dielectric constant of surrounding medium leads to the increase of the induced charges in the medium, which can compensate the charge induced in the nanoparticle.

Larger dielectric constant (or refractive index) of the surrounding medium results in larger amount of induced changes from the polarization of medium, which eventually weakens the restoring force leading to the red-shift of the resonances, as shown in Figure 1.14.

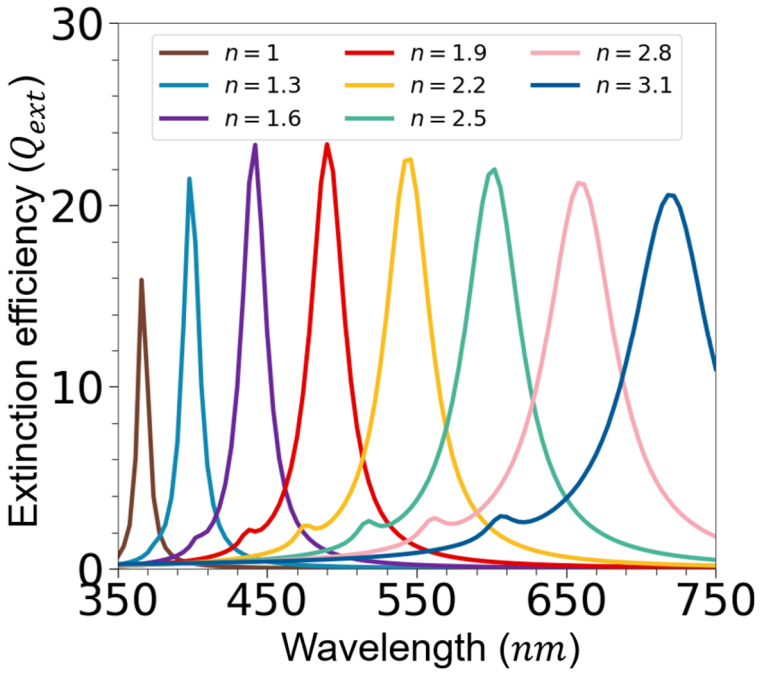

Figure 1.14. Extinction efficiencies of a silver particle with 30 nm in diameter surrounded by a medium with an increasing refractive index.

1.3.3 Short-range coupling

When nanoparticles are in close proximity, they can interact with each other through LSPR of each individual particle, inducing coupled plasmonic resonance,[82,83] whose resonance frequency is strongly modified. The modification depends on the incidence polarization, interparticle gap and the size of particle. Figure 1.15 shows the total extinction efficiency spectra of a plasmonic dimer with 50 nm in diameter, embedded in homogeneous medium with the refractive index of 2.0, and the corresponding near-field maps at the selected wavelength. As shown in Figure 1.15a, decreasing the interparticle gap leads to the red-shift of the broad dipolar resonance and a slight red-shift of the narrow quadrupolar resonance with a strong field enhancement at the featured wavelengths (Fig. 1.15b & c). In contrast, the resonance wavelength for the TM polarization is almost insensitive to the gap, and the near-field maps indicate no coupling effect.

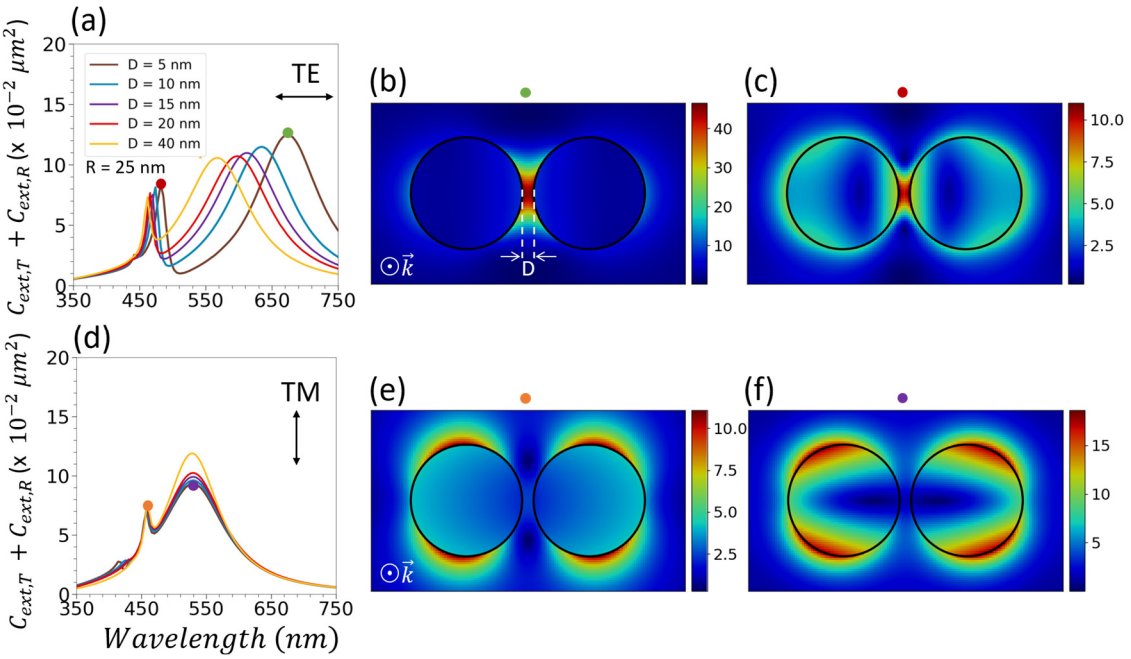

Figure 1.15. Total extinction cross-section of a dimer illuminated by TE (a) and TM (d) polarizations with the increasing interparticle gap (D). Near-field enhancement (total intensity) at the selected wavelengths for TE (b, c) and TM (e, f) polarizations. The particle size is 50 nm in diameter.

Figure 1.15 presents a further investigation concerning the short-range coupling, specifically focusing on the impact of particle size. With a fixed gap of 15 nm, an increase in particle size causes the resonances in both TE and TM to redshift. While the shift in TM polarization is primarily attributed to the dependence of the intrinsic LSPRs on the particle size, the strong redshift in TE polarization is due to the additional contribution from the increasing of the coupled plasmonic resonances, as displayed in Figure 1.16c & d.

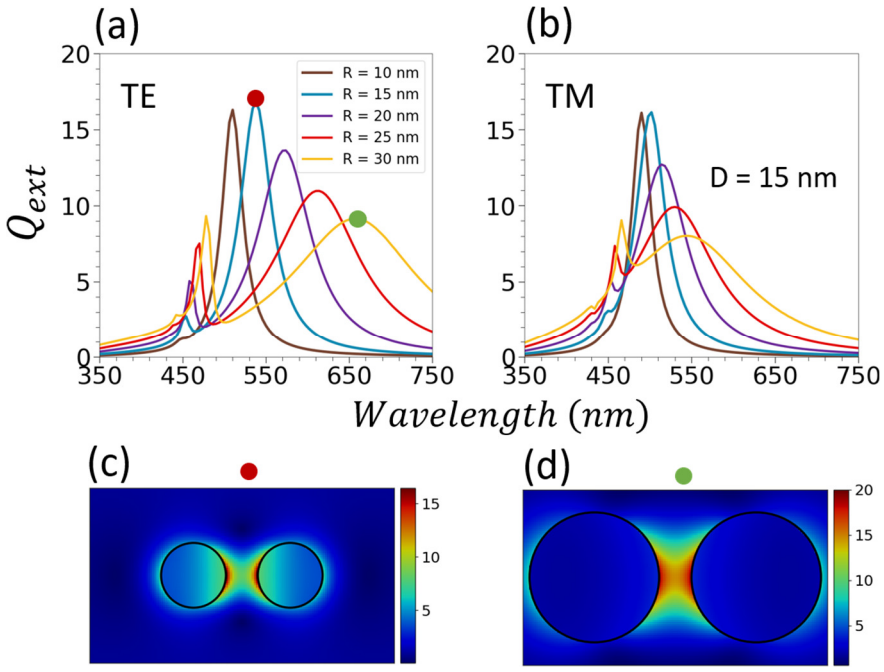

Figure 1.16. Total extinction efficiency of a dimer illuminated by TE (a) and TM (b) polarizations with the increasing particle size (R). Near-field enhancement at the resonance wavelengths for particle size of R = 15 nm (c) and R = 30 nm (d) with TE polarization. The interparticle gap is fixed at D = 15 nm.

1.3.4 Long-range coupling of regular nanoparticle array.

In addition to changing the nature of material or surrounding medium, geometrical design can also be used to tune the optical spectrum of metallic nanostructures. When metallic particles arrange in an ordered way with a distance comparable to incident wavelength, they can modify the spectral response and produce even higher quality of plasmonic resonance (as illustrated in figure 1.17), resulting from optical overlapping between localized surface plasmon resonance of individual particle and the long-range photonic modes. The long-range modes are either from diffraction waves grazing on the particle surface[22,23,84–86] or guided modes in slab waveguides.[87–93] The former is widely known as surface lattice resonance (SLR), while the latter is quasi-guided mode or waveguide plasmon polariton (WPP), depending on the coupling strength with LSPR.

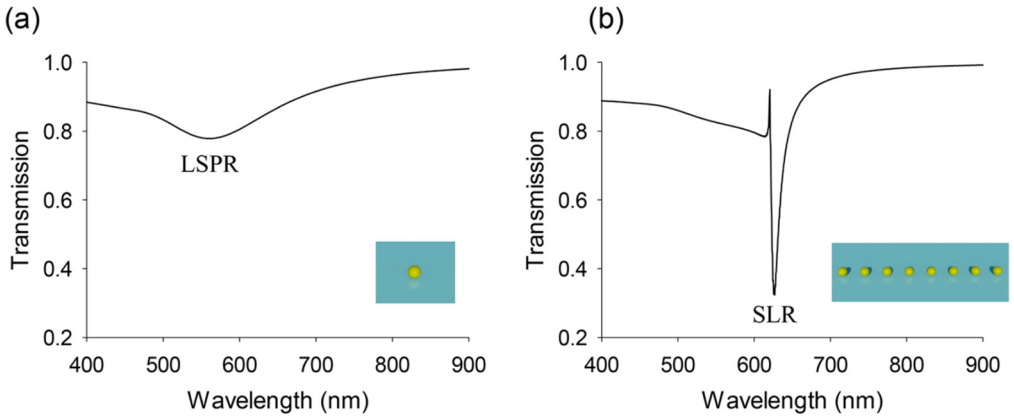

Figure 1.17. Comparison of LSPR and SLR of gold particles with 80 nm in radius and 1D array with 620 nm in period. The incident polarization is perpendicular to the array. The figure is taken from Kravets et al.[22]

SLRs have been extensively studied using coupled dipole approximation (CDA),[94,95] which were first applied by Laor and Schatz to demonstrate the surface enhance Raman spectroscopy (SERS) resulting from coupling plasmonic resonance in ensemble of metallic hemispheroid.[96] Meier et al. and Carron et al. extended the CDA model for the regular array of metallic particles.[97,98] Further works on using CDA explaining the narrow resonances that arise in both one-dimensional and two-dimensional array of nanoparticles are carried out by Markel, Zou, Schatz and co-authors.[99–101]. Mathematically, CDA enables to point out the conditions that lead to SLRs, which have been thoroughly discussed in previous studies.[102,103] Recent progresses in fabrication technique enables to observe extremely narrow SLRs in gold nanoparticle arrays.[102,104,105] The primary reason why SLRs attract so much attention in the field of plasmonics and metamaterials because of its potential in manipulating and controlling light at nanoscale and can be observed in wide range of particle shapes, including metallic holes,[106,107] nanorods,[108–110] slits,[111] disks.[103,112,113] SLR-based materials can thus be easily applied for numerous applications in lasing,[114–116], sensing,[117,118], solid state lighting,[119,120] and structural colors.[11,121,122]

Unlike SLPs, where a homogeneous surrounding medium is favored, quasi-guided modes or WPPs require a supporting waveguide layer. The plasmonic-photonic coupling results from the interaction between LSPRs of metallic particles and guided modes of the supporting layer. Therefore, controlling this interaction can be attenable by simply changing grating period of

nanoparticle array, incident angle or thickness of the waveguide layer. By doing so, Liden et al[123] showed the way to tune the suppression of the light extinction arising from the destructive interference between incident light and waveguide modes. Taking similar approach, Zentgraf and co-workers[89] demonstrated extremely high transparency in gold nanowire embedded in waveguide layer, originating from the cancelation of plasmonic resonance from the destructive interference. Christ et al.[88] also used gold nanowire array with an dielectric waveguide to demonstrate strong plasmonic-photonic coupling, enabling to achieve large Rabi splitting of 250 meV, which can be potential in photonic band gap studies. Another interesting studies on the plasmonic-photonic interaction is carried out by Rodriguez et al and Zhou et al,[124,125] where the scientists have shown how to control the strength of the coupling between LSPRs to guided modes in a slab through varying the waveguide thickness. Results from the studies can be promising for designing hybrid dielectric-metallic devices that can be used in solid-state light-emitting implementations. The hybrid structures can also find applications in many other areas, such as plasmonic color[126,127] or sensing[128–130].

1.3.5 Influence of nanoparticle inhomogeneities.

Recent advancement in self-assembly approaches[37,38,131–133] enable to realize such hybrid structures for industrial purposes that require cost-efficiency and scalability. However, fabricating perfect regular array is extremely challenging, and the nanoparticle array generated by these techniques normally suffers from inherent imperfections, such as positional disorder and size distribution of metallic nanoparticles, which may affect the quality of plasmonic-photonic resonances. Therefore, understanding these influences is crucial for the development of scalable optical devices with desired attributes. Many previous studies have been devoted to unveil the material disorder and size dispersion effect on the spectral properties.[131,132,134–138] Generally, the spatial randomization suppresses the coherent scattered field of nanoparticle array leading to the weakening of the coupling effect, manifesting itself as the increase and decrease of extinction dips and peaks respectively.[22] The weakening of the extinction peak is also observed when particle size is dispersive, related to the reduction of scattering intensity of small particles leading to low contribution to the coherent far field coupling.

In chapter 3, the influence of the inhomogeneities on the optical response will be investigate in more detail using a specific study case *i.e* the self-organized nanoparticle array induced by laser. In addition, questions about the effect of array size on optical properties and the adequacy of the simulated disorder array compared to experiment data will also be addressed.

2 Experimental techniques

This section provides a brief overview of the experimental techniques used in this thesis, including the preparation of Ag: TiO_2, continuous and nanosecond laser processing. We also show how the colors of the sample are characterized and transformed to different color spaces. Finally, it will end by showing how to print plasmonic images using laser processing.

2.1 Sample preparation

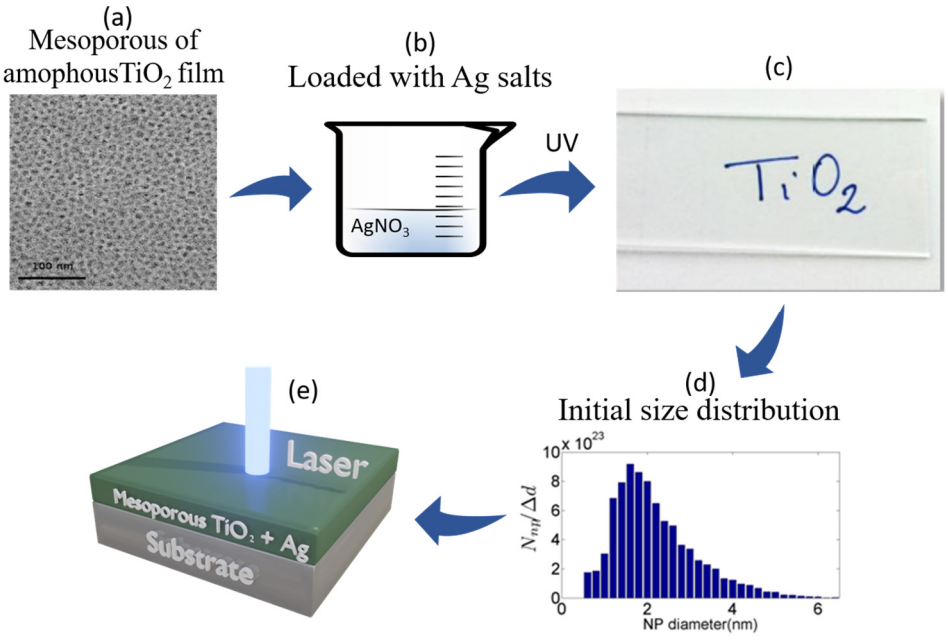

Figure 2.1. Illustration of the sample preparation process.

In the first step, the mesoporous of amorphous TiO_2 films (Fig. 2.1 a) are prepared by a sol-gel process.[139,140] The initial film contains a mixture of titanium tetraisopropoxide (TTIP, Aldrich; 97%), acetylacetone (AcAc, Aldrich; 99%), hydrochloric acid (HCl, Roth; 37%), ethanol (EtOH, Carlo Erba; absolute), Pluronic P123 (Aldrich; MW: 5000) and de-ionized water (H_2O) with the molar ratios are controlled at TTIP/P123/ethanol/HCl/H_2O/AcAc = 1:0.025:28.5:0.015:29.97:0.5. The films are dip-coated and annealed at 340℃ with the resulting thickness of 230 $\pm$ 50 nm. In the next step, silver ions are loaded into the TiO_2 films by soaking the films using an aqueous

ammoniacal silver nitrate solution (Fig. 2.1b). Then, the films are rinsed with deionized water and dried in the dark at room temperature for 12h. After being exposed to UV light (400 $\mu W.cm^{-2}$ and a wavelength of 254 nm) the films become transparent, colorless (Fig. 2.1c) and small silver nanoparticles are formed with the initial size distribution around 2nm (Fig. 2.1d). Before being processed by laser (Fig. 2.1e), the films are stabilized with UV-Visible light cycles to achieve color stability.[139,140]

2.2 Laser printing set-ups

After the preparation, the films are now ready for laser processing. The materials undergo several physicochemical processes during laser exposure, which result in nanoparticle growth and sample modification.[49,50] The resulting samples strongly depend on the laser parameters and of course, the type of laser used. Nanosecond lasers can generate high peak power with low average power when compared to continuous lasers, which have a relatively higher constant laser power. Using different lasers, therefore, can lead to very different opto-structural properties,[47,52,53] which will be discussed by studying the optical properties of samples illuminated by continuous laser in Chapter 3 and by nanosecond laser in Chapter 4. This section will be followed by the introduction of using continuous laser and nanosecond laser.

2.2.1 Continuous laser

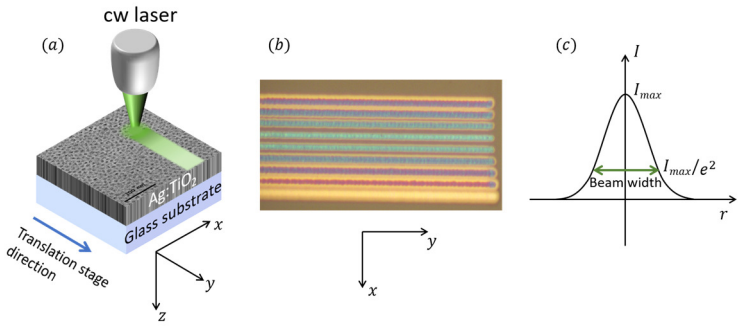

Figure 2.2. (a) Illustration of the cw laser setup. The sample is fixed on the translation stage illuminated by a Gaussian laser beam which is normal to the sample surface. (b) Laser marking lines at 9 different

focuses with a constant scan speed of 800 mm/s and laser power of 280 μW. (c) Gaussian beam profile and the definition of the beam width at $1/e^2$ of the maximum intensity.

For the continuous laser setup, we use an Ar-Kr CW laser with a slight focus under normal incidence on the sample surface by a 10x microscope objective (Olympus MPlan N, N.A 0.25). The samples are placed on a translation stage and moved at constant speeds as illustrated in Fig. 2.2a. The wavelength of laser beam can vary from 457 nm to 647 nm and the intensity of the laser beam has a Gaussian shape with the beam width (at $1/e^2$ intensity) is measured at around 12.7 μm (Fig 1.14c). The beam width can be tuned by moving the translation stage along z-axis, which can modify the sample differently. Figure 2.2b shows illustration of laser inscription of nine induced lines with different focuses while keeping laser power and scan speed constant. The change of the sample due to the variation of laser focus results in different color appearances.

2.2.2 Nanosecond laser

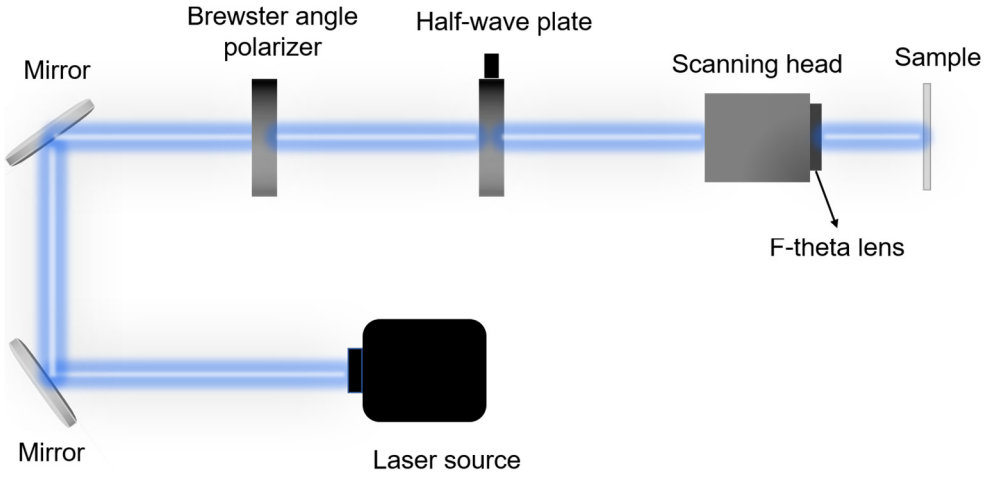

Figure 2.3. Sketch of nanosecond laser setup.

A nanosecond fiber laser, with a pulse duration of 1.3 nm at 532 nm from IPG photonics, is used to scan on the material surface equipped with a galvanometric mirror scanner head (Sunny Technology). The laser is focus on the sample by using a 16 cm F-Theta lens with a focused laser spot size of 13.5 μm and is linearly polarized using a Brewster angle polarizer, where the

polarization can be controlled by using a half-wave plate (as shown in Fig. 2.3). The laser fluences can be calculated from the relation:

$$F = \frac{2P}{f_{rep} \times \pi r^2} (J/cm^2) \tag{2.1}$$

with P is laser power, $f_{rep}(Hz)$ is the repetition rate, r is the beam radius at $1/e^2$.

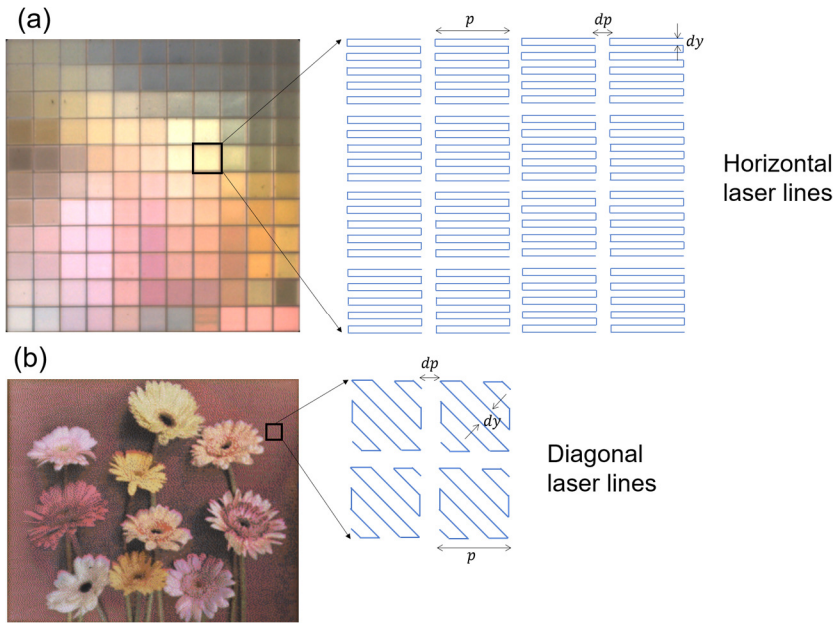

Figure 2.4. Description of laser marking lines. (a) Illustration of horizontal laser marking lines with distance between the lines is dy. (b) Illustration of diagonal laser marking lines with the distance between the lines is dy.

To mark on the sample surface, CS Mark (Sunny technology) commercial software is used to control the laser beam and scanner head, which can tune laser power, scan speed, and repetition rate. Dots, lines, rectangles, and circles are some of the marking shapes that can be drawn. In this thesis, we only use lines to draw our color databases or plasmonic images; drawing with dots can be found in Dalloz et al.[38] Figure 2.4 illustrates laser marking lines, where each pixel (with the size of p) is printed by marking laser lines with the inter-distance of dy, oriented along horizontal axis (Fig. 2.4a) or diagonal axis (Fig. 2.4b). The distance between each pixel is dp.

2.3 Color characterization

2.3.1 Color acquisition

Colors of the sample are measured using a homemade setup, where an RGB camera (Basler ac2500-14gc) equipped with a telecentric lens captures the image of the sample. Sample can be illuminated by a light source in transmission side or reflection side with an incidence angle of 0° and 16° respectively. In this setup, the light sources are fixed while the sample can be rotated around x-axis to change the incidence and observation angles (Fig. 2.5). Thus, in transmission mode, both angles are equal to 0° while in reflection mode, they are equal to 16°. When measuring sample dichroism, an analyzer is added between the sample and the telecentric lens with the optical axis parallel to the yz-plane. Two polarized images (in transmission or reflection modes) are taken with the optical axis being parallel to yz-plane and xy-plane. In diffraction mode (the analyzer is not used), sample can rotate around x-axis so that the -1 diffraction order from the sample can be captured by the camera with the same light source in reflection mode. The front and back side reflection modes correspond to the configuration when the superstrate and substrate are facing with the light source respectively.

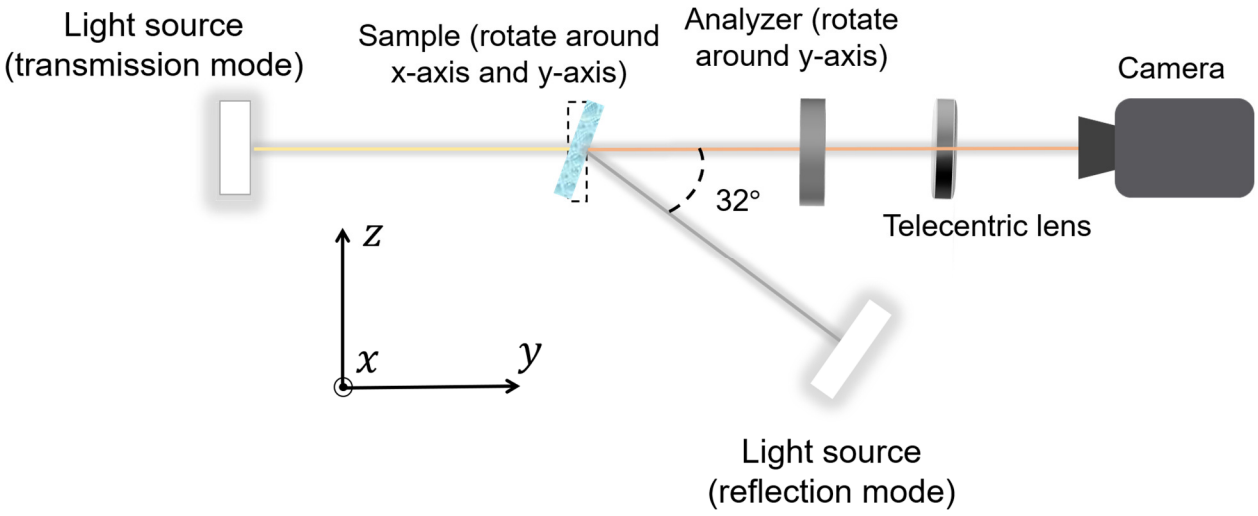

Fig. 2.5. Color acquisition setup. The setup is depicting the reflection mode, the transmission mode corresponds to the sample when it aligns with the dashed rectangle.

2.3.2 Color transformation[141,142]

The colors captured by the camera are represented in RGB color space. However, there is interest in converting RGB color space to L*a*b* because the latter is designed to match with human vision and is device-independent, making it ideal color space to work with for color management and color matching applications.

The first step is to convert the measured RGB to three tristimulus values XYZ using the relation as followed:

$$\begin{bmatrix} \mathrm{X} \\ Y \\ Z \end{bmatrix} = \begin{bmatrix} 0.412453 & 0.357580 & 0.180423 \\ 0.212671 & 0.715160 & 0.072169 \\ 0.019334 & 0.119193 & 0.950227 \end{bmatrix} \begin{bmatrix} \mathrm{R} \\ G \\ B \end{bmatrix} \tag{2.2}$$

The chromaticity (x, y) can be derived from the tristimulus values as:

$$x = \frac{X}{X+Y+Z}, y = \frac{Y}{X+Y+Z} \tag{2.3}$$

Finally, L*a*b* color space can be calculated using the following equations:

$$\begin{cases} L^* = 116F\left(\frac{Y_i}{Y_n}\right) - 16 \\ a^* = 500\left(F\left(\frac{X_i}{X_n}\right) - F\left(\frac{Y_i}{Y_n}\right)\right) \\ b^* = 200\left(F\left(\frac{Y_i}{Y_n}\right) - F\left(\frac{Z_i}{Z_n}\right)\right) \end{cases} \tag{2.4}$$

where

$$F(t) = \begin{cases} t^{\frac{1}{3}}, & t > \left(\frac{6}{29}\right)^3 \\ \frac{1}{3}\left(\frac{29}{6}\right)^2 t + \frac{4}{9}, \text{otherwise} \end{cases} \quad (2.5)$$

In the above equation, L^* represents the lightness of the color a^*, b^* correspond to the color positions between red and green, yellow and blue respectively, and $X_n = 95.0489, Y_n = 100, Z_n = 108.8840$ are three tristimulus values of the D65 illumination.

2.4 Sample characterizations

2.4.1 AFM

Sample surface topography are measured using a Bruker Icon atomic force microscope (AFM). The AFM functions on the principle of force-based scanning probe microscopy. Its key components include a sharp, atomically terminated tip attached to a flexible cantilever and a precisely controlled piezoelectric scanning stage. The tip interacts with the sample surface, and the resulting mechanical forces are transduced into electrical signals via the deflection of the cantilever. These signals are subsequently processed to create topographic images of the sample with sub-nanometer resolution.

In this thesis, AFM is used to attain the three-dimensional surface morphology and cross section surface profile to reveal the periodicity of the investigated surface as shown in Figure 2.5.

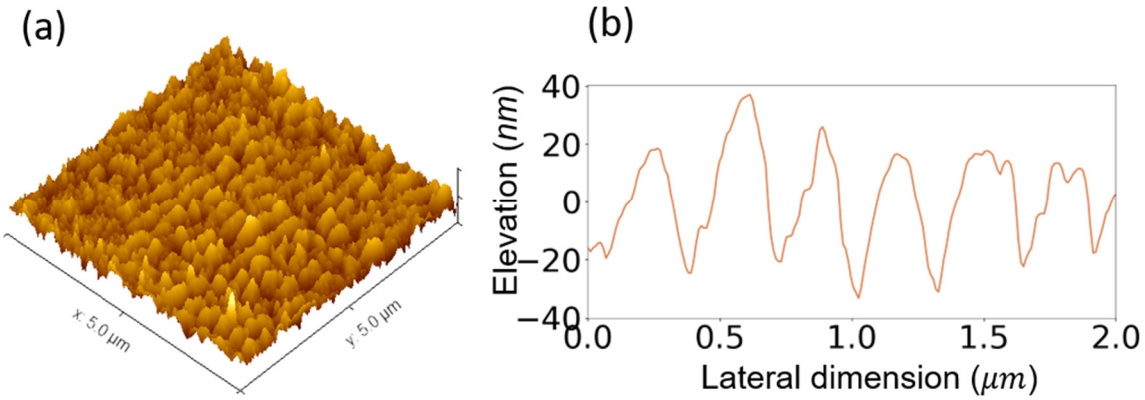

Fig. 2.5. an AFM 3d surface topography and the corresponding surface profile.

2.4.2 SEM

The top views of the samples in this thesis are measured with a FEI Nova nanoSEM 200 scanning electron microscope (SEM) in low vacuum mode with a helix detector. Its working principle involves the emission of a focused electron beam onto the sample surface. When the electrons in this beam interact with the specimen, various signals are generated, including secondary electrons (SE) and backscattered electrons (BSE). The Nova nanoSEM 200 utilizes detectors to capture these signals, with SEs providing detailed topographic information for surface imaging, and BSEs offering compositional contrast. An example of sample top view captured using the SEM is shown in Figure 2.6.

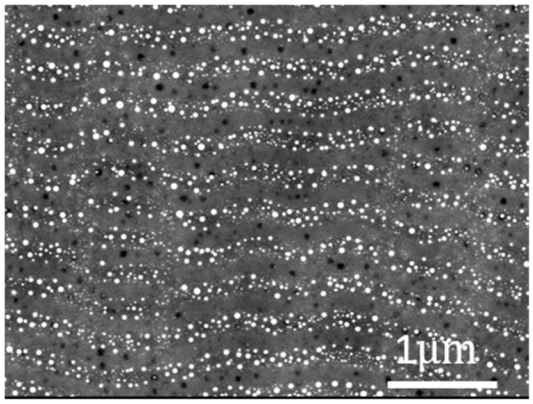

Fig. 2.6. Top view SEM image.

2.4.3 STEM

Cross-sections of the samples are characterized using Jeol Neo ARM 200F, operating by focusing a high energy electron beam onto a specimen, enabling sub-angstrom probe sizes for precise imaging. As the electrons interact with the specimen, they undergo various scattering processes, generating transmitted electrons that form diverse types of scanning transmission electron microscopy (STEM) images, such as bright-field, dark-field and high-angle annular dark-field images.

The cross-sections are taken at 200kV and the lamellas suitable for top-view imaging were fabricated using the FEI Helios 600i instrument via focused ion beam (FIB) techniques. Figure 2.7 shows examples of top view and cross section of a sample.

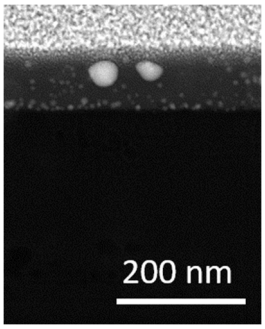

Fig. 2.7. (a) Plane-view and (a) cross-section HAADF-STEM images.

2.4.4 EDS

The Jeol Neo ARM 200F, equipped with a series of Jeol detectors (Jeol-EDS SDD), Gatan devices, and various sample holders, enables the acquisition of energy-dispersive X-ray spectroscopy (EDS) mappings for elemental composition analysis. The fundamental working principle behind EDS involves the capture of characteristic X-rays emitted by a specimen upon electron beam excitation. These emitted X-rays are efficiently collected by a semiconductor detector and subsequently converted into electrical signals. Within the EDS analyzer, these signals are further

processed, transformed into pulse currents, where their amplitudes correspond to the energies of the detected characteristic X-rays. These currents are measured through a multi-channel pulse-height analyzer, with each channel associated with a specific element. The resulting EDS spectrum provides precise quantitative data on the elemental composition of the specimen, facilitating nanoscale elemental analysis and mapping, as illustrated in Figure 2.8.

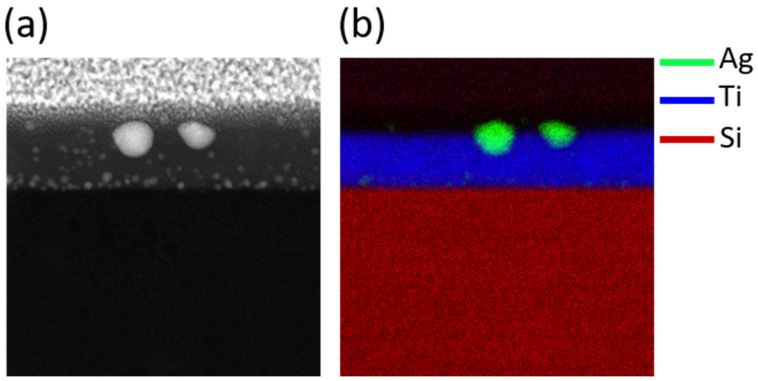

Fig. 2.8. (a) Cross-section HAADF-STEM image and (b) EDS chemical analysis.

3 Hybridization between plasmonic and photonic modes in laser-induced plasmonic metasurfaces

Plasmonic metasurfaces made of perfectly regular 2D lattices of metallic nanoparticles deposited on surfaces or close to waveguides can exhibit hybridized plasmonic and photonic modes. The latter arise from the excitation of surface or guided modes through the coherent scattering of periodic arrays. Recently, laser induced self-organization of random plasmonic metasurfaces has been used to create nanoparticle gratings embedded in protective layers.[37,38] Despite the broad size distribution and positional disorder of nanoparticles, the resulting nanostructures exhibit strong coupling between plasmonic and photonic modes in transverse electric polarization, leading to dichroism, which is well-reproduced from one laser printing to another. Here, we examine quantitatively the effect of inhomogeneities at the nanoscale on the hybridization between localized plasmonic modes and delocalized photonic modes by considering realistic laser-induced self-organized nanoparticle arrays embedded in a two-layer system. By referring to regular samples, we describe the optical mechanisms involved in the hybridization process at characteristic wavelengths, based on far and near field simulations. Two kinds of real samples are considered, featuring different levels of coupling between the plasmonic and photonic modes. The results demonstrate that controlling the statistical properties of plasmonic metasurfaces, such as the nanoparticle size distribution and average position, over areas a few micrometers wide is enough to control in a reproducible manner the hybridization mechanisms and their resulting optical properties. Thus, this study shows that the inherent irregularities of laser-induced self-organized nanostructures are compatible with smart functionalities of nanophotonics, and confirms that laser processing has huge potential for real-world applications.

3.1 Introduction

A regular arrangement of metallic nanoparticles can produce a coherent scattered light. The latter may couple to guided modes of a waveguide or generate diffracted orders grazing on the plane of the nanoparticle array. These excited photonic modes may then interact with localized surface

plasmon resonances (LSPRs) of individual nanoparticles to create hybrid plasmonic photonic states.[22,23,86–89,92,118,123] Tailoring this coupling effect enables the design of biosensing materials,[118,129] refractive index sensors,[143] photovoltaic devices[144] or light emitting diodes.[145,146] In addition, the interaction of resonance modes can modify the spectra at visible wavelengths and be used for color applications.[11,40,121,122,147–149] Many efforts have been devoted to the development of nanofabrication techniques to utilize these hybrid plasmonic photonic materials in large-scale industrial applications.[131–133,143,150,151] Recently, lasers have been employed to produce nanomaterials that support hybrid modes and, which demonstrated high performance for a secured color printing technique referred as printed image multiplexing. Up to four multiplexed images were encoded in a single metasurface for four independent visual observation conditions under white light.[37,38] This ability to encode multiplexed images results from the dichroic properties of the laser processed samples, which exhibit self-organized silver nanoparticle arrays embedded in a high index thin film.[47,52,53] The advantages of using laser-based techniques are their scalability, cost-effectiveness and flexibility. Unfortunately, the resulting nanoparticle arrays normally suffer from intrinsic imperfections from self-organization processes, which include size dispersion and spatial disorder. Despite this randomness at the nanoscale, the optical properties of samples at the macroscopic scale, such as their color in specific observation modes or their dichroism, are reproducible from one laser printing to another when the processing parameters are maintained constant. The effects of randomness at the nanoscale in these laser-induced systems on the electromagnetic coupling are not yet clear and remain an open question. In order to continue to develop applications of laser-induced nanomaterials, it is important to determine how tolerant their optical responses are to the intrinsic inhomogeneities of the laser process.

In this chapter, we demonstrate the existence of hybrid plasmonic and photonic modes in self-organized quasi-random plasmonic metasurfaces generated by continuous wave laser despite the presence of structural inhomogeneities. Experimental spectra are compared to simulation results where real-like structures are considered. A numerical study performed on real-like structures and regular structures, in which array size, spatial disorder and size dispersion are progressively increased, is carried out to estimate their impact on the structure optical response and prove the sufficiency of real-like sample in reproducing the statistical properties of the real material. The comparison with experimental results then allows to quantify the effect of inhomogeneities in the

laser-induced metasurfaces. The chapter then highlights the different plasmonic and hybrid modes that shape the visible spectra and compare the coupling effect in real-like and regular structures at the near-field scale. Two real samples are investigated, which exhibit different nanoparticle size distributions and support different degrees of coupling, to show that this laser technique can control the coupling strength by simply tuning the processing parameters. The laser-based method reported here shows great potential for mass manufacturing of nanomaterials with smart functionalities, which can be applied to anti-counterfeiting or other security purposes.

3.2 Laser-induced self-organized nanoparticle arrays

Mesoporous films of amorphous TiO2 containing silver ions and nanoparticles (NP) are processed by a continuous wave (cw) laser slightly focused on the film and moving at a constant speed. Two laser-processed samples are investigated in this chapter since they exhibit very different nanoparticle size distributions and average nanoparticle grating periods. The first one (Figure 3.1a) is irradiated at 488 nm wavelength and the second one, investigated later in the chapter, at 647 nm. Experimental details are given in the Chapter 2.[47,152] As shown in Fig. 3.1a, the laser processing induces the growth of silver nanoparticles with a broad size distribution (Figure 3.2a) along a self-organized periodic structure, whose average period is $\Lambda_x = 300 \pm 40$ nm. Silver nanoparticles are embedded in an intermediate thin film made of a blend of SiO_2, from the substrate, and TiO_2 from the initial mesoporous film (Figure 3.1b and Figure 3.2c). The average thickness of this film is $d_2 = 100$ nm. This intermediate layer is covered by a layer containing TiO_2, mainly in the form of anatase nanocrystals (Figure 3.2c). The origin of such self-organized nanostructures and the mechanisms leading to this broad size distribution were discussed in some of our previous papers.[49,50,152–154] The present chapter focuses on the study of the influence of the array size, size dispersion and spatial disorder at the nanoscale on the optical responses of these laser-induced self-organized metasurfaces. The present sample exhibits a strong dichroism in transmission with a spectrum showing a single broad dip at 480 nm wavelength for TM polarization (perpendicular to the grating lines) and two dips at 440 nm and 580 nm for TE

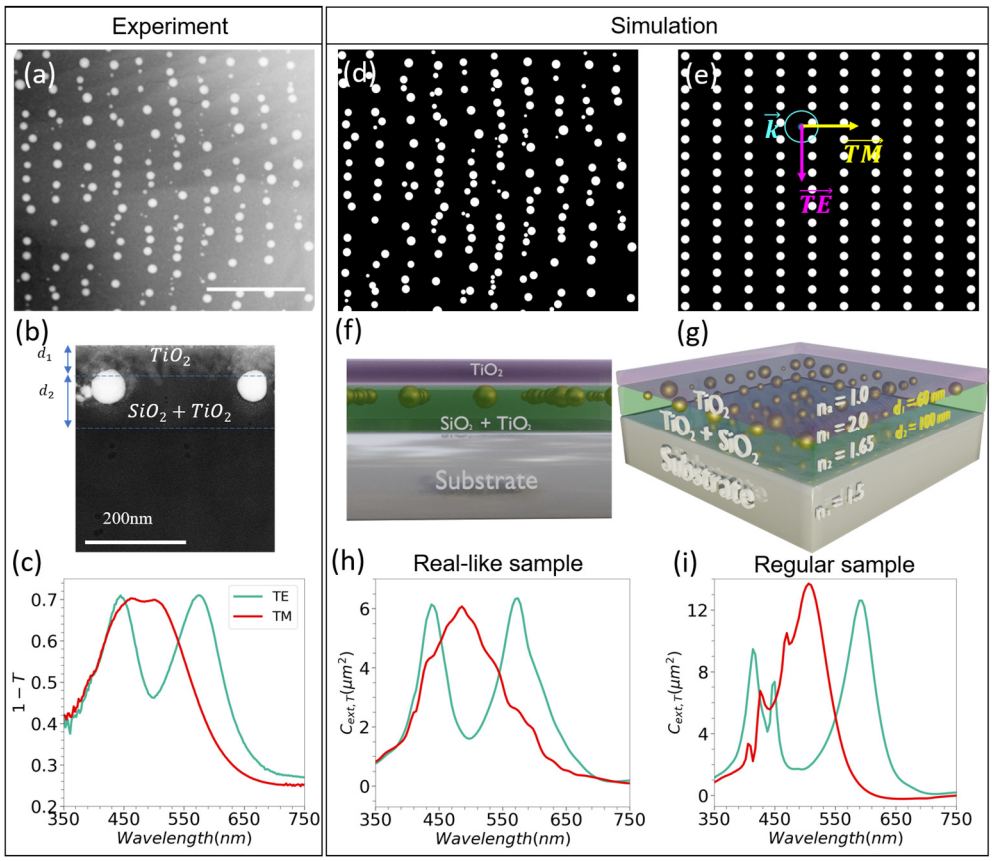

Figure 3.1. (a-b) Transmission electron microscopy micrographs of a Ag NP:TiO_2 metasurface induced by cw laser at 488 nm wavelength. (a) Plane and (b) cross-section views of the sample. A two-layer system appears above the glass substrate. The top layer contains mainly TiO_2 nanocrystals and the intermediate layer is made of silver nanoparticles (in white) embedded in a blend of SiO_2 and TiO_2. (c) Extinction, which is calculated as 1 – T (Transmission coefficient), of the sample measured for TE (electric field parallel to the grating lines) and TM polarizations under normal incidence. (d) Plane view (imported from Fig. a), (f) cross-section and (g) 3D view of the real-like sample used in the simulations. All nanoparticles are inside the intermediate layer and tangent to the top layer interface. (e) Plane view of the regular sample used for comparison. The latter has the same layer structure as the real-like sample except that the nanoparticle array is periodic with periods along x-axis and y-axis of Λ_x = 300 nm and Λ_y = 180 nm and the nanoparticle diameter equals 90 nm. In regular sample, Λ_x is chosen to be equal with the average periodic of the grating lines of realistic sample, while Λ_y is chosen to have a consistent simulation results with the realistic sample. The vectors represent the incident wave vector and the two considered polarizations. (h-i) Calculated extinction cross sections in transmission side of (h) the real-like sample and (i) the regular one for TE (blue) and TM (orange) polarizations. The scale bar in (a) is 1 µm and is the same in (d) and (e).

polarization (Figure 3.1c). This spectrum can be reproduced at different places on the sample by using the same laser processing parameters. It is therefore independent of the particular ensemble of nanoparticles induced with a certain randomness by the 12.8 µm wide laser beam (diameter at $1/e^2$), and only dependent on statistical properties of the quasi-random nanostructures.

In order to investigate the optical properties of the material, we create a model with a realistic sample that reproduces the layer structure and the nanoparticle distribution of the real sample (Figure 3.1d and Figure 3.1f-g). The refractive indices of the two layers are optimized to match

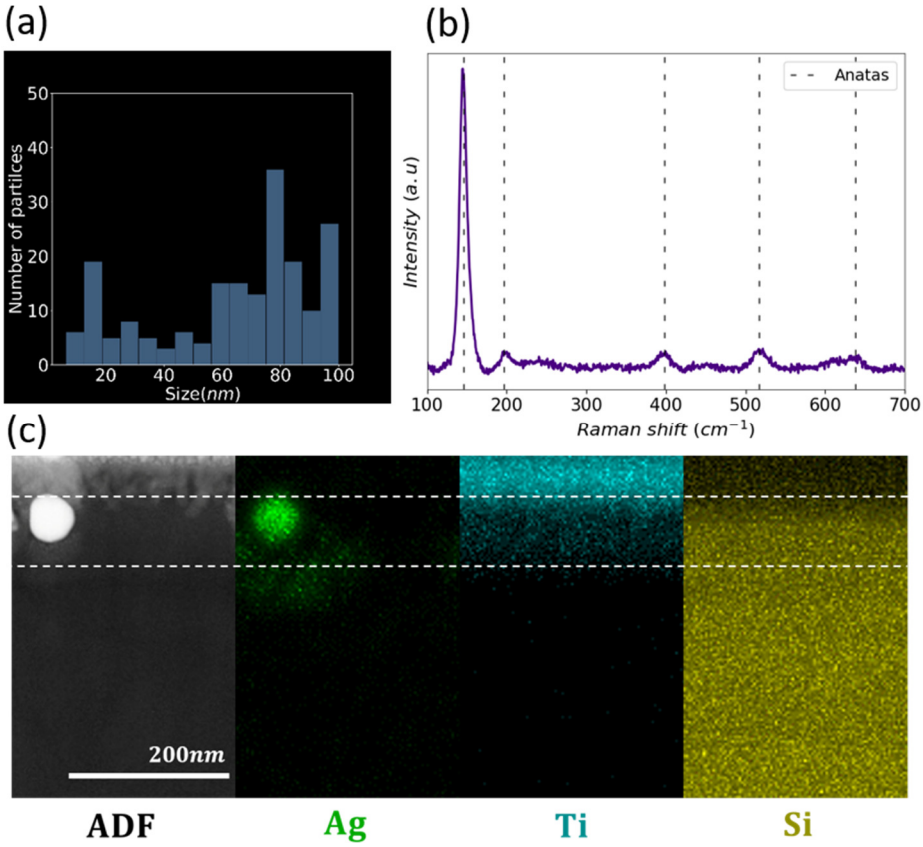

Figure 3.2. (a) Size distribution. (b) Raman spectrum of the sample after background removal.[155,156] (c) Chemical analysis of the sample cross-section by annular dark field (ADF) electron microscopy and energy-dispersive spectroscopy that highlights Ag, Ti and Si atomic content. Dashed white lines indicate the layer interface. Sample irradiated by the laser at wavelength of 488 nm, power of 250 mW and scan speed of 300 µm/s

the simulations with the experimental results, while being coherent with the information given by Raman spectroscopy and energy dispersive microscopy (Figure 3.2b & c). The simulated extinction cross-section spectra of the realistic sample are shown in Figure 3.1h and are consistent with the experimental results of Figure 3.1c. These results and those of Figure 3.3, where the

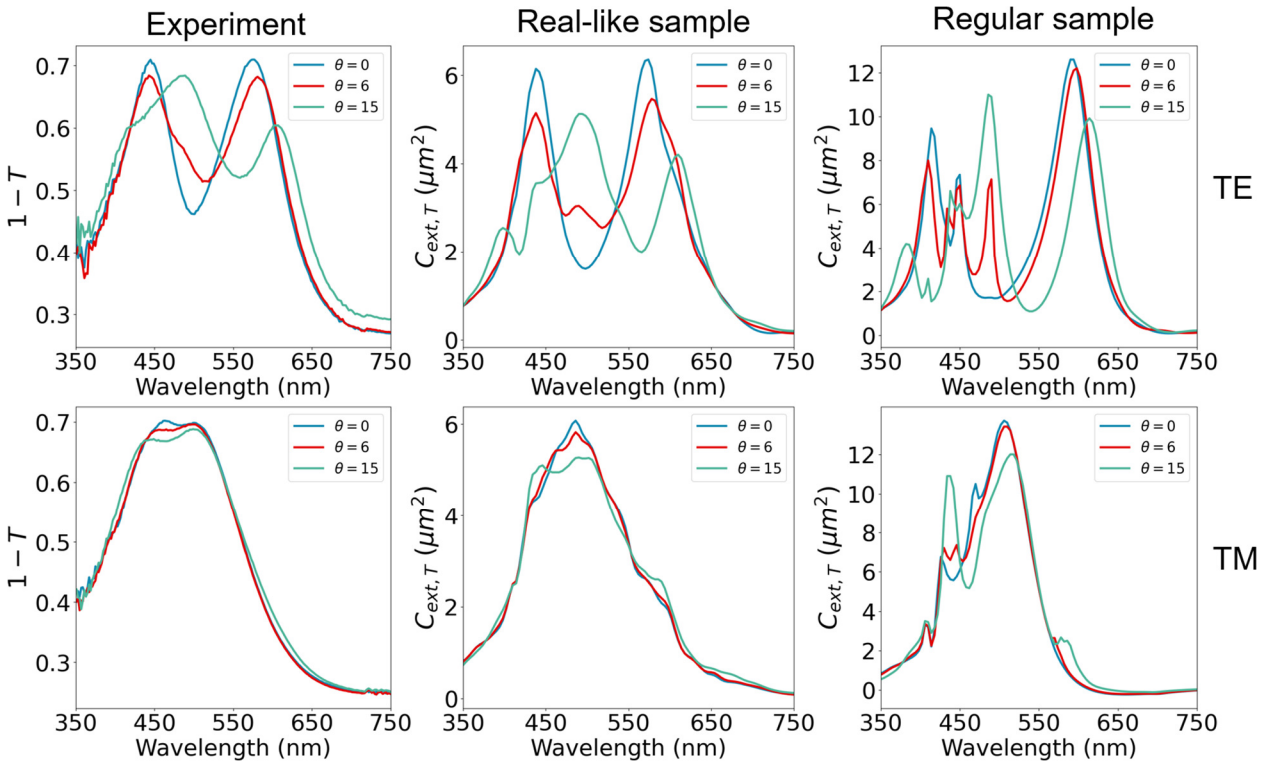

Figure 3.3. Experimental extinction of the real sample (1 - T) and simulated extinction cross section in transmission side of the real-like and regular samples for TE and TM polarization under different incidence angles.

incidence angle is varied, confirm the choice of the refractive index values in the simulations, which are 1.50 for the glass substrate, 1.65 for the intermediate layer and 2.00 for the top layer (Figure 3.1g). A regular structure is then considered to better highlight, later on, the underlying phenomena at the origin of the observed dichroism in the laser-induced samples (Figure 3.1e). This regular structure has the same parameters as the realistic sample except that the nanoparticle array is periodic, and the nanoparticle diameter is fixed as described in the caption of Figure 3.1. The spectral variations of the extinction cross section of the regular sample exhibit multiple shoulder peaks (Figure 3.1i), attributed to the multipolar resonances of the metallic particles

(Figure 3.4). Their absence in the spectra of the realistic and true samples is due to the inhomogeneity broadening. The strong dichroism that occurs in the self-organized metasurface originates from the coupling between plasmonic and photonic modes, as will be further discussed when studying the near field. In the next section, we investigate the influence of total array size on

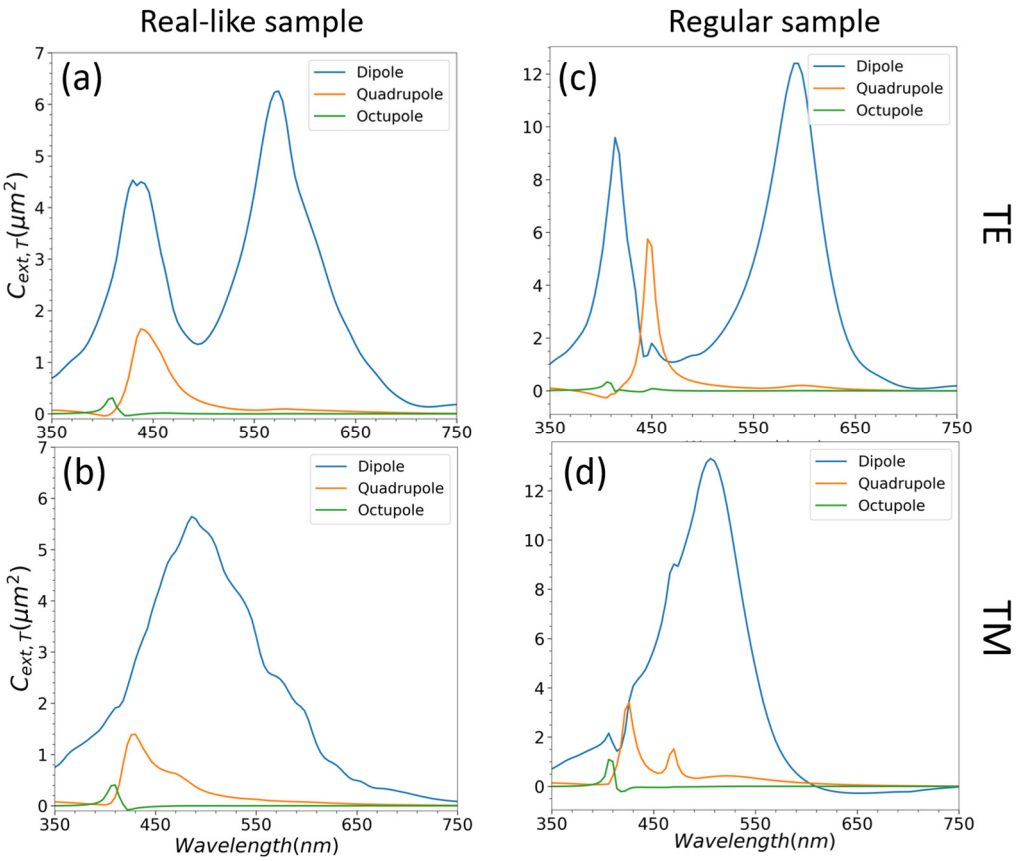

Figure 3.4. Multipole decomposition of the extinction cross-section for TE and TM polarization of real-like sample (a-b) and regular sample (c-d) respectively.

the optical responses, the array sizes required for the study of hybridization at different level of disorders, and how spatial disorder and size distribution affect the coupling effects.

3.3 Effect of the opto-structural parameters on collective resonances

Here, we would like to highlight that imperfections inherent to laser-induced structuring are compatible with the excitation of collective resonances. The first question that arises when doing electromagnetic simulations of NP assemblies is to know how many NPs should be considered to

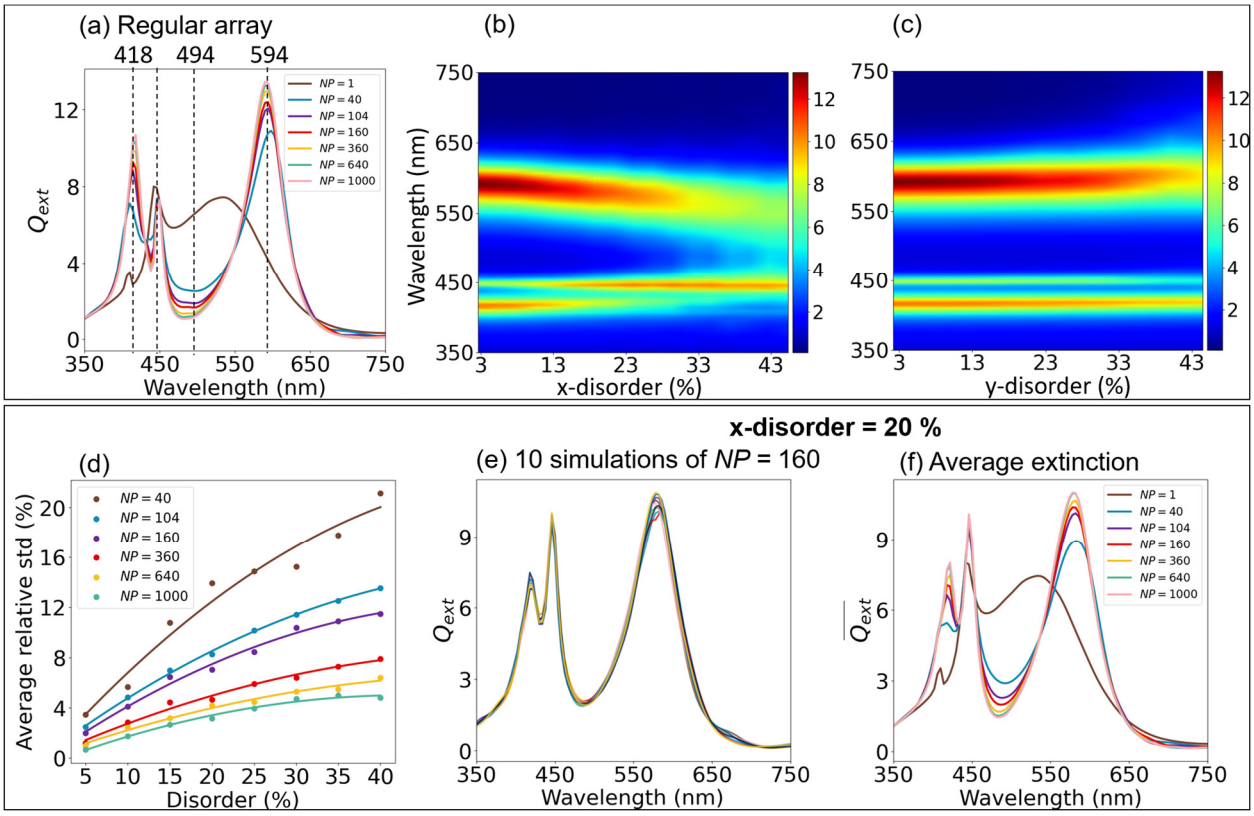

Figure 3.5. Spectral variations of the extinction efficiency for TE polarization. (a) for various number of particles of the regular array. The number of particles in x and y is set to have approximately a square array and the array periods are kept at Λ_x = 300 nm, Λ_y = 180 nm. The particle diameter is 90 nm. (b-c) Extinction efficiency for arrays (described in Figure 3.6) where the positional disorder increases along x-axis and y-axis respectively from 1 to 5. (d) Relative standard deviation of extinction efficiency for each array size as a function of degree of disorder. (e) Extinction efficiency of ten different simulations of array with NP = 160 and x-disorder = 20%. (f) Average extinction efficiency of TE polarization (ten simulations for each array size) at x-disorder = 20%.

provide reliable simulation results. Figure 3.5a shows the extinction efficiency $Q_{ext,T}$ of regular matrices for different numbers of NPs per array. $Q_{ext,T} = \frac{C_{ext,T}}{N_p * \pi R^2}$, where $C_{ext,T}$ is the extinction cross-section in transmission side, N_p is the number of the particles in the array and R is the particle radius. It allows to better compare the results obtained for different numbers of NPs. When increasing the number of particles in the regular array, the peaks at 418 nm and 594 nm become more pronounced as well as the dip at 494 nm, evidencing the collective behaviors of the NPs array at these wavelengths. On the other hand, the peak at 447 nm, which is attributed to the quadrupolar resonance, remains insensitive to the array size. In addition, the optical response starts to reach the saturation at array of NP = 640. Therefore, in the next simulations introducing spatial disorder and size distribution (Figure 3.5b, c & Figure 3.7), the particle number is set to 640.

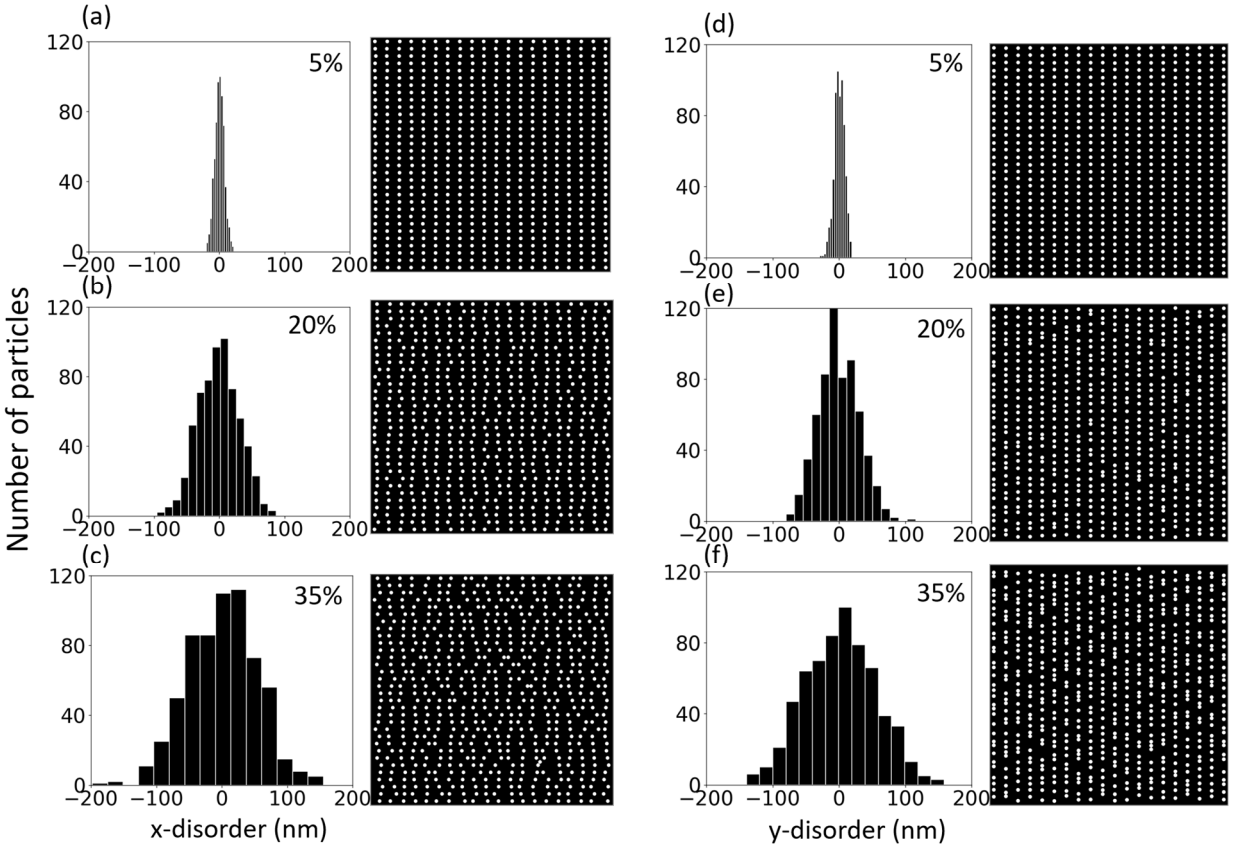

Figure 3.6. Introduction of disorder in the regular structure. Histogram of the distance from the periodic array of the nanoparticle center along x or y and the spatial distribution of silver nanoparticles in the simulated structure. The disorder is increasing from the top to the bottom row by broadening the position histograms (5 – 35%) for x-disorder (a, b, c) and y-disorder (d, e, f), respectively.

Spatial disorder is introduced by a random displacement of each nanoparticle along the x or y axis (Figure 3.6). An increase in the spatial disorder corresponds to a wider standard deviation of the displacement histograms in x and or y. Simulations (Figure 3.5b) show that when the x-disorder increases, the extinction efficiency at 418 nm and 594 nm attenuate and shift toward the position of the dip, and extinction efficiency of the dip at 494 nm increase. At high level of disorder, the peaks and dip start to merge together and the extinction spectrum tends more and more to the one of a single nanoparticle. The long wavelength peak is characteristic of a hybrid plasmonic resonance and corresponds to a strong enhancement of the absorption by the LSPR at a wavelength where constructive interferences occur between the waves scattered by each period in the sample plane. These constructive interferences are due to fact that the field scattered by the NPs arrives in phase with the incident field on the adjacent NPs.[22] The higher the disorder, the more random is the phase difference between the scattered fields by the rest of the array and the incident field on each NP, which reduces the collective effect on the absorption enhancement. Conversely, the relative amplitude of the quadrupolar resonance (at 450 nm) slightly increases to reach the one of a single particle. In contrast to x-disorder, increase the disorder in y-axis doesn't change the positions of the peaks and dip (Figure 3.5c). Even the extinction of the peaks at 418 nm and 594 nm is slightly decreased, the dip at 494 nm remain visible regardless of the y-disorder. This behavior is very similar to the size distribution shown in Figure 3.7. Because of the small particle size in the size distribution simulation, the quadrupolar mode is absent, and the width of the resonance peak is narrower linked to the decreased radiation damping of the resonance.[65,157] The results from Figure 3.5b, c and Figure 3.7 demonstrate that the regularity along the x-axis is the most crucial parameter that govern the coupling behavior when compared to the others. Therefore, in the following investigations we will vary particles along x-axis while keeping particle size (D = 90 nm) and y-disorder = 0%.

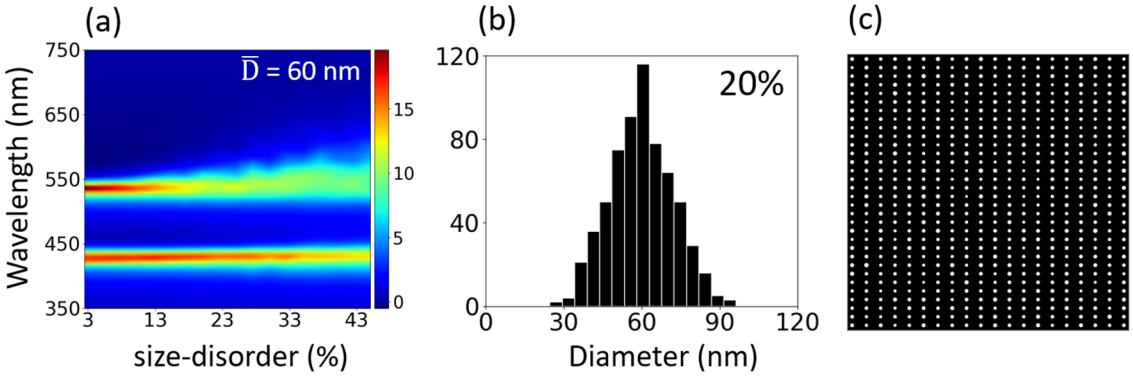

Figure 3.7. (a) Extinction efficiency for size distribution with the mean diameter of 60 nm. (b, c) Histogram and nanoparticle array of 20% size disorder, respectively. The higher disorder corresponds to broader histogram. When varying the size, we keep the regular position of nanoparticles.

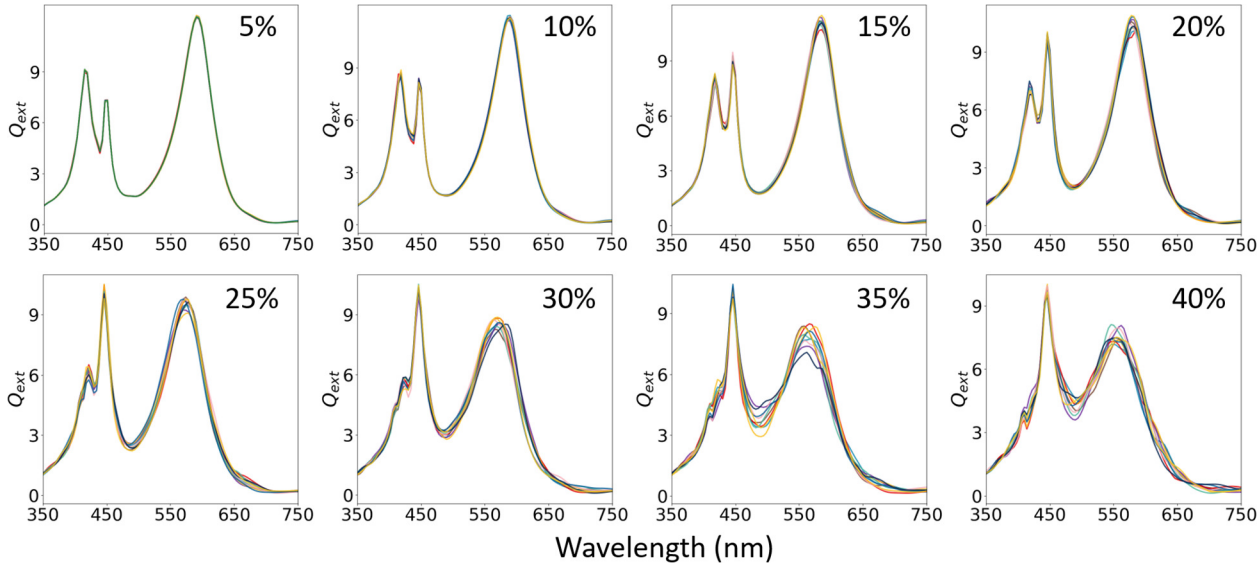

Figure 3.8. Spectral variation of ten different NP = 160 arrays at each degree of disorder, with increasing x-disorder from 5% to 40%.

When disorder increases, the results start depending on the particular arrangement of NPs considered in an array. The higher the array size, the more reproducible is the simulated spectrum for different arrangements with the same degree of disorder. To limit the calculation time, we limit the NP number per array to 1000 and we average over 10 different arrangements. Figure 3.5d gives an estimate of the error with which the average spectra for a given x-disorder is calculated when considering various NP numbers per array. This error is calculated by using the relative average

standard deviation of the calculated spectra. Ten simulations with different spatial distributions are carried out for each disorder value and array size (see Section 7.1 for detail equations). As shown in the figure, to maintain reliable simulation results when the disorder increases, higher numbers of NPs must be considered in the arrays. Figure 3.5e show 10 spectra calculated with different arrangements and the same degree of disorder (20 %) and NP number (160), which corresponds to an average relative error of 7 %. Figures 3.8 and 3.9 provide further simulations about the spectral variation as a function of disorder and array size, respectively. Figure 3.5f, which can be compared to Figure 3.5a, shows the average spectra simulated for 20 % of x-disorder and an increasing number of NPs. The spectra converge from 640 NPs and the difference between 160 NPs and 640 NPs corresponds only to an average relative error of 4.5%.

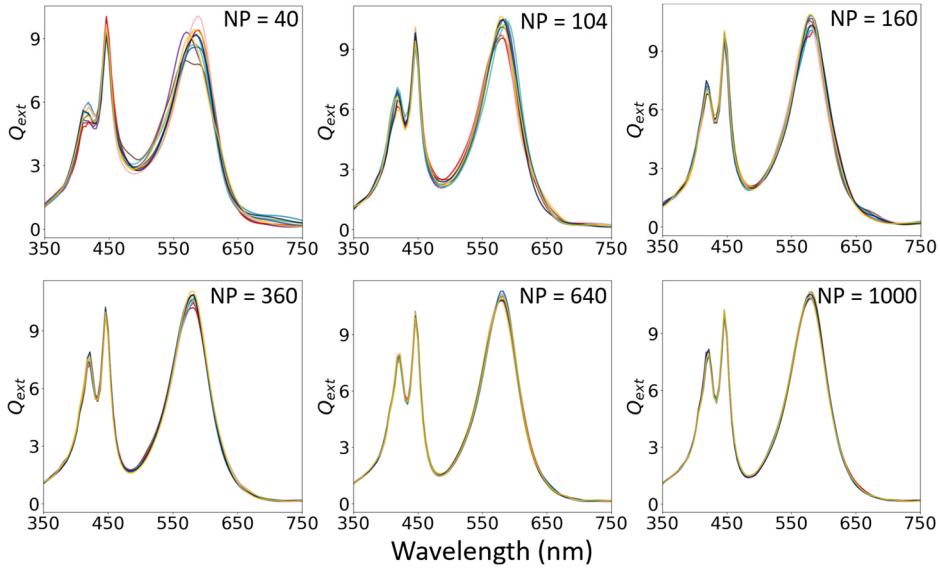

Figure 3.9. Spectral variation of ten simulations for arrays with increasing size from NP = 40 to NP = 1000 at x-disorder = 20%.

Turning to the question of whether the array size and spatial disorder of real-like sample in Figure 3.1d are precise enough to provide reliable optical response of the real sample, we first quantify the disorder degree of the real-like sample. As shown in Figure 3.10, by comparing the histogram and plane view of a generated array, the disorder level of real-like sample is determined as being ~20% along the x and y axes. In addition, the array size is equivalent to an array of 160 NPs, which corresponds to a relative average error of 7 %. In conclusion, the statistical optical properties of

real samples can be well-reproduced by a few micrometers wide real-like sample and the collective effects are still largely present in the laser-induced self-organized metasurfaces despite the intrinsic inhomogeneities. In the next section, we will investigate the underlying mechanisms of these collective behaviors using simulations from real-like sample, which only arise for TE polarization.

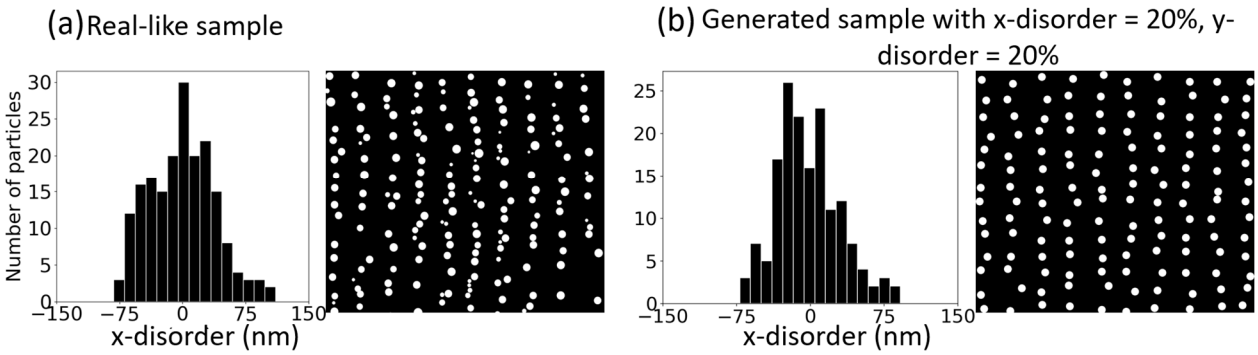

Figure 3.10. Histogram and nanoparticle array (a) for real-like sample and (b) for a generated sample with x-disorder = 20% and y-disorder = 20%.

3.4 Coupling between plasmonic and photonic modes

To undoubtedly highlight the optical mechanisms that occur at characteristic wavelengths, we compare further the optical properties of the real-like sample (Figure 3.11b.3) under TE polarization with the ones of the regular sample (Figure 3.11a.3). As already described in Figure 3.1, their extinction cross-section spectra (Figure 3.11a.1 and Figure 3.11b.1) exhibit a similar split of the dipolar plasmon mode, characterized by two peaks and a dip, which are identified by vertical dotted lines in Figure 3.11a.1 and Figure 3.11b.1. In addition, the regular sample shows the peak of the quadrupolar plasmon mode at 450 nm, which does not appear for the real-like sample since it is merged with the first blue-shifted peak of the dipolar contribution (Figure 3.4a). To confirm the quadrupolar nature of the peak at 450 nm, Figure 3.11a.6 and Figure 3.11a.10 display the near-field distribution in plane and cross-section views at this wavelength, which shows four symmetric maxima on the nanoparticle surface, including two maxima shown in cross-section (Figure 3.11a.6) and two maxima shown in plan view (Figure 3.11a10). On the regular sample, the dip at around 494 nm results from the interference between the incident wave and guided modes of the double layer structure excited through diffraction by the nanoparticle grating. This interference

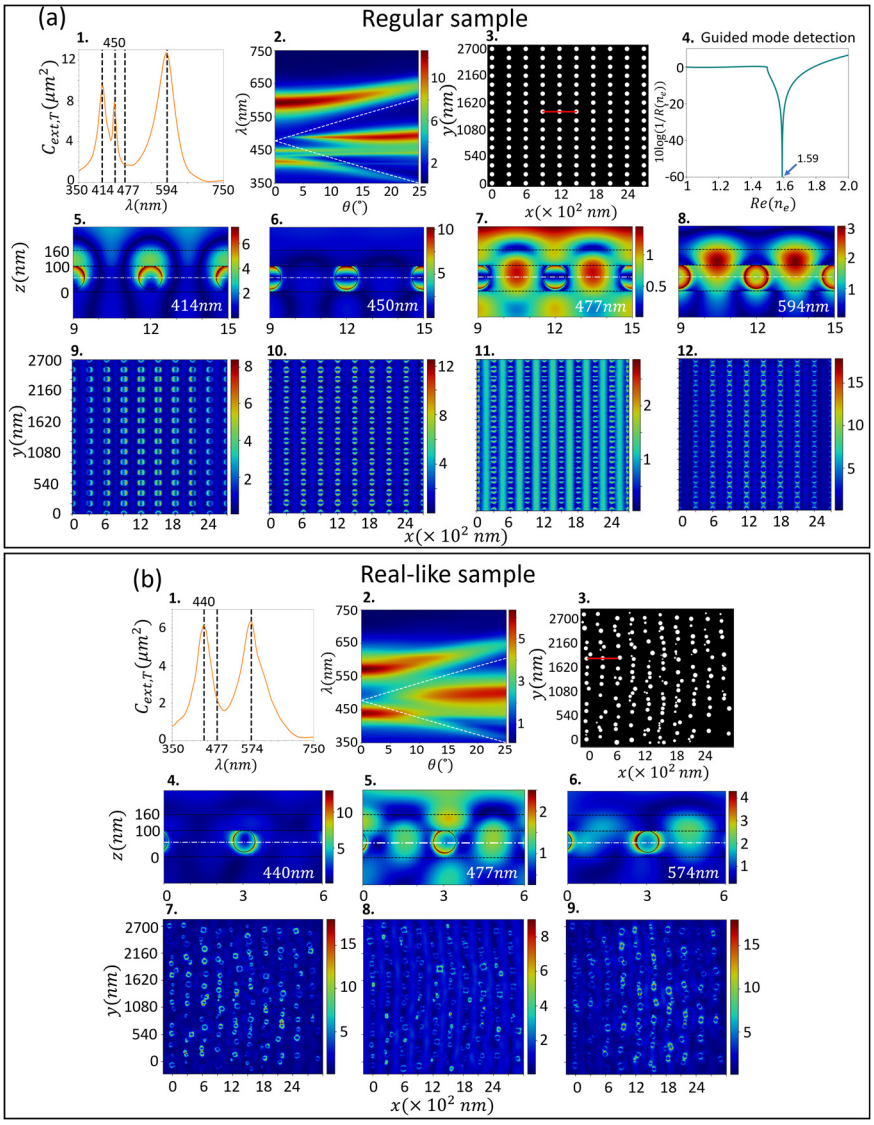

Figure 3.11. Spectral variations of $C_{ext,T}$ under normal incidence for (a.1) the regular and (b.1) real-like sample. The vertical dashed lines indicate the wavelengths at which the near field is calculated below. Spectral and angular maps of $C_{ext,T}$ for (a.2) the regular and (b.2) real-like sample. The white dashed lines indicate the guided modes excited by ±1 diffraction orders. Plane view of the (a.3) regular and (b.3) real-like NP arrays. (a.4) Pole of the reflection coefficient R of the two-layer system without nanoparticles. (a.5-12, b.4-9) cross section and plane view of the near field intensity distribution at selected wavelengths (shown in Fig. a.1 and b.1 respectively). The near-field intensities shown in plane view are calculated on the white dashed dotted lines drawn in the cross-section pictures. The near-field intensities shown in cross section are calculated on the red lines in Figure a.3 and b.3. The black dashed lines indicate the layer interfaces. All calculations are implemented for TE polarization.

creates a standing wave pattern, where nanoparticles reside at the nodes, i.e. the positions of minimum intensity (Figure 3.11a.7 & 11). Similar observations were already reported many times[89,91] and can be explained by the π phase shift of the scattered field at the nanoparticle surface compared to the incident wave.[123] Correspondingly, the field enhancement and absorption at the nanoparticle surface are almost null and the material is almost transparent at this wavelength. As demonstrated by Amra et al.,[158] (Section 7.2) the effective refractive index of guided modes that can propagate in a multilayer structure corresponds to the complex poles of the reflection coefficient of the structure. Figure 3.11 a.4 shows the reverse reflection coefficient of the two-layer structure as a function of the effective refractive index. As we know that the field is negligible on nanoparticles at the considered wavelength, we assume in this simulation that the intermediate layer is nanoparticle free. The results show that one guided mode can propagate in the structure, and lead to an effective index $n_e = 1.59$. Assuming that this guided mode is excited through the first diffraction order of the 300 nm period grating of nanoparticles, one can deduce the wavelength at which the excitation should occur: $\lambda = \Lambda * n_e = 300 * 1.59 = 477$ (nm). This value points out the beginning of the plateau where $C_{ext,T}$ is minimum on Figure 3.11a.1, and is then compatible with the rigorous calculation of the scattered field. Comparing now the near field distribution of the real-structure with the one of the regular sample at the position of the calculated guided mode (477 nm), the similarities are striking despite the heterogeneities of the real-like structure (Figure 3.11b.5& 8). One can thus conclude that the dip in the $C_{ext,T}$ spectrum of the real-like structure also results from the excitation of a guided mode in the structure, whose effective index is considered to be also equal to 1.59 in the following discussion.

Actually, two guided modes can propagate in the structure, one going to the right, the other to the left. Under normal incidence, the wavelength at which these two modes are excited is the same. But under oblique incidence, according to the grating equation (Equation 3.1), the left (or backward) and right (or forward) modes are excited by two different wavelengths $\lambda_{\pm}$.

$$\lambda_{\pm} = \Lambda \frac{n_e - n_i sin\theta_i}{\pm m} \tag{3.1}$$

where $\theta_i = 0°$ is the incident angle, n_i is the refractive index of the incident medium, $\pm m$ is the order of diffraction (± 1 in the present case), and Λ is grating period. Assuming that $n_e = 1.59$, $\lambda_\pm$ are plotted with white dashed lines in Figure 3.11a.2 and Figure 3.11b.2 that display the spectral and angular dispersion of the extinction cross-section in transmission for both samples. At small incidence angle, when the guided modes spectrally overlap with the dipolar mode of the LSPRs of individual nanoparticles, their interaction turns into a dip in the extinction. When the photonic modes move outward from this spectral area for larger angles, the white dotted lines get closer to the extinction peaks. In addition, the dipolar mode of individual nanoparticles starts to reinforce at around 494 nm. This behavior was also observed in other periodic structures, with two-dimensional gold nanoparticles[123] or one-dimensional gold grating[88] placed on top of an ITO waveguide. Here, we report this behavior for a structure with spatial disorder and size-inhomogeneity, namely the laser-induced self-organized structure (Figure 3.11b.2). The latter exhibits a very similar behavior with broader resonances due to the heterogeneous broadening. Interestingly, the quadrupolar mode of the LSPR emerges on the spectrum of the real-like structure when dipolar contribution is attenuated by its interaction with a guided mode, i.e. in the angular range [10°;12°]. The quadrupolar resonance mode does not contribute to the excitation of the guided modes and appears as a horizontal stripe insensitive to the incident angle. For TM polarization (Figure 3.12b1 and Figure 3.12b.2), the angular behavior of $C_{ext,T}$ features LSPRs whose resonance wavelength is almost independent of the incident angle.

The coupling between the photonic and plasmonic modes leads to the generation of hybridized states, which manifest themselves as extinction peaks, featuring the characteristics of both modes. For the peak at $\lambda = 414$ nm, the electric field is mainly enhanced and localized around the metallic particle with a small field enhancement on top of the particles, indicating the dominant of LSPRs (Figure 3.11a.5 and Figure 3.11a.9). On the other hand, in Figure 3.11a.8, the field distribution at 594 nm shows stronger feature of photonic nature, where not only does the field distribute around the metallic particles, but it also concentrates in the top layer between the nanoparticles. This is an indication of the coexistence of plasmonic and photonic modes, which can be referred to waveguide-plasmon polariton.[88,89,91] In addition, as shown in Figure 3.11a.12, the emergence of

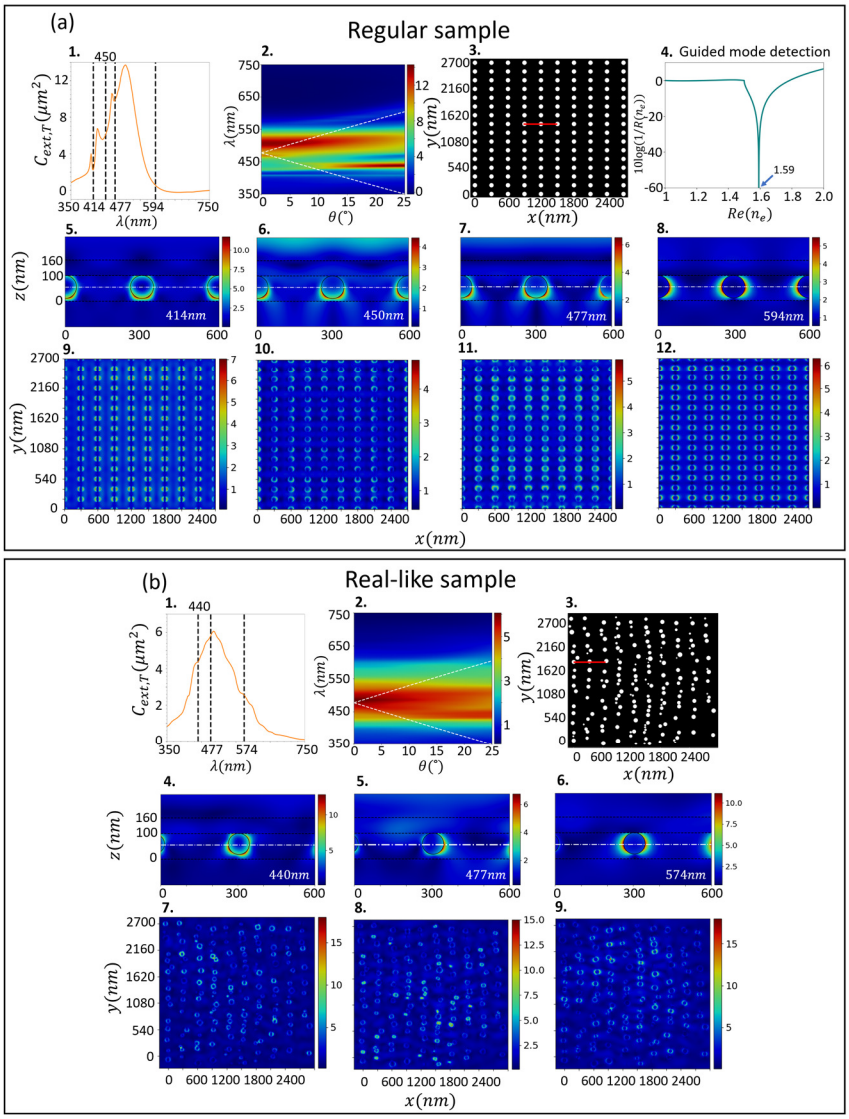

Figure 3.12. Spectral variations of $C_{ext,T}$ under normal incidence for (a.1) the regular and (b.1) real-like sample. The vertical dashed lines indicate the wavelengths at which the near field is calculated below. Spectral and angular maps of $C_{ext,T}$ for (a.2) the regular and (b.2) real-like sample. The white dashed lines indicate the guided modes excited by ±1 diffraction orders. Plane view of the (a.3) regular and (b.3) real-like NP arrays. (a.4) Pole of the reflection coefficient R of the two-layer system without nanoparticles. (a.5-12, b.4-9) cross section and plane view of the near field intensity distribution at selected wavelengths (shown in Fig. a.1 and b.1 respectively). The near-field intensities shown in plane view are calculated on the white dashed dotted lines drawn in the cross-section pictures. The near-field intensities shown in cross section are calculated on the red lines in Figure a.3 and b.3. The black dashed lines indicate the layer interfaces. All calculations are implemented for TM polarization.

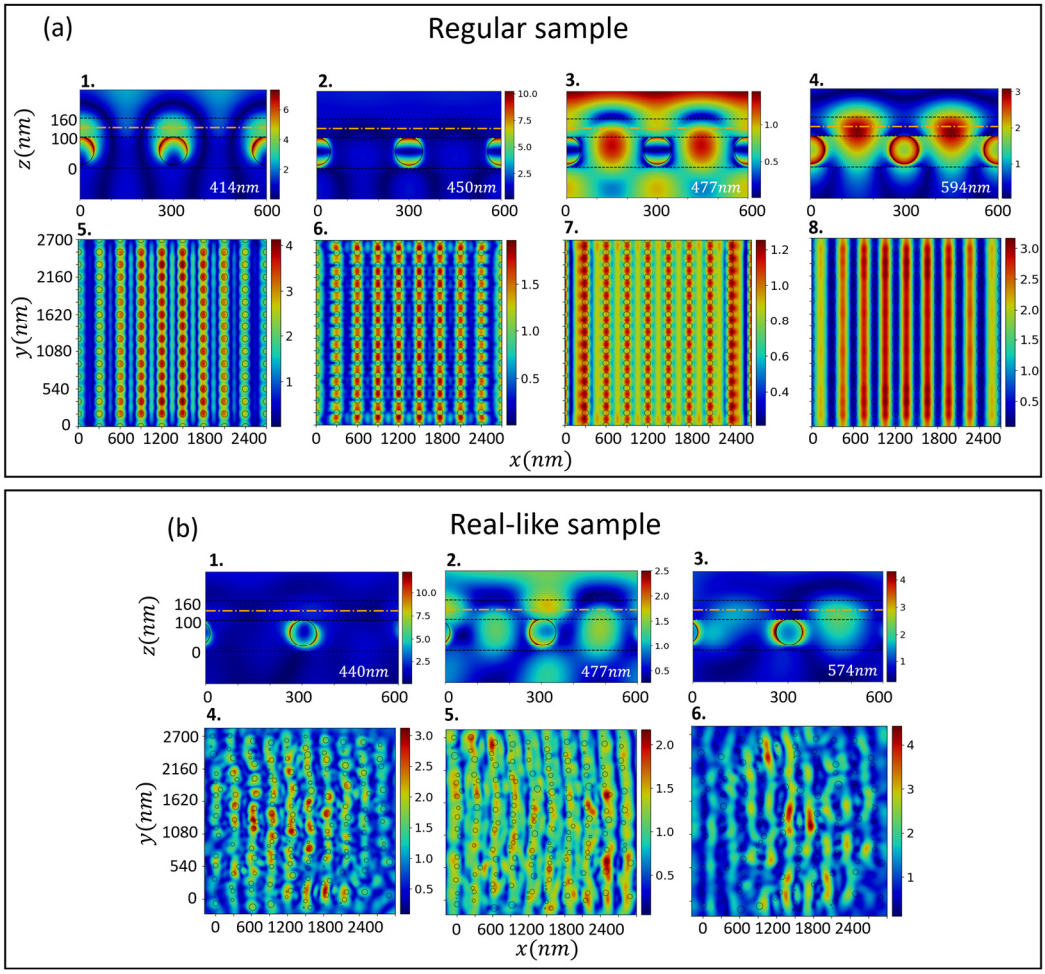

Figure 3.13. (a-b) Near-field intensity on cross-section and plane views (z = 130 nm) at the selected wavelengths, where the spectra exhibit extinction dips or peaks as shown in Figure 3.11, under normal incidence of the regular sample and real-like sample respectively. The orange dashed dotted lines in cross-section view indicate where the plane views are calculated. The black circles in plan views represent the NPs positions and sizes.

the hybrid state causes the electric field redistribution with enhancement between the nanoparticles, evidencing a strong coupling between particles. The comparison of the near field distribution at the two extinction peaks for the real-like sample (Figure 3.11b.4, Figure 3.11b.6, Figure 3.11b.7 and Figure 3.11b.9) show, as on the regular sample, a field located on the nanoparticles at the lower wavelength and located both on the nanoparticles and in the top layer at the higher wavelength. The spatial disorder and size dispersion significantly alter the field intensity

from one nanoparticle to another. However, the comparison with the regular structure confirms that mode hybridization takes place in the real-like structure. Additional near-field plane views calculated at the middle of the TiO_2 layer are given in Figure 3.13. The corresponding simulations of Figure 3.11 for TM polarization are shown in Figure 3.12, evidencing that only LSPRs in the whole wavelength range are observed.

Figure 3.14a-e further investigates the near field intensity distribution when the regular structure is illuminated by a plane wave under $\theta_i = 10°$. The dip at 477 nm under normal incidence, where the scattered field is π-out of phase with the incident wave on the nanoparticles, has been split in two dips, which can be determined using equation (3.1), at 425 nm and 529 nm (Figure 3.14a). The shorter wavelength corresponds to the forward mode, while the longer wavelength corresponds to the backward mode. When interfering with the incident light within the structure, the forward mode leads to an interference pattern that is tilted to the left on the cross-section view, as simulated in Figure 3.14c (cross-section) and as can be deduced from the wave vectors direction of the two interfering waves. As the simulated structure is finite and illuminated with a plane wave, the excitation of the forward mode also leads to an accumulation of light intensity to the right (plan views at z = 55 nm and z = 130 nm in Figure 3.14c). It should be noticed that the quadrupolar mode occurring at 440 nm, which does not excite the guided mode itself, partly overlaps with the interference pattern associated to the forward mode at 425 nm wavelength (Figure 3.14c). At shorter wavelength, the hybridized mode features an extinction peak at 398 nm where the field enhancement at the particles top surface and the field accumulation at the right of the plane views can be observed (Figure 3.14b). The backward mode excited at 529 nm leads to an interference pattern tilted to the right on the cross-section views and to an accumulation of light to the left on the plane views at z = 55 nm and z = 130 nm (Figure 3.14d). The resulting hybridized mode occurs at 602 nm (Figure 3.14e) and leads to an enhanced absorption of the dipolar plasmon mode and a field enhancement in the upper layer that accumulates to the left. While less regular, these features are also observed on the real-like structure whose simulations are gathered in Figure 3.14g-j. Consequently, the size dispersion and spatial disorder of nanoparticles resulting from laser processing do not significantly prevent the occurrence of the hybridized states between plasmonic and photonic modes for TE polarization.

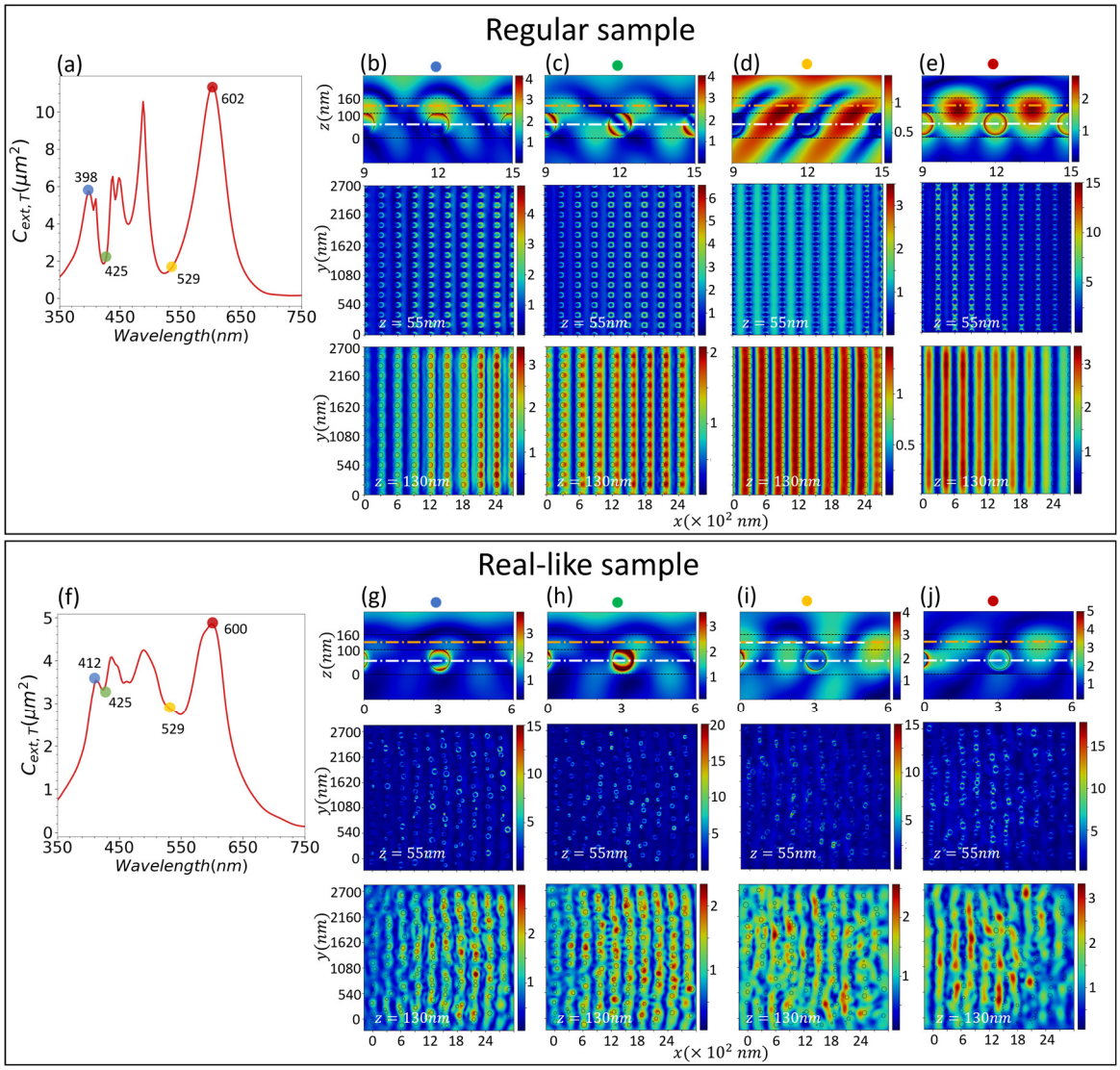

Figure 3.14. Optical properties of the regular and real-like structures under an oblique incidence angle of 10°. (a, f) Extinction cross-section spectrum of both structures. (b-e, g-j) Near field intensity on the cross-sections and plane views at characteristic wavelengths. The forward (green dot) and backward (yellow dot) guided modes excited π-out-of-phase with the incident wave at the nanoparticle surface show light that propagates and accumulates to the right and left, respectively. The blue and red dots correspond to the hybridization of the forward and backward mode, respectively, with the dipolar plasmon mode of individual nanoparticles. The cross-sections are calculated at the same position as the one shown in Figure 3 (red line). The white (z = 55 nm) and orange (z = 130 nm) dashed dotted lines indicate where the near fields on the plane view are calculated. The black dashed lines represent the layer interfaces. Black circles in plane views (z = 130 nm) represent the positions and sizes of NPs.

This laser technique not only produces metamaterials that sustain hybrid modes but it can also control the coupling strength through the spectral overlapping between the resonance modes and diffraction efficiency of the nanoparticle grating. The spectral overlapping can be changed by varying the grating period of the self-organized nanoparticle array. As explained in our previous article[47] this grating period is proportional to the incident laser wavelength used for processing. The laser wavelength and other parameters as the laser power or scan speed can also affect the average nanoparticle size and their size dispersion, and in turn the diffraction efficiency of the nanoparticle array. Figure 3.15 shows the results related to another real sample, which was produced at λ = 647 nm, with a power of 500 mW and a scan speed of 300 μm/s, and the corresponding simulations of the realistic structure. The longer laser processing wavelength leads to a larger average grating period of 400 nm (Figure 3.15a). Assuming the thicknesses shown in Figure 3.15d, deduced from SEM picture of the sample cross section (Figure 3.16), the same refractive indices as previously and a film free of nanoparticles, one can use the same approach as previously to determine the occurrence of one guided mode in the structure with an effective index of 1.56 (Figure 3.15b). Multiplying this value by the average grating period, one can find that under normal incidence, the guided mode can be excited at 624 nm, which matches well the position of the blue-edge of the second dip in transmission in Figure 3.15c and Figure 3.15f, and the near-field distribution shows interference patterns with low excitation on particle surface (Figure 3.15h). As the experimental size distribution (shown in fig. 3.16b) shows smaller sizes than in the first sample, the dipolar mode of the LSPRs (first peak in Figure 3.15c) is blue-shifted compared to the first sample, resulting in strong electric field enhancement at 482 nm confined around nanoparticles, as shown in Figure 3.15g. Conversely, the hybrid mode excited at higher wavelength (658 nm) with the electric field is delocalized and mainly distributed around surrounding media. Consequently, the resonance of the plasmonic and photonic modes do not spectrally overlap, which results in weak coupling effect. Notice that in this weak coupling regime, the excited guided mode is tuned out of the LSPRs, appearing closer to the extinction peak. Therefore, it features similar near-field pattern to the peak (Figure 3.15h & i). Simulating the spectral and angular variations of the extinction cross-section in transmission (Figure 3.15e), shows that the spectral overlapping occurs for incidence angles above 15°. Then, the coupling between the photonic and plasmonic modes leads to a reduced absorption followed, at longer

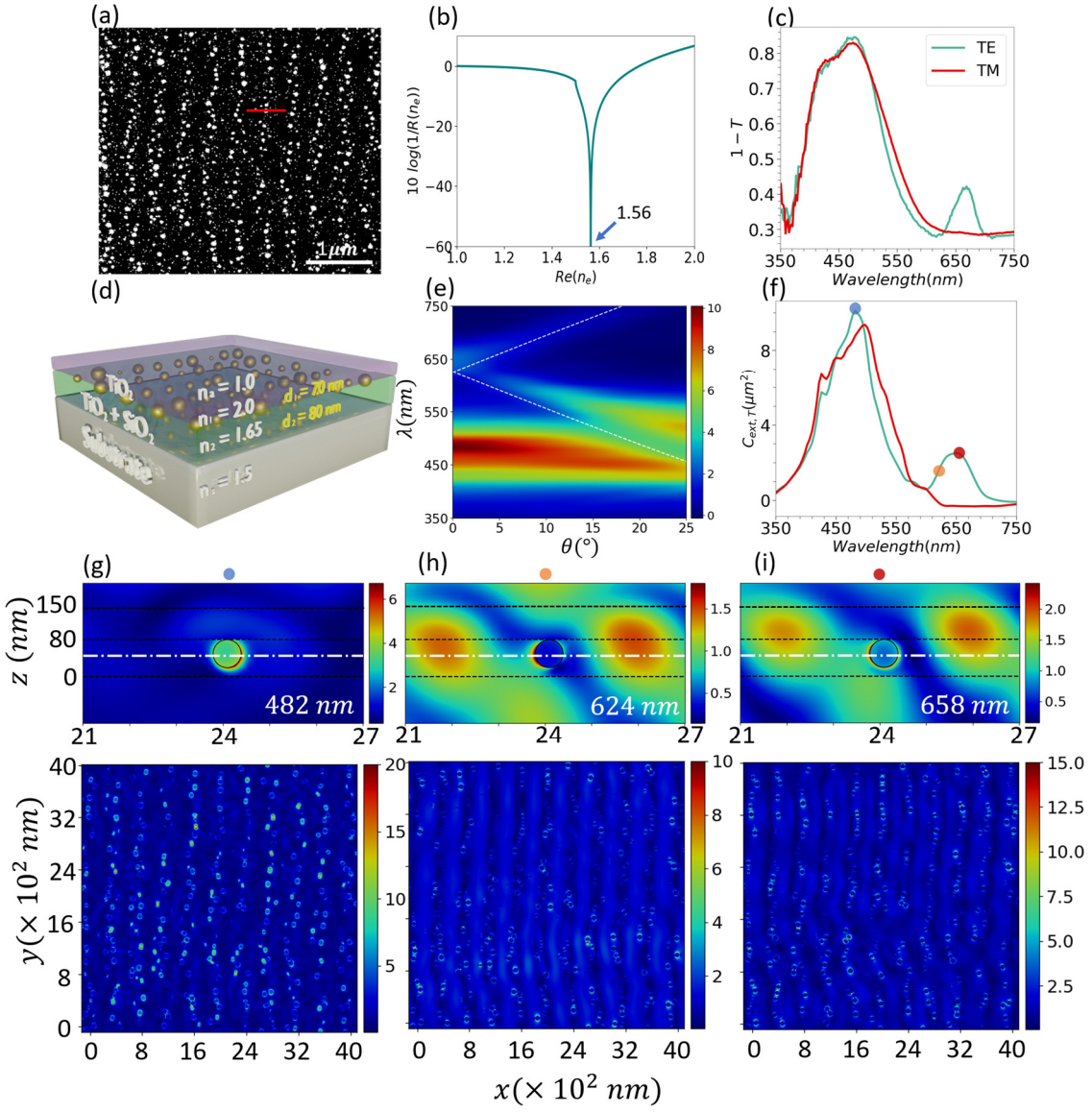

Figure 3.15. (a) Plane view of the real-like sample simulated from a real sample laser processed at λ=647 nm, with power of 500 mW and scan speed of 300 μm/s. (b) Reverse reflection coefficient R of the two-layered system without nanoparticles in logarithmic scale. 1.56 is the effective index value of the guided mode considered to draw the dash lines in (e). (c, f) Extinction spectra of the true and simulated sample. (d) 3D sketch of the simulated structure. (e) Spectral variations of the extinction cross-section in transmission of the real-like sample. (g-i) near field intensity on the cross-sections and plane views at the characteristic wavelengths.

wavelength, by an absorption enhancement. The inhomogeneity of this other laser-induced quasi-random plasmonic metasurface does not prevent the excitation of guided modes and the occurrence of hybridization. These examples, selected among a large database of laser-processed samples produced by tuning the laser wavelength, power, scan speed and laser focus, are two extreme cases where dichroic properties are observed. They should be representative of a large number of laser-processed samples in which self-organized periodic patterns occur.

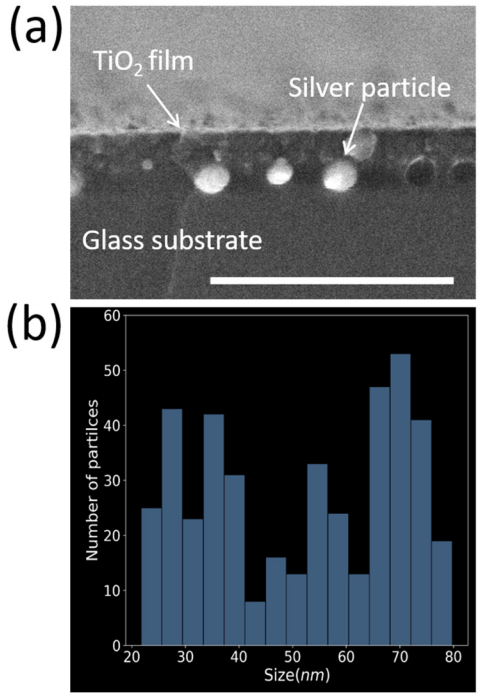

Figure 3.16. (a) Cross-section view and (b) size distribution of the sample processed by laser at 647 nm, 500 mW and 300 μm/s. The scale bar is 500 nm

3.5 Conclusions

In conclusion, this study investigates the effect of intrinsic spatial disorder and size dispersion that exist in the laser-induced self-organized plasmonic metasurfaces on their optical properties. Simulations are carried out on regular structures in which different array sizes, levels of disorder and different size distributions are introduced, and on realistic structures elaborated from three

dimensional reconstructions of real samples. By proving the adequacy of the real-like sample in reproducing the statistical properties of experimental sample and further investigating the near-field distribution, we characterize the coupling between the dipolar mode of the LSPR of individual metallic nanoparticles and guided modes excited through diffraction by the nanoparticle array. The near and far field investigations demonstrate that the inhomogeneities inherent to the fabrication technique, while striking when looking at the structures at the nanoscale, do not disturb so much the overall interaction with light. Two representative kinds of laser-induced nanostructures, exhibiting different periods, size distributions and dichroism, confirm this conclusion. Laser processing appears then as a powerful technology to produce useful functional metamaterials despite intrinsic imperfections. With its simplicity, cost-effectiveness and scalability, it is very promising for industrial applications, which exploit the fascinating optical properties of plasmonic materials.

4 Controlling color, diffraction and dichroism of plasmonic metasurfaces

Structural and plasmonic colors have attracted growing interest over the last fifteen years for their stability, environmentally friendly properties, singular visual effects and their numerous potential applications. However, scalability remains a major challenge when considering their flexible use over large surfaces. Laser processing has then appeared as a good candidate to overcome this challenge thanks to its versatility, efficiency, cost-effectiveness and simplicity. However, the quasi-random nature of the nanoparticle distributions produced by laser made the understanding of their optical properties tricky and the confidence in their reproducibility limited. In this chapter, we demonstrate the potential of nanosecond lasers to control the diffraction, dichroism and colors of random plasmonic metasurfaces while explaining the origin of their optical properties through electromagnetic simulations. The optical properties are first linked to the geometrical parameters of self-organized gratings that are induced by laser either on the surface by a topographic modulation or below the surface by the growth of organized nanoparticles. These two kinds of gratings are perpendicular to each other and exhibit different periods. The chapter unravels the main mechanisms that shape the spectral properties of these laser-induced nanoparticle gratings. Electromagnetic simulations evidence the role of plasmonic surface lattice resonances resulting from the far field coupling of metallic nanoparticles despite their size dispersion and relative disorder. They also demonstrate the impact of near field coupling that leads to the hybridization of plasmonic modes of some particle pairs closely packed along the grating lines in these laser-induced structures. The chapter shows how the two kinds of self-organized gratings influence the diffraction and dichroism. Imperfections of laser-induced metasurfaces bring singular properties that do not exist in perfectly regular samples. They are used here to print faithful color images in different modes of observation and to use diffraction or dichroism as a security feature.

4.1 Introduction

Structural color printing has recently emerged as an eco-friendly technique to generate vivid colors and interesting visual effects stable over time.[2,4,10] While traditional inks are based on dye absorption, structural color marking technologies create colors originating from various optical phenomena including scattering,[27,28] absorption,[29,159] diffraction,[160] interference,[161] or coupling between resonance modes.[162,163] This gives the technologies huge advantages and extra freedom to design optical devices, and develop real-life applications spanning from data storage,[11] information security,[164,165] color filters,[166] sensors,[167] to display technologies.[8]

Various approaches have been proposed to produce metamaterials with structural colors, such as electron beam lithography,[21,168] focused ion beam,[159] or chemical methods.[169] Among them, laser-based technologies emerge as foremost industrial processes owing to the fact that they are versatile, rapid, cost-effective and scalable.[40,170] Laser can trigger several mechanisms that modify the physical properties of metamaterials, and so their colors. Metallic particles can thus be resized, reshaped and organized. The spectral shape of their localized surface plasmon resonances can be tuned by changing their geometrical parameters.[42–44,56,171,172] When the laser triggers their self-organization, diffraction grating whose period and orientation depend on the laser wavelength and polarization can emerge and be used to diffract visible light [45,48] or induce dichroism.[52,53] These diffractive and dichroic properties have recently been used to implement laser-induced image multiplexing where three images were encoded and printed in a single metasurface.[37,38] The dichroic colors that were used for some multiplexed images were shown result from the coupling between the localized surface plasmon resonance of individual metallic particles and delocalized photonic modes excited through the self-organized nanoparticle grating.[38] In all these studies, the laser modifies simultaneously several parameters of metallic nanoparticles including their size, density and organization, and does control the statistical distribution of these parameters over large ensembles of nanoparticles rather than their specific value for each single particle. The laser can also change different parameters of the film that supports or contains the nanoparticles, such as its crystal phase, density, thickness or surface topography. Fabry-Pérot interferences can then contribute to the final optical properties of the system.[41,173] The variety of optical mechanisms involved in random plasmonic metasurfaces makes them powerful to create particular color

properties such as the ones that recently enabled three-image multiplexing. The simplicity and flexibility of laser processing make it appealing for developing large-scale applications. And, the quasi-random nature of the nanoparticle assemblies creates an interesting challenge to unravel the different mechanisms that shape the color properties of these materials.

In this chapter, we unravel the mechanisms that control the optical properties of quasi-random plasmonic metasurfaces produced by laser processing. We especially pay attention to nanosecond (ns) laser-processed Ag NPs:TiO_2 metasurfaces that exhibit diffractive and dichroic properties, to explain why these two phenomena can be observed simultaneously or independently. Optical characterizations highlight the laser parameter ranges where the different optical behaviors occur and allow identifying rapidly the main kinds of metasurfaces that can be produced by laser processing. Their morphological properties are measured by electron microscopy and atomic force microscopy. Two main features, a periodic arrangement of metallic nanoparticles and a periodic modulation of the surface topography characterize the diffractive or dichroic metasurfaces. The chapter explains the relative importance of the different self-organized periodic structures on the optical properties of metasurfaces. Electromagnetic simulations of real-like samples unveil the role of coherent far-field coupling by the nanoparticle grating and of near-field coupling, on the diffractive and dichroic properties. They allow to explore separately the influence of different parameters by considering both the real-like structures and close perfectly periodic structures. The chapter finally demonstrates that the technology can be used to mark faithful color images in different modes of observation. The colors observed in other modes can then be used for security purpose.

4.2 Overview of the optical and structural properties of the laser induced random plasmonic metasurfaces

Mesoporous titania thin films loaded with silver and deposited on glass substrate are processed with a slightly focused ns laser (532 nm) scanning the surface to create quasi-random plasmonic metasurfaces (Figure 4.1a). Their properties are controlled at the scale of a pixel size by varying four parameters. Figures 4.1b and 4.1c give a sampling of colors exhibited by these metasurfaces

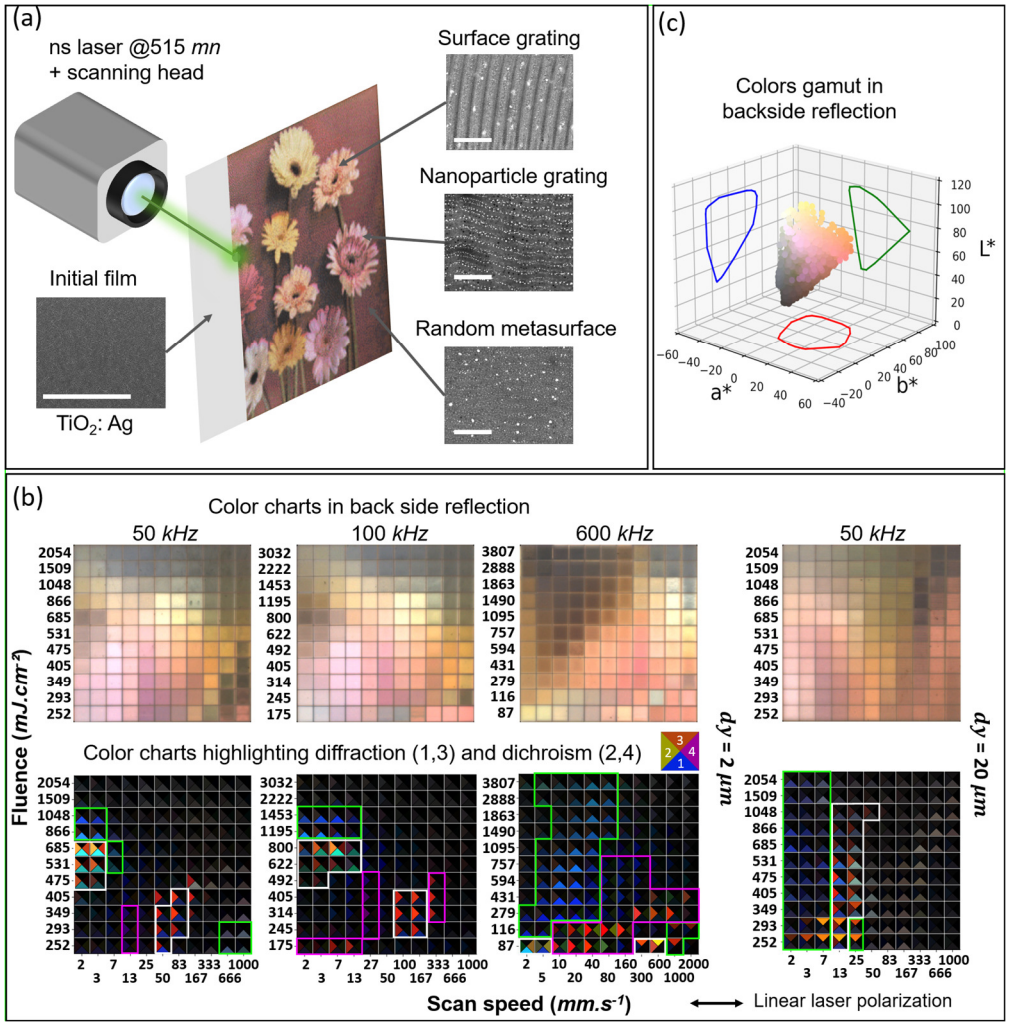

Fig. 4.1. Optical properties of laser-induced metasurfaces. (a) Principle of the laser marking process. A few scanning electron microscopy images illustrate different kinds of laser-induced metasurfaces that exhibit different colors. (b) Charts illustrating some optical properties of metasurfaces generated by varying four laser processing parameters: the laser fluence and repetition rate, the scan speed of the laser beam and the distance dy between consecutive laser lines. The laser polarization is fixed and parallel to the double arrow. The top charts show the colors observed in backside reflection (specular reflecion). All measurements were carried out under white light illumination. The bottom charts show four data per square. Triangles #1 and #3 show the color observed in two diffraction configurations where the plane of incidence is either perpendicular (triangle #1) or parallel (triangle #3) to the laser polarization. Triangles #2 and #4 illustrate the dichroism in reflection and transmission, respectively, where the displayed color corresponds to the color difference (ΔR, ΔG, ΔB) between the colors measured with a TE or TM linearly polarized incident white light. The setup used for measuring the colors is described in Section 2.3. (c) Gamut in the CIE L*a*b* color space of colors measured in the backside reflection mode (details are given in Section 2.3). The convex hull of the gamut is projected on the three planes for more clarity.

in specular reflection when observed from the backside. We will come back on the printing of faithful color images in various modes of observation at the end of the chapter. Figure 4.1b also highlights diffractive and dichroic behaviors of metasurfaces.

The diffractive behaviors (triangles #1 and #3) highlight the presence of two main kinds of diffraction gratings that result from laser-induced self-organization processes. The origin of these two perpendicular self-organized periodic patterns is already discussed in the previous studies.[52,53] The first type of self-organized grating, which appears when triangles #1 lit in blue (Figure 4.1b, bottom color charts), corresponds to gratings parallel to the incident laser polarization with a period in the range 290 – 380 nm. When the blue color shifts toward green in triangle #1, the grating period increases, as can be deduced from the grating equation and the fixed parameters of the measurement setup (Section 2.3). The second type, which appears when triangles #3 lit in orange, corresponds to gratings perpendicular to the laser polarization with a period in the range 460 – 500 nm. When the orange color shifts toward yellow in triangle #3, the grating period increases. Some triangles #1 appear whitish or brownish rather than blue, they correspond to metasurfaces that scatter light in a broad range of observation angles rather than diffracting it, so to more disordered metasurfaces.

Triangles #2 and #4, in Figure 1b, characterize the sample dichroism that is shown by a color corresponding to the (ΔR, ΔG, ΔB) difference between the colors measured with TE or TM polarized white light. The color charts on the bottom side show that many metasurfaces previously identified as diffractive are also dichroic (squares inside the white outline), many others are only dichroic and not diffractive (pink outline) and still a large part is diffractive without exhibiting any significant dichroism (green outline).

4.3 Structural parameters of metasurfaces

Grating #3 only occurs at high speed and low fluence at 600 kHz repetition rate and corresponds to a periodic modulation of the surface topography with small disordered nanoparticles (Figure 4.2 – 300 mm.s^{-1}). While, interestingly, grating #1 can take many different forms. It corresponds to periodic modulation of the surface topography with disordered nanoparticles in Figure 4.3 (685

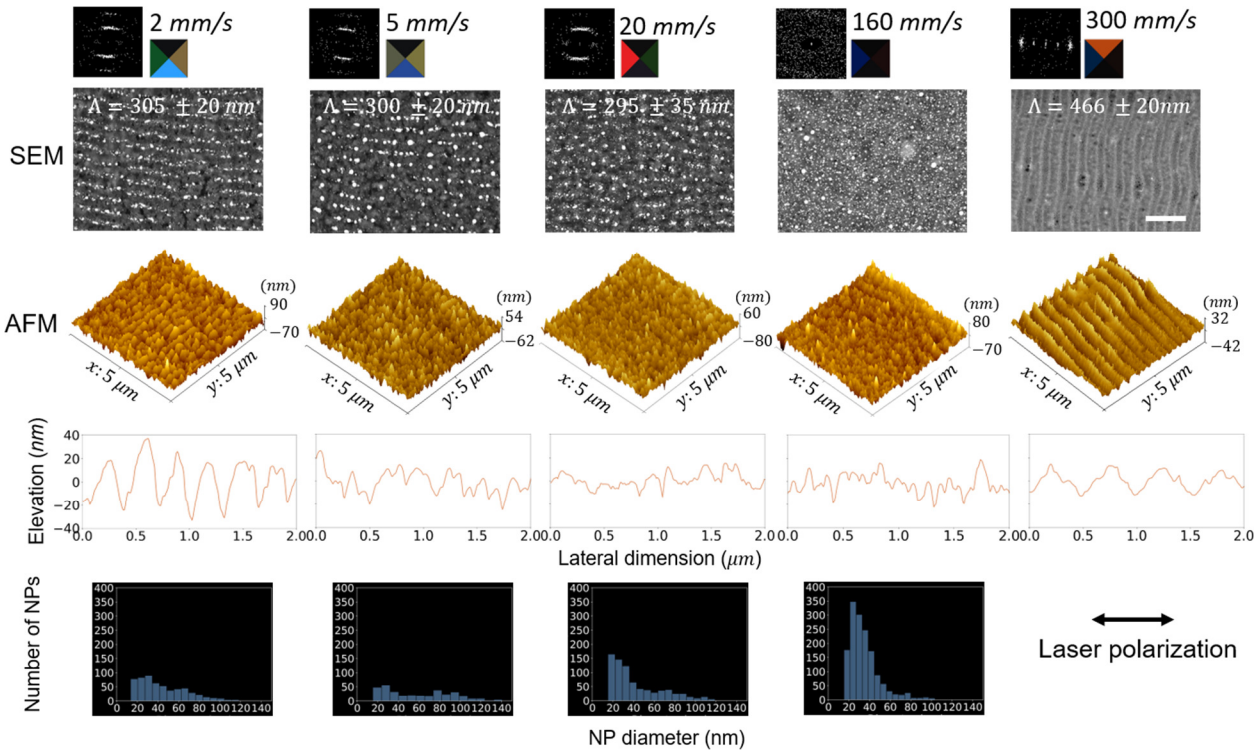

Fig. 4.2. (a) Evolution of the physical and optical properties of laser-induced metasurfaces when varying the scan speed (from 2 mm.s^{-1} to 300 mm.s^{-1}) at low fluence (87 mJ.cm^{-2}), high repetition rate (600 kHz) and large overlapping between laser lines (dy = 2 µm). For each scan speed, the sample is characterized by a four-color chart (as described in Figure 4.1), a representative scanning electron microscopy (SEM) image with the value of the grating period and its Fourier transform on the top corner left, an atomic force microscopy (AFM) 3D view of the surface topography and the corresponding surface profile, measured along the x axis for the 4 left images and along the y axis for the sample at 300 mm.s^{-1}, and a histogram of the nanoparticle sizes as observed by SEM. The double arrow indicates laser polarization for the SEM images. The scale bar is 1 µm in all SEM images.

mJ.cm^{-2}, 2 mm. s^{-1}, 50 kHz). It may correspond to self-organized particles mainly located in the film, with additional surface corrugation (Figure 4.2 – 2 mm.s^{-1}, 87 mJ.cm^{-2}, 600 kHz), or without surface corrugation (Figure 4.2 – 5 mm.s^{-1}, 87 mJ.cm^{-2}, 600 kHz). It exhibits self-organized particles that emerge on the top surface in Figure 4.4.

In order to highlight the most important structural features that influence the metasurface optical properties, we choose to display the evolution of the surface topography and metallic nanoparticles

with the scan speed for metasurfaces generated at low fluence (87 mJ.cm^{-2}), high repetition rate (600 kHz) and strong overlapping between laser lines (dy = 2 µm). As illustrated in Figure 4.2, at low speed these metasurfaces exhibit diffraction with grating parallel to the laser polarization (#1), and dichroism (#2 & #4). Then, when speed increases, only dichroism is observed, before disappearing. At the highest speed, diffraction by a grating perpendicular to the

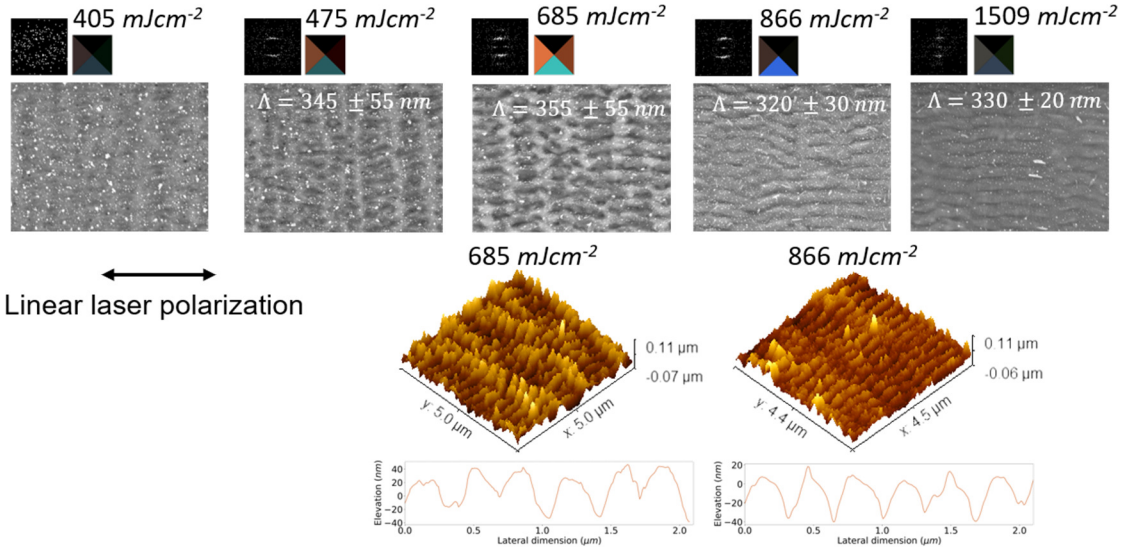

Fig. 4.3. Evolution of morphological profiles and optical responses of laser-induced metasurface when varying laser power at 50 kHz repetition rate, 2 mm/s scan speed and 2 µm laser lines distance. The scale bar is 1 µm.

laser polarization (#3) occurs. The combination of scanning electron microscopy (SEM) and atomic force microscopy (AFM) images gives insight about the main features that characterize the metasurfaces, namely their surface topography and the distribution of metal nanoparticles. At 300 mm.s^{-1}, the self-organized gratings perpendicular to the laser polarization (#3) are surface gratings whose period is slightly lower than the laser wavelength, in which Ag nanoparticles are small enough not to be clearly observed by SEM. When decreasing the scan speed (160 mm.s^{-1}), i.e. increasing the deposited energy per unit area, the surface topography homogenizes, the grating disappears, and Ag nanoparticles grow within a correlated disorder (homogeneous distances between nanoparticles). From 20 to 5 mm.s^{-1}, nanoparticles tend to organize along grating lines parallel to the laser polarization while growing up to reach sizes that exceed 100 nm. At the lowest speed, Ag nanoparticle gratings are associated with a surface grating that follows the nanoparticle

lines (same orientation, same period). The period of the nanoparticle gratings is a fraction of the laser wavelength, the divider being expected to be the effective refractive index of the photonic mode that can propagate within the layer.[52,53]

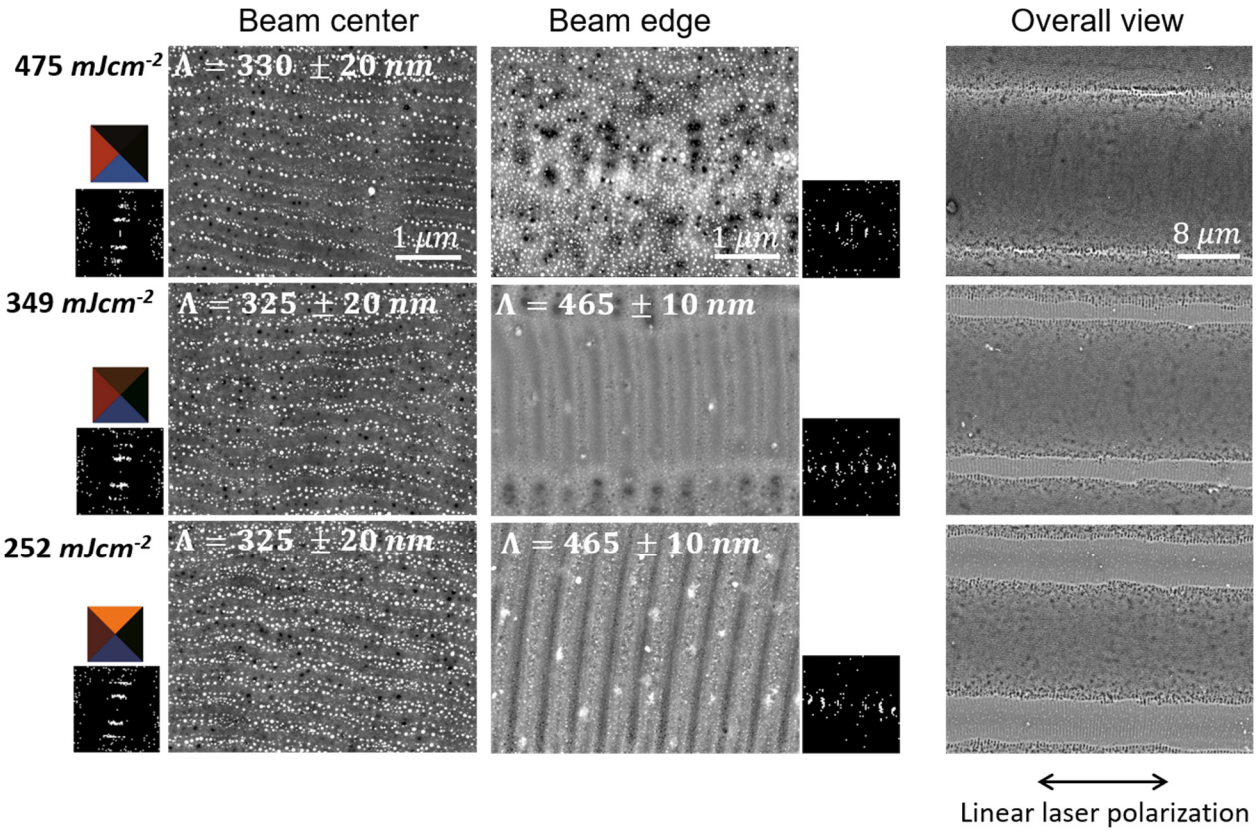

Fig. 4.4. Evolution of morphological profiles of laser-induced metasurface when varying laser power at 50 kHz repetition rate, 13 mm/s scan speed and 20 µm laser lines distance. The SEM images of the overall view with low magnification, center and outer of laser beam are given. The inset images are the Fourier transform of the corresponding images.

These results highlight the fact that diffraction is much stronger when a surface grating is present, whatever its period and orientation. However, the nanoparticle grating, while weakened by heterogeneity in the nanoparticle spatial arrangement and broad size distributions, may contribute to diffraction too by coherent far field coupling. Conversely, the dichroism seems mainly related to the presence of self-organized nanoparticle gratings and not to the surface grating. It is expected to originate mainly from two mechanisms: the near field coupling between nanoparticles aligned along the same line, and the far field coupling between the localized surface plasmon mode through

the excitation of a delocalized photonic mode propagating in the direction perpendicular to the grating lines. In the next sub-section, electromagnetic simulations intend to unveil the mechanisms at stake in the optical response of laser-induced quasi-random plasmonic metasurfaces. They will deal with realistic samples and regular samples (periodic structures with single nanoparticle size), and will investigate the influence of the structural parameters of the laser-induced nanoparticle gratings on the diffractive and dichroic properties of metasurfaces.

4.4 Origin of dichroism

In order to unveil the optical mechanisms at the origin of dichroism in the laser-induced metasurfaces, we propose to simulate the electromagnetic far field response of a realistic sample that mimics a dichroic experimental sample, as well as its closest regular sample (periodic and single nanoparticle size), which exhibits similar spectral features. Investigating the near-field of the regular sample will demonstrate the origin of collective resonances and serve as a guide to find similar resonances in the realistic sample. Some features that are specific to the realistic samples will finally appear to strongly contribute to the dichroism too.

Figures 4.5a and 4.5d show the SEM plan-view and TEM cross-section images of a dichroic sample (triangles #2 and #4 lit) obtained at 600 kHz, 116 $mJ.cm^{-2}$, 80 $mm.s^{-1}$, dy = 2 µm. A tridimensional representation of this sample is elaborated by considering spherical nanoparticles with the same diameter and in-plane distribution as the those measured by SEM, and in-depth location compatible with the simulation constraint imposing that nanoparticles must be located within a single medium. In the simulation, all nanoparticles are tangent to the top interface inside the 95 nm thick TiO_2 layer (Figure 4.5b-c) to mimic the STEM characterization as shown in Figure 4.5d. As the initial mesoporous TiO_2 layer (initial film thickness of ~200 nm as described in Section 2.1) has been largely densified by laser processing (95 nm thick layer) and the initial amorphous TiO_2 has been crystallized into its anatase phase (Raman characterization in Figure 4.6), the refractive index of the film surrounding the nanoparticles is set to 2; while the glass substrate has a refractive index of 1.5. Further details about the refractive index of Ag nanoparticles are given in Section 7.3. To reduce numerical errors due to the limited sample size (and number

of nanoparticles), the simulated sample is extended by duplicating four times the same structure (Section 7.4).

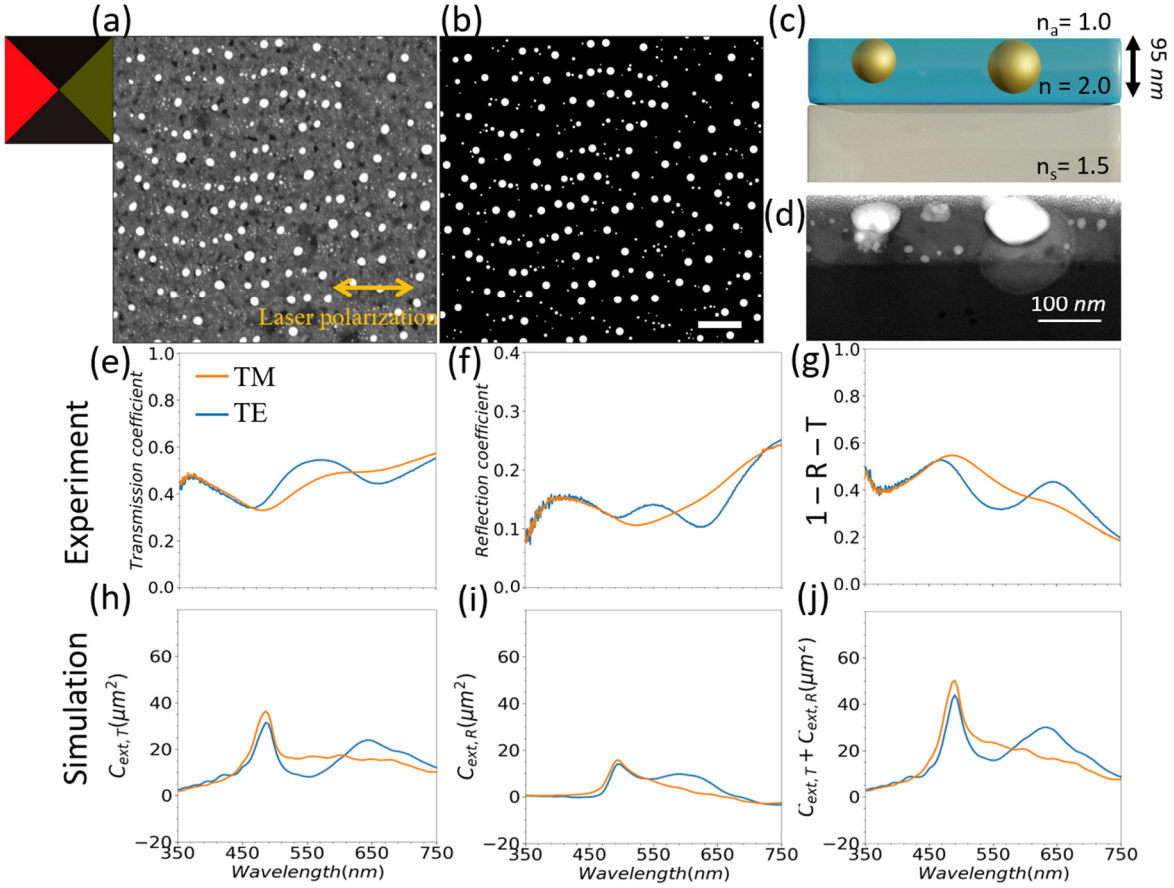

Fig. 4.5. Experimental sample vs realistic simulated sample. (a) SEM image of the considered nanostructure induced by laser processing at 600 kHz, 116 mJ.cm^{-2}, 80 mm.s^{-1} and dy = 2 µm. (b) Plan view and (c) cross-section of the simulated sample. (d) TEM cross-section of the experimental sample. (e-f) Experimental data of transmission (T) and reflection coefficient (R), and (g) the corresponding loss spectrum (1 – T – R). (g-j) Simulation results of extinction cross-section in transmission ($C_{ext,T}$), in reflection ($C_{ext,R}$) and total extinction ($C_{ext,T} + C_{ext,R}$), respectively. Scale bars in SEM is 500 nm. The incident field illuminates from the bottom at an incidence angle θ = 6° with a vertical incidence plane. The nanoparticle grating lines are parallel to the linear polarization of the laser used for processing the sample (horizontal double arrow in a). TE polarization is horizontal and TM polarization vertical in a-b.

The simulated extinction cross-section spectra in transmission and reflection (Figure 4.5h-i), which account for losses in the two specular directions, can be compared qualitatively with the

transmission (T) and reflection (R) coefficients (actually with 1-T and 1-R) measured on the real sample (Figure 4.5e-f), for two linear polarizations that are parallel (TE) or perpendicular (TM) to the nanoparticle grating lines (themselves parallel to the laser polarization used during laser processing). The total experimental losses (Figure 3g) can also be compared with the total simulated losses (Figure 4.5j). In both cases, the losses exhibit a single broad peak for TM polarization and two peaks for TE polarization.

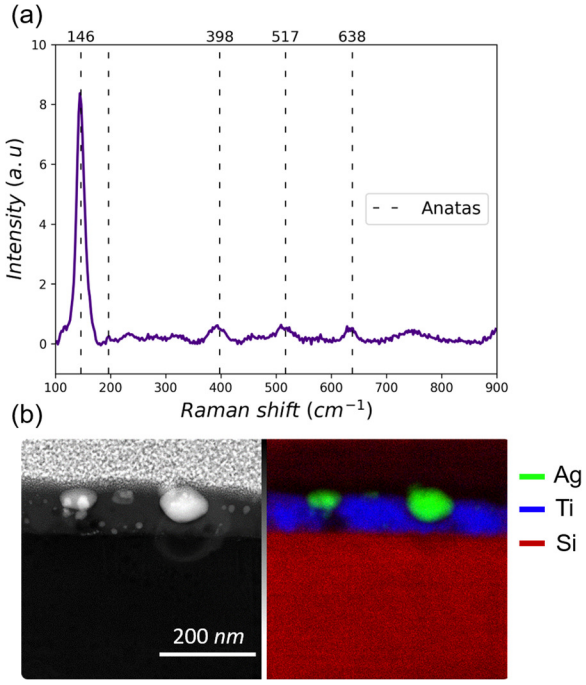

Fig. 4.6. Characterization of sample induced by laser at 600 kHz repetition rate, 116 mmJ.cm^{-2} laser fluence, 160 mm.s^{-1} scan speed and 2 µm laser lines distance. (a) Raman analysis. (b) Annular dark field (ADF) image (left image) and energy dispersive spectroscopy (EDS) chemical mapping (right image)

In Figure 4.7, we compare the far-field spectra and near-field intensity distribution of the realistic sample with those of a regular sample in which all nanoparticles are 71 nm in diameter and periodically spaced with 300 nm period along the x direction and 180 nm period along the y direction (Figure 4.7a.1). This regular sample exhibits narrower resonances and homogeneous near-field maps that make interpretation easier (Figure 4.7a.2). If the period along the x direction is similar to the average period that can be measured between lines of the realistic sample, the periodicity along the y direction is a stronger simplification since it does not exist in the realistic

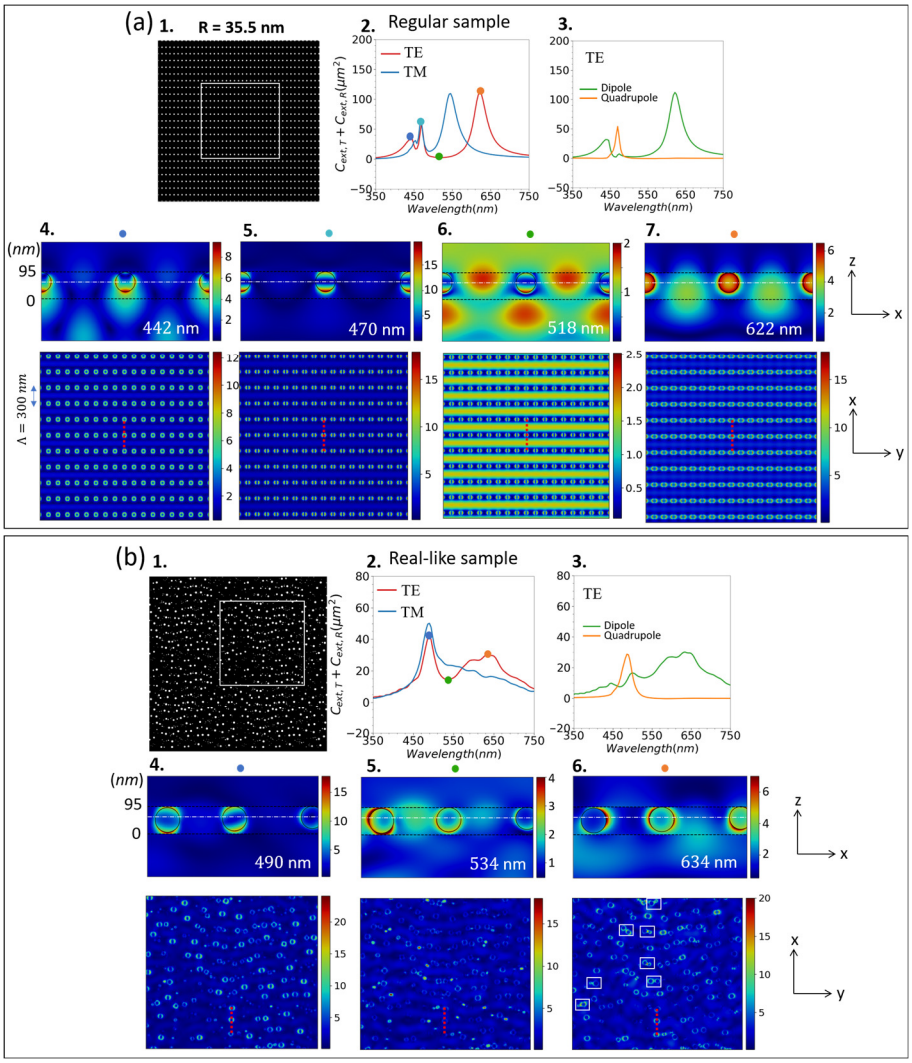

Fig. 4.7. Near-field maps in xz and xy plane of the regular and real-like samples for TE polarization (along the grating lines with $\Lambda = 300\ nm$). Plane view of the (a.1) regular and (b.1) realistic samples. Spectral variations of the total extinction for the (a.2) regular and (b.2) realistic samples for TE and TM polarizations. Multipole decomposition of the total extinction for the (a.3) regular and (b.3) realistic samples for TE polarization. (a.4-a.7 and b.4-b.6) Cross-section and plane view of the near-field intensity for TE polarization at selected wavelengths that are identified by disks with different colors in a.2 and b.2, respectively. The plane view near-field maps are calculated along the white dashed lines drawn in the cross-section maps, and correspond to the areas limited by a white rectangle in a.1 and b.1, respectively. The cross-section near-field maps are calculated along the red dotted lines drawn in plane view maps. The black dashed lines show the layer interfaces. Illumination from the bottom side with an incidence angle $\theta = 0°$.

sample. However, the regular sample has strong enough similarities to provide a useful comparison with the realistic sample.

For TM polarization, the regular sample exhibits a main peak at 545 nm for the dipolar mode (Figure 4.7a.2 and Figure 4.8). For TE polarization, the main peak of the dipolar mode red-shifts at 622 nm and is accompanied by a second peak at 442 nm (Figure 4.7a.3). A quadrupolar mode adds at 470 nm. Several articles have already reported such a behavior of the dipolar mode when metallic nanoparticles are periodically organized.[22,102] The long-wavelength peak results from the far-field coupling of the localized surface plasmons of individual nanoparticles. For appropriate period of the nanoparticle grating, the field scattered by the nanoparticles arrives in phase with the localized surface plasmon resonance induced by the incident field on adjacent particles, thereby reinforcing the resonance (Figure 4.7a.7 and Figure 4.9). This effect is known as a plasmonic surface lattice resonance and leads to the extinction enhancement at 622 nm. A short-wavelength peak is also reported in some articles with lower amplitude and broader width because of an increased damping.[22] In our layered system, the field enhancement at 442 nm is maximum on the bottom side of nanoparticles and along the TE incident field (Figure 4.7a.4). For TE polarization (along the y axis), we can also highlight at ~518 nm the guided mode excited through diffraction by the nanoparticle periodic array that propagates along the x direction π out-of-phase with the incident field on metallic nanoparticles.[123] The destructive interference of the propagating mode with the incident field on the nanoparticles considerably reduces the nanoparticle absorption and leads to low extinction. The near-field enhancement on the nanoparticle surface is thus low, and the near-field maxima occur in the dielectric layer between nanoparticles (Figure 4.7a.6). At 470 nm the quadrupolar mode exhibits four lobes in the cross-section plane parallel to the incident polarization (Figure 4.7a.5 and Figure 4.9e).

In comparison, the realistic sample exhibits a much broader main dipolar peak than the regular sample, but its maximum also largely red-shifts from 500 nm to 634 nm when rotating the polarization from TM to TE (Figure 4.8b.3 and Figure 4.7b.3). The second dipolar peak at lower wavelength for TE polarization is less obvious, it seems to interfere with the quadrupolar mode. The latter is less sensitive to the incident polarization, broader than for the regular sample and occurs at 490 nm. The near-field intensity map on the cross-section at 534 nm, where total

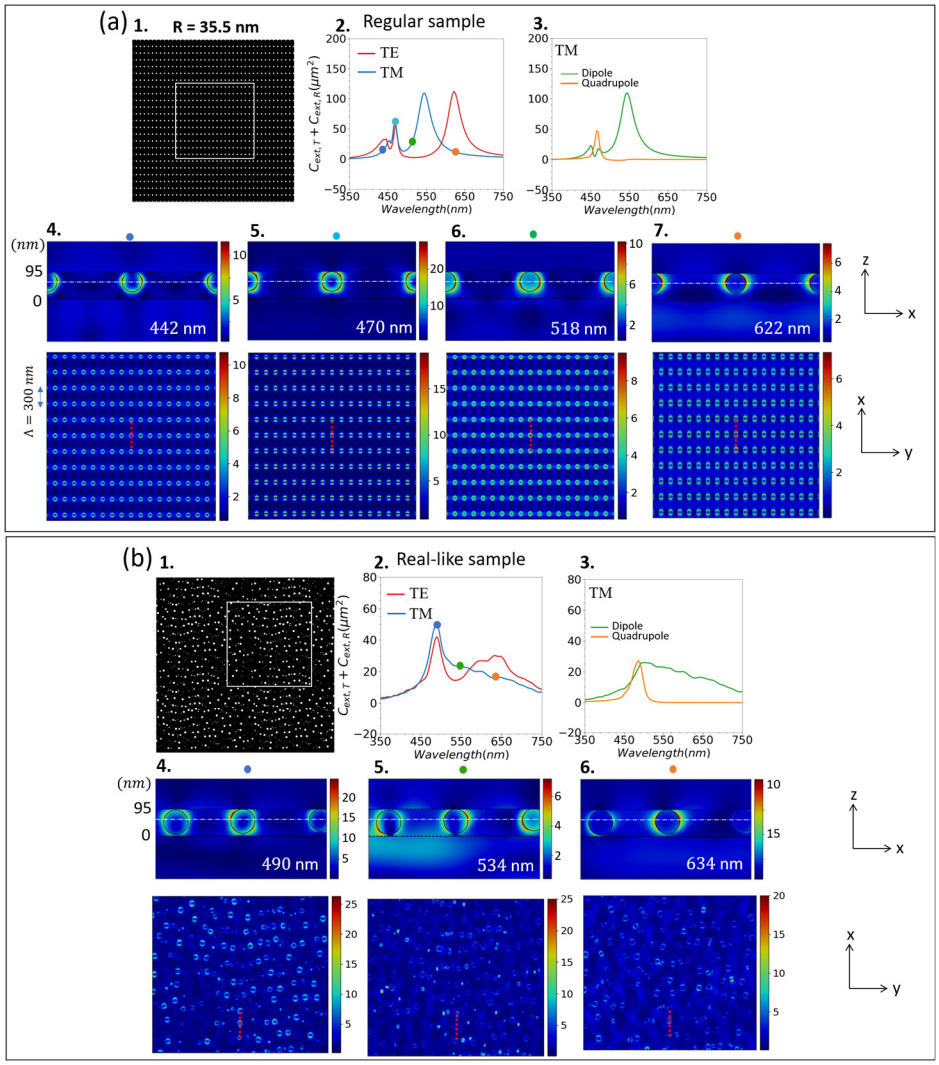

Fig. 4.8. Near-field maps in xz and xy plane of the regular and real-like samples for TM polarization (perpendicular to the grating lines with $\Lambda = 300\ nm$). Plane view of the (a.1) regular and (b.1) real-like samples. Spectral variations of the total extinction for (a.2) regular and (b.2) real-like samples in two incident polarizations for TE and TM polarizations. Multipole decomposition of the incident perpendicular to the laser polarization for (a.3) regular and (b.3) NP arrays. (a.4-a.7 and b.4-b.6) cross section and plane view of the near-field calculation at the selected wavelengths (depicted as circles with different colors shown in fig. a1 and b.1 respectively). The near-field intensities of the plane view are calculated on the white dashed lines drawn in the cross section pictures, corresponding to the areas limited by white rectangles shown in fig. a.1 and b.1 respectively. The near-field intensities of the plane view are calculated on the red dotted lines drawn in plane view pictures. The black dashed lines correspond to the layer interfaces.

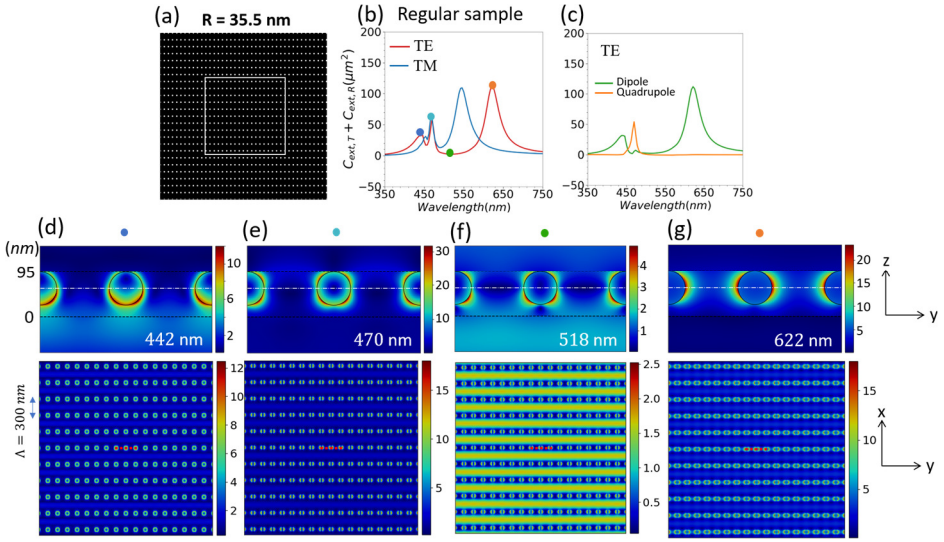

Fig. 4.9. Near-field maps in yz and xy plane of the regular and real-like samples for TE polarization (parallel to the grating lines with $\Lambda = 300\ nm$). Plane view of the (a) regular. Spectral variations of the total extinction for (b) regular in two incident polarizations. Multipole decomposition of the incident perpendicular to the laser polarization for (c) regular NP arrays. (d-g) cross section and plane view of the near-field calculation at the selected wavelengths (depicted as circles with different colors shown in Fig. b). The near-field intensities of the plane view are calculated on the white dotted dashed lines drawn in the cross-section pictures, corresponding to the areas limited by white rectangles shown in fig. a. The near-field intensities of the plane view are calculated on the red dotted lines drawn in plane view pictures. The black dashed lines correspond to the layer interfaces.

extinction is the lowest, evidences a reduced field enhancement at the nanoparticle surface and a field maximum between nanoparticles (Figure 4.7b.5). This behavior tends to evidence the occurrence of a plasmonic lattice mode resonance, although the corresponding effect is limited by the size heterogeneity and the spatial disorder of nanoparticles. Indeed, as shown in the plane view of Figure 4.7b.5, some nanoparticle sizes resonate at 534 nm (red nanoparticles). And, spatial disorder introduces phase variations between the field scattered by nanoparticles along the x direction that reduce the coupling efficiency in the guided mode. Size heterogeneity and spatial disorder are thus limiting factors to observe the field enhancement at the long-wavelength peak in these laser-induced samples.

However, a strong dichroism is observed in these realistic samples due to the difference between the main dipolar peaks obtained for TM and TE polarization. This dichroism is actually reinforced by another phenomenon that does not occur in the regular sample and that is highlighted in Figure 4.10: the near-field coupling between close nanoparticles. The plane-view of the near-field intensity at 634 nm in Fig. 4.7b6 shows that different pairs of close nanoparticles, found along the irregular lines, resonate at this wavelength (white rectangles). This near-field coupling leads to hybrid modes whose resonance frequencies are polarization dependent and for which the high frequency mode is usually a dark mode.[174–177] As shown in Figure 4.10, nanoparticle dimers

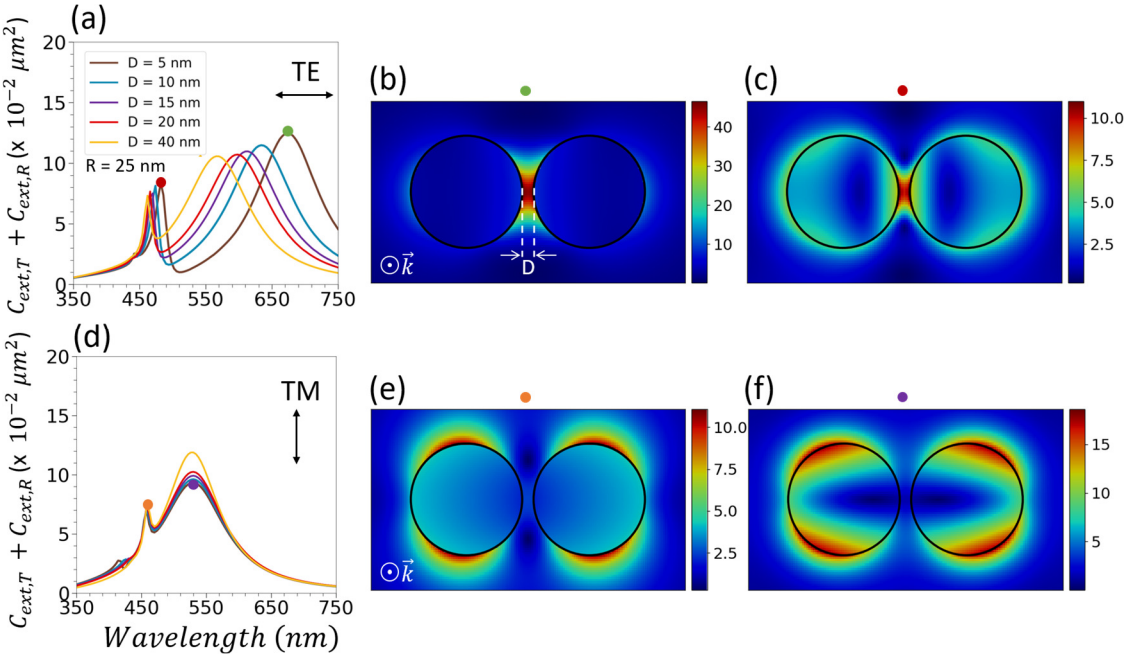

Fig. 4.10. Near-field coupling. (a, d) Total extinction cross section of a dimer in the layered system (Fig. 4.5c) with varying interparticle distances for TE (along the dimer axis) and TM (perpendicular to the dimer axis) polarizations, respectively. Field enhancement in plan-view for dipolar (b, e) and quadrupolar (c, f) resonances for both polarizations. Particle size is 50 nm in diameter.

embedded in a high index layer and tangent to the top interface, as described in Figure 4.5c, exhibit a dipolar resonance for TE polarization (the bright hybrid mode) whose position red-shifts when the distance between nanoparticles decreases. The narrow peak at around 470 *nm* that corresponds to a quadrupolar resonance, also slightly red-shifts. As the gap decreases the coupling between nanoparticles increases and the near field enhancement in the gap rises. Conversely, the resonance

positions for TM polarization remain nearly unchanged, and the corresponding near-field map (Fig. 4.10e&f) show no indication of coupling between the resonance modes. These simulations demonstrate that the broad dipolar resonance of the realistic samples that peaks at low wavelength for TM (Figure 4.8b.3) and at high wavelength for TE (Figure 4.7b.3) is not only due to the size dispersion, but also to the variable distances between particles that lie along a same grating line. Note that the small peaks at the shoulder of the broad dipolar resonances in TE polarization only

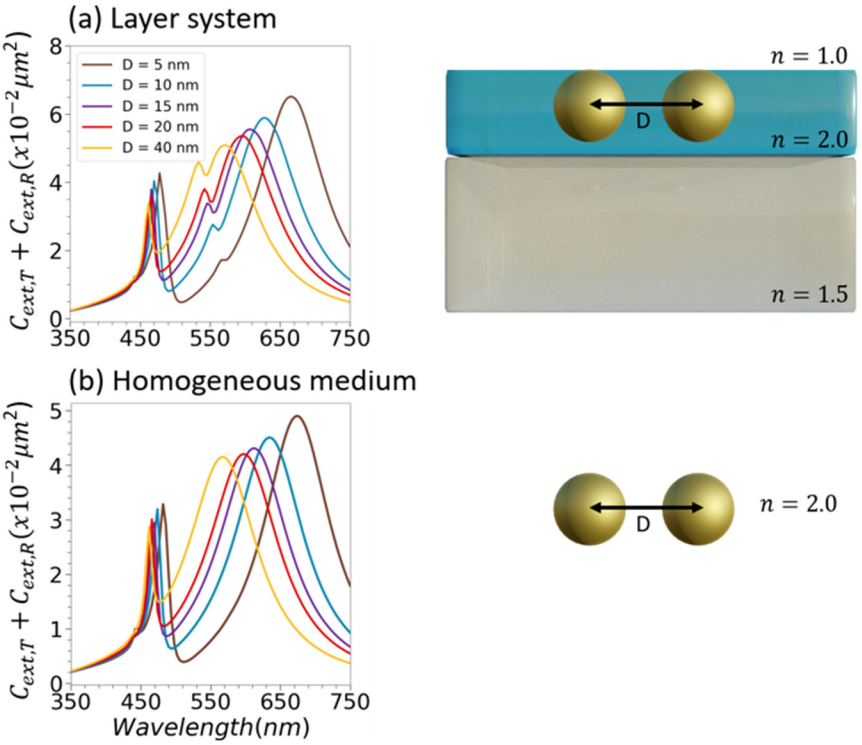

Fig. 4.11. Total extinction cross section of a dimer in layered system (a) and homogeneous medium (b), and their corresponding structural cross sections. The incidence polarization is parallel to the dimer axis.

appear when the nanoparticles are embedded in a layered system as shown in Figure 4.11. This small peak can be attributed to the interaction of the coupled dipolar resonance with the close air-TiO_2 interface. This small peak is not observed in the realistic sample because of the heterogeneous broadening of the dipolar resonance. It is important to emphasize that simulations in Figure 4.10 and 4.11 involve only two particles, resulting in an extinction cross section on the order of 10^{-2} μm^2, in contrast to large simulated array in Figure 4.19, which exhibits an extinction cross section on the order of 100 μm^2.

To summarize, the dichroic behavior of the extinction cross-section of realistic samples turns to result from two optical mechanisms. The first one originates from the near-field coupling between the LSPR of close nanoparticles that can be found along the grating lines. It leads to mode hybridization with a resonance position that is strongly dependent on the distance between close nanoparticles, and their respective diameter too, for TE polarization. The second one originates from the far-field coupling between the LSPR mode of nanoparticles through the excitation of a photonic mode that interfere constructively with the incident field on the nanoparticles at a specific wavelength that depends on the grating period. While carried out on specific samples, these results can be generalized to all metasurfaces where self-organized nanoparticle gratings are observed.

4.5 Considerations on diffraction by nanoparticle gratings.

Diffraction by the laser-induced metasurfaces shown in Figure 4.1 and 4.2 results either from surface topography gratings or from coherent scattering by self-organized nanoparticles. While diffraction by periodic surface corrugation has been investigated in the literature,[45,46] it is worth investigating the influence of some parameters of the nanoparticle arrays on diffraction. The study is based on the analysis of the spectral variations of the scattering cross-section and the angular variations, in the incidence plane, of the differential scattering cross section (defined in Section 1.2.5) at selected wavelengths. A sample, described in Figure 4.12, is selected from Figure 4.1b based on its diffraction properties and the absence of surface modulation grating. This sample exhibits Ag nanoparticles that are semi-embedded at the top surface. A realistic sample, modeled in Figure 4.13a is created from the SEM plane-view and TEM cross-section, and compared to the closest regular sample presented in Figure 4.13b in which 44 nm wide spherical nanoparticles are separated by a period of 325 nm along the x direction and 100 nm along the y direction. As the semi-embedded nanoparticles cannot be simulated with the used modeling, two configurations are considered, with Ag nanoparticles either supported on the TiO_2 surface or inside the TiO_2 layer where the biggest particle are tangent to the top interface (the relative position of particles are kept unchanged in the two configurations).

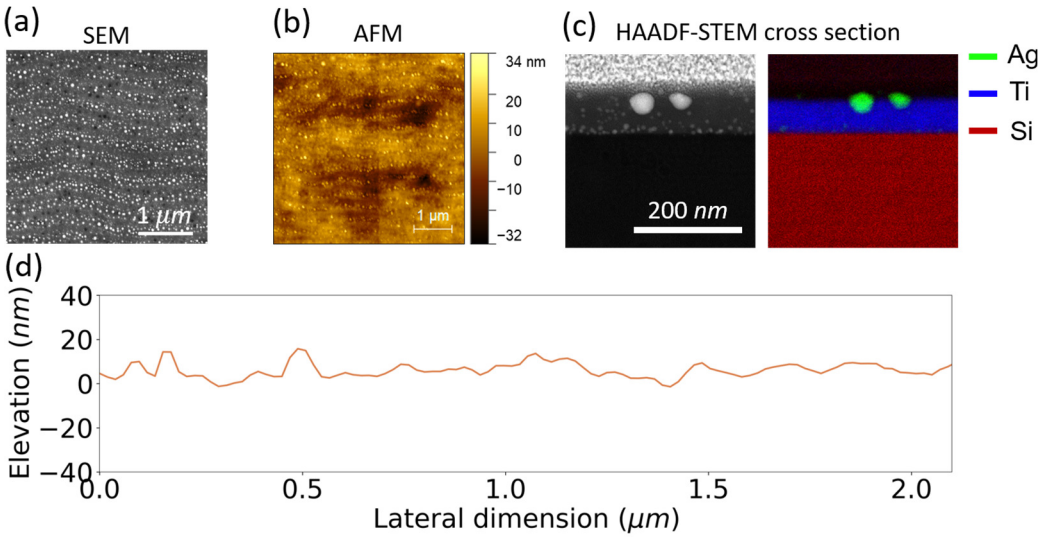

Figure 4.12. Characterization of sample induced by laser at 100 kHz repetition rate, 245 mmJ.cm-2 laser fluence, 100 mm.s-1 scan speed and 2 μm laser lines distance. (a) Plane view of the SEM image. (b) Atomic force microscopy (AFM) characterization. (c) Annular dark field (ADF) image (left image) and energy dispersive spectroscopy (EDS) chemical mapping (right image). (d) surface morphology perpendicular to the grating line of the sample.

The samples are illuminated by a TE polarized plane wave under 60° of incidence (θ_i) from the top (air), the incidence plane being perpendicular to the y axis. The scattering cross-sections in reflection of the realistic and regular samples exhibit similar spectra for both configurations where Ag nanoparticles are either in or out the TiO_2 layer (Figure 4.13a.5 and 4.13b.5). For particles inside the TiO_2 film, a main peak, corresponding to a dipolar mode dominates the (green) spectrum at 507 nm for the realistic sample and 524 nm for the regular sample, while this dipolar peak blue-shifts in the violet at 374 nm, respectively, when nanoparticles are on top. Considering the period $\Lambda = 325$ nm for the realistic and regular samples and using the grating equation $\sin(\theta_m) = \sin(\theta_i) - \lambda/\Lambda$, one can calculate the -1st diffraction angle at -43.9° for 507 nm wavelength, -48.3° for 524 nm, -16.5° for 374 nm. These angles are actually the ones at which the maximum scattering efficiency is found on the left-end side of the angular scattering diagrams in Figure 4.13. It is interesting to note that the amplitude of the scattering cross-section maximum is almost the same for the realistic and regular samples (slightly higher for the latter). However, the maximum

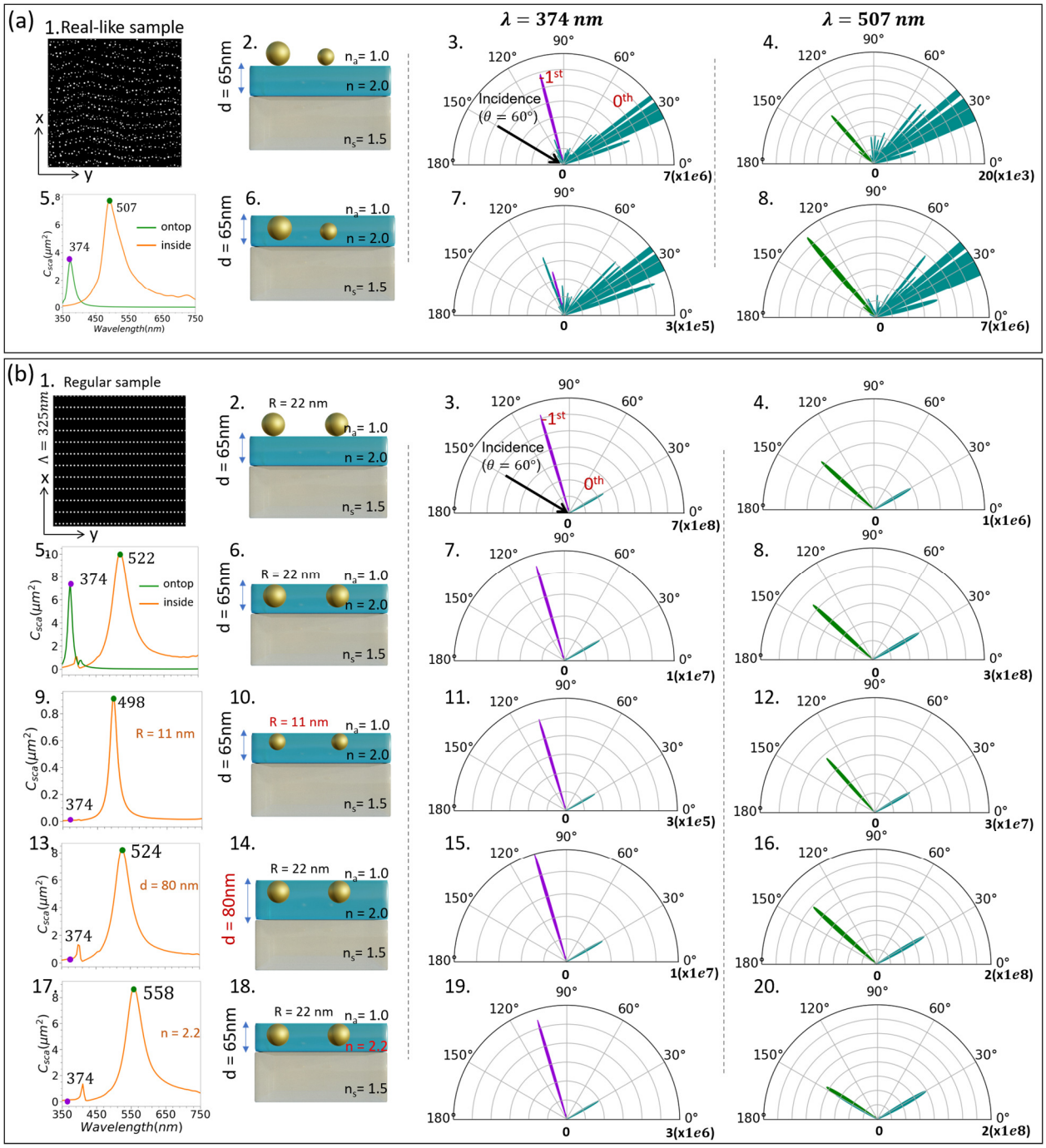

Figure 4.13. Influence of metasurface structural parameters on the diffraction. Plane view of the realistic (a.1) and regular samples (b.1). Scattering cross section in reflection side of realistic (a.5) and regular (b.5, 9, 13, 17) samples. Cross section views of realistic (a.2, 6) and regular (b.2, 6, 10, 14, 18) samples. Scattered radiation at the selected wavelengths of the realistic (a.3, 4, 7, 8) and regular (b.3, 4, 7, 8, 11, 12, 15, 16, 19, 20) samples. Unit of the differential scattering cross section is nm2/steradian.

diffracted intensity in the -1st diffraction order is 30 to 40 times higher in the regular sample than in the realistic sample if we compare the on top configurations in the violet and the inside configurations in the green. This huge difference results from the heterogeneity of the realistic sample that scatters a lot of light in a ±20° angular range around the specular direction, whatever the wavelength. Note that, as expected from the scattering spectra, the diffracted intensity in the violet -1st order is much higher for the on top configurations than for the inside configurations and vice versa in the green -1st diffraction order.

As observed from the characterizations of 4.12, Ag nanoparticles of the real sample are rather like Janus particles with their top half located in the air and their bottom half located in the TiO_2. This sample is then expected to exhibit a maximum diffraction efficiency between the violet and the green. It is actually with a diffraction angle at -28° to record a blue diffracted light that the pictures of Figure 1b (triangles #1) were taken to visually observe a high diffracted intensity. One can also note that the exposure time of the camera was increased by 40 between the recording of diffraction images and the pictures recorded in the front side reflection mode. Our simulations thus fairly well match the experimental observations.

Simulations also allow studying the influence of some sample parameters individually. Figures 4.13b.9-12 show that dividing the nanoparticle size by 2 from 44 nm to 22 nm divides the maximum diffraction intensity in the green -1st order by a factor 10. Increasing the TiO_2 thickness by 25% (Figures 4.13b.13-16) or its refractive index by 10% (Figures 4.13b.17-20) slightly reduces the maximum diffraction efficiency in the green -1st order by a factor 1.5.

To summarize the results about diffraction by nanoparticle gratings, one can keep in mind the following information. Grating period is fixed by the laser wavelength and the type of resonance excited during laser processing; the grating period determines the diffraction angle. The disorder that affects the spatial distribution of self-organized Ag nanoparticles strongly reduces the diffraction efficiency, which however remains observable by the naked eye. The diffraction efficiency is greatly enhanced in the visible range when Ag nanoparticles are embedded in the top layer. And, the higher the refractive index or thickness of the top layer, the lower the diffraction efficiency.

4.6 Printed plasmonic color images

In this part, we show the degree of fidelity that laser processing of quasi-random plasmonic metasurfaces allows to reach when printing color images. We also demonstrate that targeted colors can be printed to be observed specifically in some modes of observation and disappear in other modes. This property has actually an interest for security printing. Contrary to ink-based techniques, which involve limited numbers of primary colors that are mixed together to create a full color image, laser processing prints as many primaries as colors present in the image to print. Each laser processing parameter set creates a specific type of metasurface that is associated to a given color in a particular mode of observation. The same laser-processed metasurface exhibits different colors in different modes of observation. Once the color databases observable in the different modes of observation are recorded by varying the laser processing parameters, one can implement a gamut mapping algorithm associated with a halftoning technique, to print by laser color images that are as faithful as possible to the original image.[38] The resulting colors originate from the combination of scattering, absorption, diffraction and interference. Figure 4.14 shows two images whose original colors were reproduced with a good fidelity either in a backside specular reflection observation mode (Figure 4.14b) or in a transmission observation mode involving polarized light (Figure 4.14c). The configurations of the observation modes are described in Figure 4.14a. The image size is 13 x 11 mm^2 with a pixel of size 50 x 50 μm^2. Interestingly, the image in Figure 4.14b contains metasurfaces that diffract light in the plane of incidence either when the image is fixed horizontally on the measurement setup ($\beta = 0°$), or when it is rotated by $\beta = 90°$. Different images are then recorded with a diffraction measurement setup in which different parts lit depending on the sample orientation. The combination of these images can be used to authenticate a secured printing. Whitish areas that occur in the two diffraction images correspond to metasurfaces that scatter light in a broad range of wavelengths rather than diffracting it.

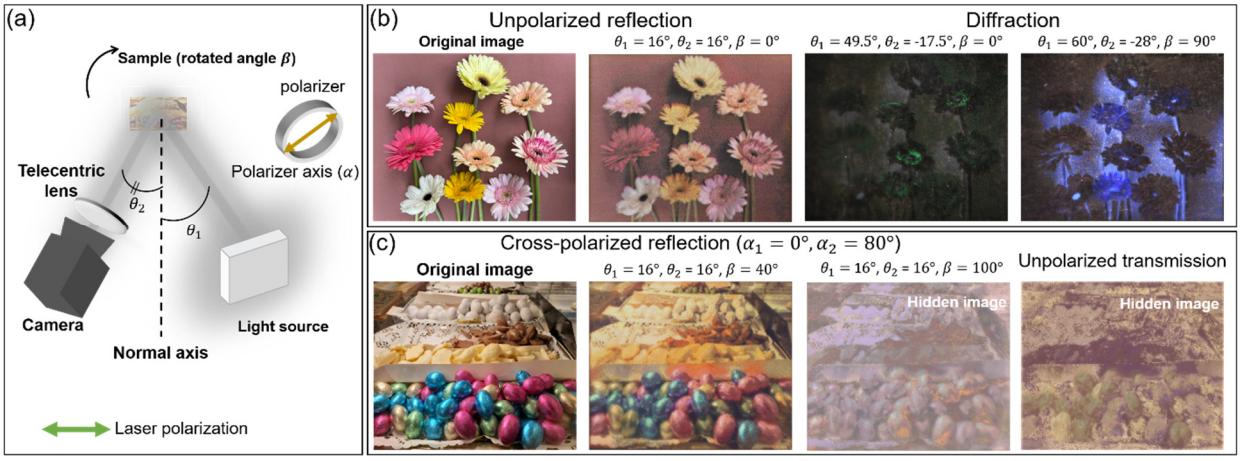

Figure 4.14. (a) Color acquisition setup for recording the printed images in different observation modes. The printed images are compared with the original ones. (b) Color printed image observed in unpolarized reflection and diffraction modes. (c) Color printed image observed in cross-polarized reflection (two polarizers are placed in front of the source and telecentric lens) and unpolarized transmission mode.

Figure 4.14c demonstrates the ability to reproduce faithfully different types of colors in a polarized observation mode where the sample is placed between two polarizers whose axes form an angle of 80° (cross polarizer) and is observed in reflection. The value is chosen to optimize the observed dichroic color without diminishing the observed light intensity. In this case, faithful colors are observed for a specific orientation of the sample between the two polarizers, and as soon as it is rotated in its plane (different β value) or observed under non-polarized light, colors vanish. The sample observation under other modes are provided in Figure 4.15. These images indicate the wide variety of metasurfaces that can be produced by laser and combined to generate secured color images.

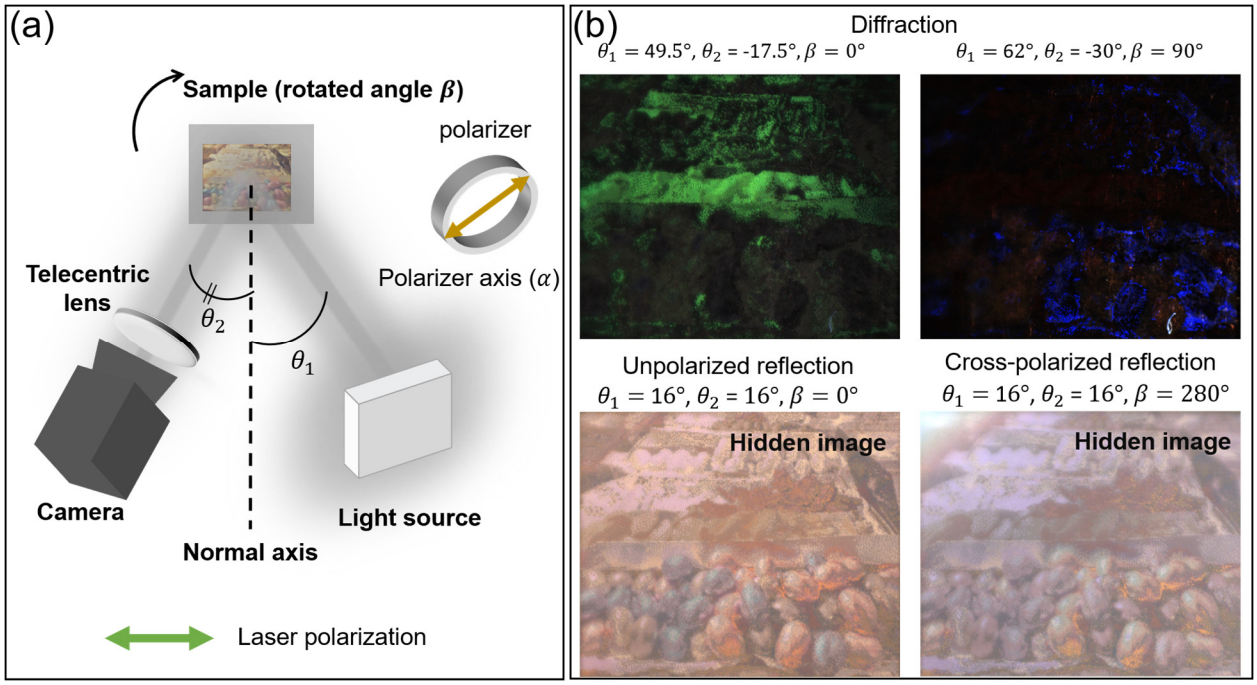

Figure 4.15. (a) Color acquisition sketch for capturing the printed images in different modes. (b) Color printed image observed in diffraction, unpolarized reflection and cross-polarized reflection modes.

4.7 Conclusion

The chapter demonstrates the great potential of a single step nanosecond laser based technology for the production of metasurfaces with a wide range of optical properties. By varying the processing parameters, metasurfaces that exhibit simultaneously or independently diffractive and dichroic properties can be produced. Using electromagnetic simulations, the chapter highlights the contribution of two optical mechanisms to the observed dichroism, which involve either the near-field coupling of close nanoparticles located along the grating lines or the coherent far-field coupling between periodically spaced nanoparticle lines. The former results in the hybridization of LPSR modes and makes the resonance position strongly dependent on the distance between close nanoparticles for TE polarization only. The heterogeneity in size and distance of the hybridized pairs broadens the resonance, but does not prevent the polarization sensitivity. The latter results in a near-field enhancement on the nanoparticle surface that is shifted toward long-wavelength for TE polarization only. The disorder and size dispersion attenuate the coupling

strength. Furthermore, the observed diffraction originates from two main self-organization structures: nanoparticle gratings and surface topography gratings. The contribution of the nanoparticle gratings to diffraction is higher when they are embedded. Leveraging the optical properties of laser-induced metasurfaces, we successfully demonstrate the printing of color images, which can be observed in specific modes while being hidden in other modes. This technology exhibits great promise for advanced applications in the fields of security, display or vision.

5 Diffraction properties of three superimposed grating structures induced by cw laser

Controlling diffraction properties of materials over a large area is highly promising for a wide range optics-related application. Laser-based techniques appear to be a good candidate to meet this demand. Here, we present diffraction properties of laser-induced self-organized structures. The latter consists of three interlaced grating-like structures, including self-organization of nanoparticles, laser-induced defect and laser marking lines. When illuminated by an external incidence under the normal incidence, the sample exhibit an asymmetric diffraction pattern. While, tilting the incidence angle, circular diffraction patterns are captured on the plane perpendicular to the sample and incidence plane. This is found to be the combination effect of the three diffracted gratings. To unveil the underlying physics of the diffractions, we use rigorous coupled-wave analysis (RCWA) and grating equations written in direction cosine space expanded for three superimposed gratings. These diffraction properties of the samples empowered by laser can be highly potential for industrial implementations, such as security, display or design.

5.1 Introduction

Diffraction grating is the fundamental optical component that splits and diffracts incoming light into different specific directions.[178,179] The diffracted field results from gratings acting as a phase modulating structure, which imposes periodic phase variation on the incoming electromagnetic wave. Such grating structures are made of periodically spaced formation at wavelength scale. Diffraction grating is of great interest in a wide range of applications, such as sensing,[180–182] security,[183,184] data storing,[185] holography,[186–191] surface plasmon resonance,[192] beam splitter[193] or wave coupler.[194]

Over the past decades, rapid advances in laser-induced periodic structures (LIPSs) has enabled to customize diffraction grating for real-world applications, owing to the simplicity and cost-effectiveness of the single-step process. LIPSs are global phenomenon that can be excited on most of materials, arising from the interference of the incident laser with excited electromagnetic

modes.[52,195] The latter can be surface plasmon polariton or excited guided wave. LIPSs have a huge potential for applications related to optics, [39,48,196,197] biology [198,199] or other technical fields.[200,201] Recently, self-organization of Ag-based nanocomposites produced by lasers have shown great promise for visual effects or security features owing to diffractive colors arising from nanoparticle (NP) or surface gratings.[52,53]

Here, we investigate the optical diffraction properties of self-organized Ag-dielectric nanocomposites generated by continuous laser beam, consisting of three superimposed grating structures. The self-organized mechanism,[47] dichroic color properties [152] and other physical chemistry aspects [49,50,154,202] of the sample have been intensely studied previously. However, the diffraction properties of these interlaced grating structures are left unanswered. Using a custom 2D rigorous coupled-wave analysis (RCWA),[76,203,204] we unveil the underlying physics of the asymmetric diffraction pattern of the sample under normal incidence. In addition, by applying the grating equations in direction cosine space [205,206] expanded for three grating structures, we reveal the combination diffraction effects of the superimposed gratings, giving rise to an interesting circular diffraction pattern of the sample under oblique incidence. These emerging diffraction properties of the sample induced by laser can be vast potential for mass manufacturing of optical devices used in security tags.

5.2 Sample characterization

The samples in this study compose of amorphous TiO_2 thin film loaded with small silver nanoparticles deposited on glass substrates. Detail about sample preparation can be referred to our previous articles.[47,152] The samples are exposed under an Ar-Kr continuous laser at λ = 488 nm, and constant power of P = 250 mW whose intensity is focused on the sample by a 10x microscope objective under normal incidence. The samples are placed on a translation stage, which can move at different constant speeds (scan speed) and marked by consecutively identical laser lines with the spacing of 12 μm. These laser lines form the first grating structure with the period equal to the spacing. In this study, we investigate samples inscribed by the scan speed from 100 μm/s to 3000 μm/s.

5.3 Direction cosine space

Before jumping into the investigation of the diffraction properties of the sample, it is necessary to present the concept of grating equation in direction cosine space. Diffraction grating written in term of direction cosine provides a simple yet powerful way to visualize and understand the diffraction behavior of grating structures especially for oblique incident angles.[205,206] Figure 5.1 shows a sketch illustrating the position of diffraction orders for an arbitrary oblique incidence in direction cosine space (in reflection side), where the coordinates of diffraction orders can be determined using the following equations (assuming the refractive index of surrounding medium is 1)

$$\alpha_m = \alpha_i + \frac{m\lambda}{\Lambda}, \beta_m = -\beta_i \tag{5.1}$$

Where $\alpha_m = \sin\theta_m \cos\phi_0, \alpha_i = -\sin\theta_0 \cos\phi_0, \beta_i = -\sin\phi_0$, λ is the incidence wavelength, Λ is the grating period and m = 0,±1,±2,±3,…

The diffraction orders are basically the projections of the intersection of diffracted beam with the hemisphere with a unit radius. As shown in Fig. 5.1, positions of diffraction orders are equally spaced and located on a straight line perpendicular to the grating lines. Notice that only diffraction orders lie within the hemisphere are real and carry energy, diffraction orders lie outside the hemisphere correspond to evanescent waves.

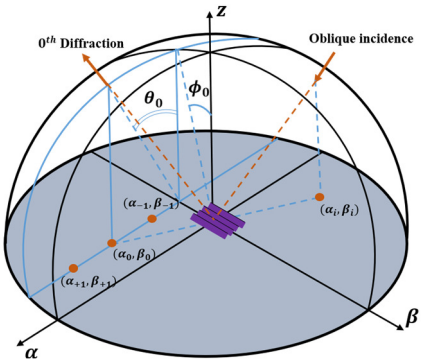

Fig. 5.1. Positions of incidence and diffraction orders in direction cosine space denoted as α, β which the subscript "i" for incidence, "0" for 0th diffraction orders, "+1" for +1st diffraction orders, and "-1" for -1st diffraction orders.

5.4 Asymmetric diffraction pattern under normal incidence

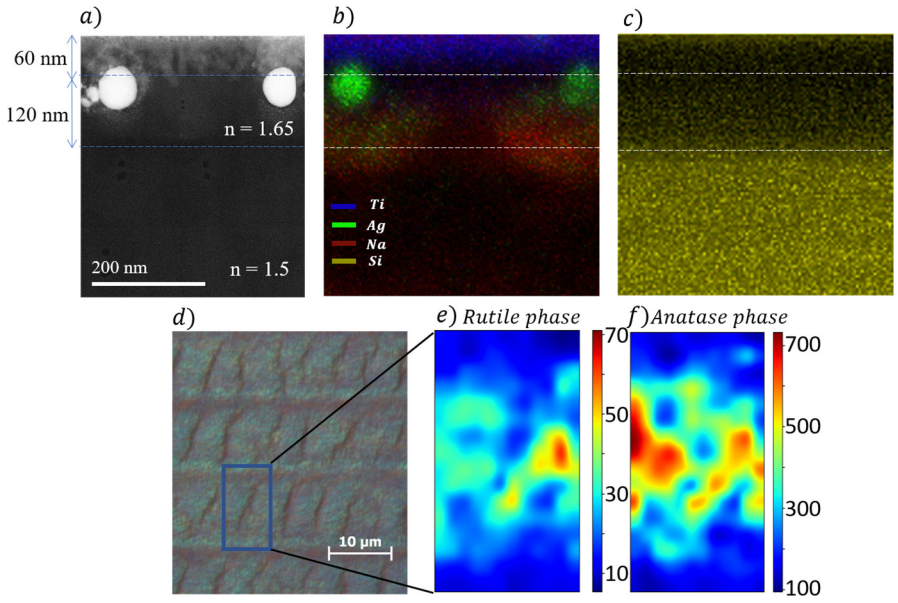

Fig. 5.2. Characterization of the sample illuminated by 300 µm/s scan speed: (a) cross view of the sample, (b-c) Chemical components of the sample, (d) optical microscope with the area highlighted in blue is used for Raman analysis, (e) Rutile phase intensity of Raman spectrum calculated at 237 cm^{-1}, 446 cm^{-1}, 611 cm^{-1}, (f) anatase phase intensity of Raman spectrum calculated at 144cm^{-1}

The first interesting diffraction feature of the sample is the asymmetric patterns that appear under normal incidence. These diffraction patterns are projected onto a screen 30 cm away from the sample and perpendicular to the incident laser beam with λ = 514.5 nm. To directly measure the positions of the diffraction orders, a sheet of paper is used as a screen with the size for each small square is equal to 1x1 cm^2 (as shown in Fig. 5.4e). The sample under the investigation is inscribed by 300 µm/s scan speed with the characterizations provided in Fig. 5.2. Figure 5.4a, b show the sample viewed under optical microscope and scanning electron microscope, where laser marking lines form a grating structure perpendicular to the α-axis with the period of Λ_1 = 12 µm. In addition, under the laser process, a regular defect arises, forming another grating structure with the period of $\Lambda_2 \approx 5$ µm. The origin of the laser-induced defect remains an open question and will be studied elsewhere. Here, we focus our attention on the diffraction properties generated by these gratings. In fact, laser can also trigger the self-organization of nanoparticles embedded in thin film,[47] whose

period is determined as $\Lambda = \lambda / \mathrm{Re}(n)$ with Re(n) is the real part of the effective refractive index of the surrounding medium. However, in this configuration, this subwavelength grating does not diffract light. This can be easily verified using equation (1), where $\alpha_i = 0$ and $\lambda / \Lambda > 1$, leading to $\alpha_m > 1$, $\forall m \neq 0$, which is outside of the hemisphere, indicating that other diffraction orders except 0th order do not exist. Coming back to the diffraction properties produced by the two grating structures, to unveil the underlying physics of the asymmetric diffraction patterns, we employ the diffraction equation written in cosine space for two superimposed gratings.[205,206]

$$\alpha_m = \alpha_i + \frac{m\lambda}{\Lambda_2}, \beta_m = -\beta_i + \frac{n\lambda}{\Lambda_1} \tag{5.2}$$

where m, n are the diffraction orders of the grating with Λ_2 and Λ_1 respectively. Then the positions of diffraction orders will be project to the screen using simple geometry as explained in Fig. 5.3. The position of the diffraction order on the unit sphere can be determined by the grating equations in direction cosine space. Assuming that the diffraction on the unit sphere is C(α_m, β_m, z_m), the projection of C on the screen is D(α_p, β_p, z_p), whose position can be evaluated using the following equations:

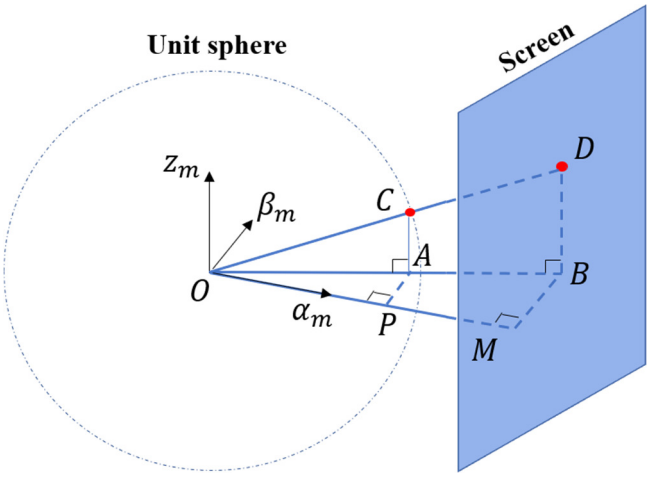

Fig. 5.3. Projection of the diffraction order on the unit sphere and the screen. The screen is perpendicular to the α_m -axis

$$\frac{DB}{CA} = \frac{OB}{OA} = \frac{MO}{PO} \rightarrow DB = \frac{MO}{PO} CA = \frac{MO}{\alpha_m} z_m \rightarrow z_p = \frac{MO}{\alpha_m} z_m \tag{5.3}$$

$$\frac{MB}{PA} = \frac{MO}{PO} = \frac{MO}{\alpha_m} \rightarrow \beta_p = MB = \frac{MO}{\alpha_m}\beta_m \rightarrow \alpha_p = MO \tag{5.4}$$

Where MO is the distance between the screen and O. After determining the positions of diffraction orders, the intensity distribution can be calculated using RCWA with the modeled structures are shown in Fig. 5.4c (plane view) and Fig. 5.4d (cross view), created by mimicking sample topology characterized by SEM in Figure 5.4a, TEM and Raman analysis in Figure 5.2. The refractive indices of the layers are approximated for the simplification. In fact, in the following simulations, the refractive indices of the materials play an insignificant role in controlling the asymmetric diffractive patterns. Figure 5.4c shows plane view of a unit cell for the simulation with the width of 5 μm, the height of 12 μm and a slanted line in the middle representing the defect. Figure 5.4f displays the simulation result, where each green dot corresponds to the diffraction orders and their sizes are proportional to the diffraction efficiencies. Notice that the size of 0^{th} diffraction order is deliberately reduced for better visualization, because its diffraction intensity is much higher than other diffraction orders. Comparing the diffraction pattern with the experimental measurement, a good agreement can be seen. It is thus can be concluded that the geometrical shape

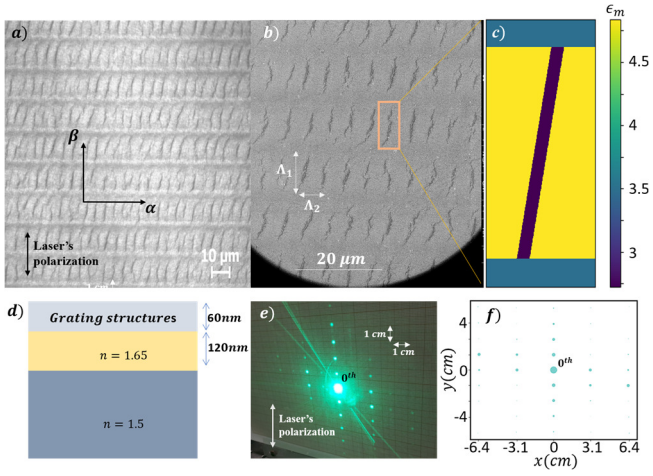

Fig. 5.4. (a, b) Optical Microscope and SEM pictures of the sample illuminated by the laser with scanning speed of 300 *μm/s*. (c) Simulated unit cell of the sample in RCWA with the color bar represents relative permittivity of the grating structures. (d) Cross view of the simulated sample (e) Diffraction pattern of the samples shown in experiment captured on a screen. (f) Simulation results of the sample with each dot represent the diffraction orders and their sizes are proportional to the diffraction efficiency (except the 0^{th} diffraction order)

of the gratings explains the asymmetry, where the slanted grating tilted to the right. Figure 5.5 further validates the dependence of the diffraction pattern on the grating shape. While changing the refractive indices of the materials, the diffraction pattern remains unchanged (Fig. 5.5b), however when the slanted grating is flipped, the diffraction pattern is flipped correspondingly (Fig. 5.5d). This is also the case when we flip our sample in the measurement as shown in Fig. 5.5e.

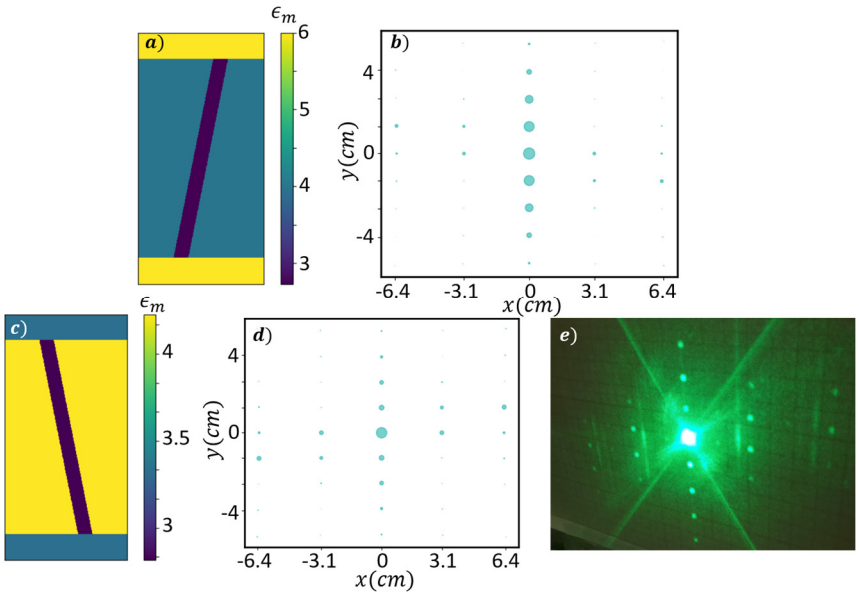

Fig. 5.5. (a, c) Simulated unit cells of the sample in RCWA with the color bar represents relative permittivity of the grating structures with the same cross section shown in Fig. 5.4d. (b, d) Simulation results correspond to grating structure with unit cells in a & c respectively. (e) Diffraction patterns of the rotated sample in simulation in comparison with the simulation in d.

5.5 Circular diffraction pattern under inclined incidence

As mentioned in the previous section, the nanoparticle grating does not diffract light under normal incidence due to the subwavelength period. However, the diffracted light from the grating can be captured under oblique incidence angle as shown in Figure 5.6, which will be further discussed herein. Figure 5.6a shows the SEM image of the sample at 100 μm/s, where the nanoparticle grating with the period of $\Lambda_3 = 344$ nm is highlighted. The grating forms curvatures that matches the arc of circle with an angle of 31.40°. Under the incidence angle of $\theta = 35°$ and the wavelength

of λ = 514.5 nm, unique circular diffraction patterns captured on the screen, perpendicular to the incidence plane and sample, at the distance

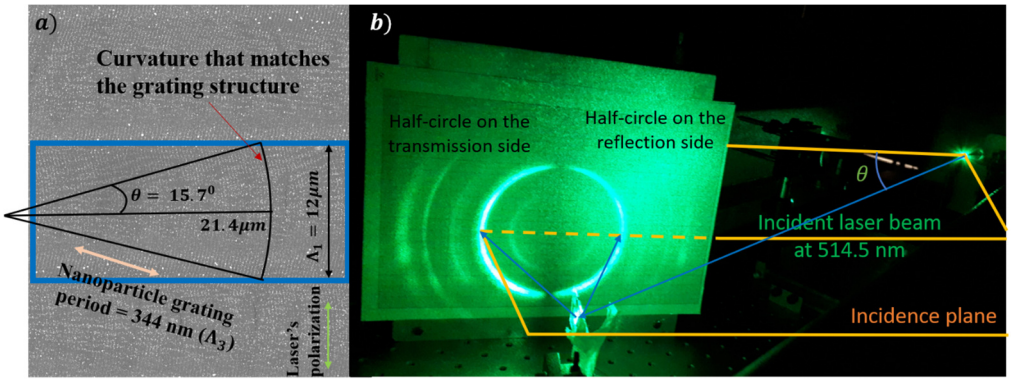

Fig. 5.6. (a) SEM pictures of the sample illuminated by a laser beam with scan speed of 100 μm/s. The nanoparticle grating is highlighted that matches with the curvature with an angle of 31.40. (b) Diffraction pattern of the sample observed under an incident laser light of λ=514.5 nm and θ = 350, captured onto a screen perpendicular to the sample and incidence plane

of 15.7 cm away from the sample. Reminding that the sample is consisted of three superimposed gratings and they all exhibit diffraction under the illumination conditions. Therefore, to understand the origin of the diffraction pattern, we step by step investigate the contribution of each grating to the diffraction property. The investigation is organized as Fig. 5.7, where we first determine the position of diffraction orders of the cross grating with Λ_1 = 12 μm and Λ_3 = 344 nm. Using equation 5.2 for the gratings with Λ_1 = 12 μm and Λ_3 = 344 nm, we calculate the positions (α_m, β_m, z_m) and then project them on the unit sphere (in reflection side), with $z_m = \sqrt{1 - (\alpha_m^2 + \beta_m^2)}$. Then the diffraction orders are projected to the screen with the same configuration as the experiment (Fig. 5.3). According to equation 5.2, only the 1st diffraction order (m = 1) of the grating with Λ_1 = 12 μm is satisfied, whereas diffraction orders for the grating with Λ_2 = 344 nm are restricted from -9 ≤n ≤9, as displayed in Fig. 5.7b & c. The next step is to plot the position of diffraction orders generated by the 2D grating but the grating with Λ_3 = 344 nm is now curved, with the tangent line (Fig. 5.7a) making an angle of 74.3 ≤ψ ≤105.7 to the α-axis, to mimic the nanoparticle grating shown in Fig. 5.6a. The structure can be seen as many 2D gratings combined, with arbitrary orientations determined by Ψ. To understand the diffraction behavior of these gratings, we apply

the general grating equation (in reflection side) in direction cosine space with arbitrary orientations to determine the position of diffraction orders on the unit sphere:

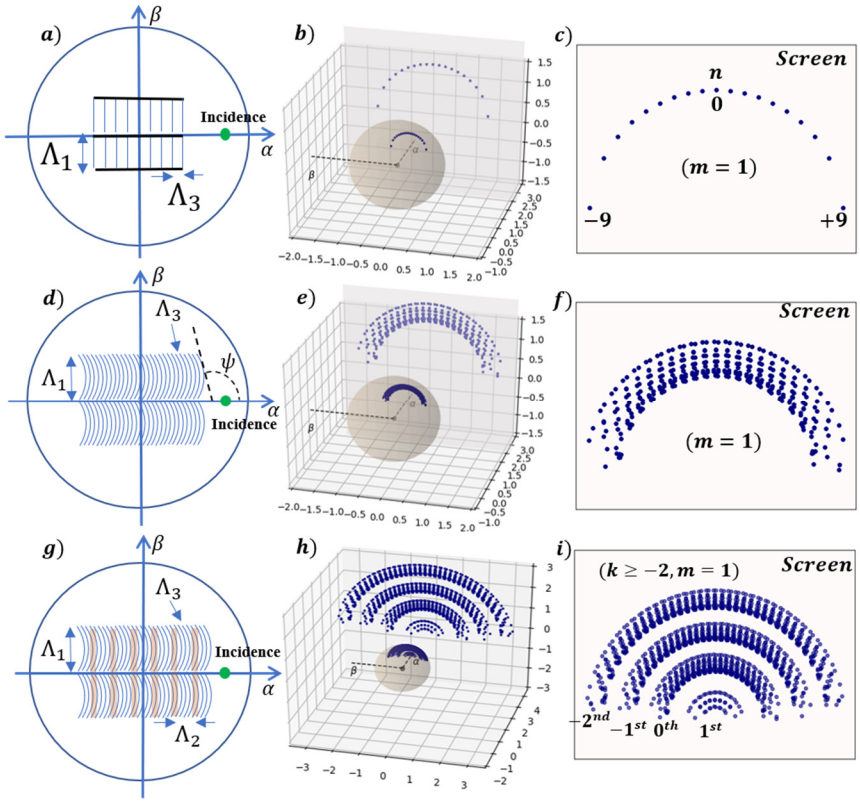

Fig. 5.7. Illustration of the position of incidence (green dots) and diffraction orders on unit sphere and screen with different grating structures illuminated by incident beam with $\lambda = 514.5$ nm and $\theta = 35^0$. Position of diffraction orders on the unit sphere and screen, (a-c) for the gratings with $\Lambda_1 = 12$ µm, $\Lambda_3 = 340$ nm, (d-f) for the gratings with $\Lambda_1 = 12$ µm, $\Lambda_3 = 340$ nm, but the latter is consisted of circular arcs with tangent line making an angle of $74.3 \leq \psi \leq 105.7$, (g-i) for three grating structures with $\Lambda_1 = 12$ µm, $\Lambda_2 = 5$ µm, $\Lambda_3 = 344$ nm

$$\alpha_{m,n} = -\alpha_i + \frac{m\lambda}{\Lambda_3} sin\Psi, \beta_{m,n} = -\beta_i + \frac{m\lambda}{\Lambda_3} cos\Psi + \frac{n\lambda}{\Lambda_1}, z_{m,n} = \sqrt{1 - (\alpha_{m,n}^2 + \beta_{m,n}^2)} \quad (5.5)$$

To obtain non-null diffraction intensity, it is necessary that the diffraction orders generated by the curved grating overlap with the diffraction orders generated by the gratings with $\Lambda_1 = 12$ µm, which can be simplified by the following equation:

$$\beta_{1,0} = \beta_{0,n} \leftrightarrow \frac{\lambda}{\Lambda_3} cos\Psi = \frac{n\lambda}{\Lambda_1} \leftrightarrow cos\Psi = \frac{n\Lambda_3}{\Lambda_1} \quad (5.6)$$

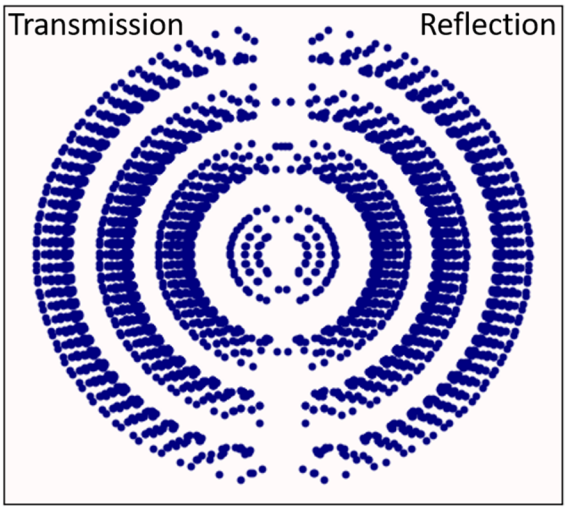

Fig. 5.8. Diffraction pattern in both transmission and reflection of the grating structures described in Fig. 5.7g.

The equation indicates a constraint, where only gratings with the orientation satisfies Equation 5.6 can produce real diffracted light. Combining equation 5.5 and 5.6, we plot the position of diffraction orders on the unit sphere and project to the screen. As shown in Fig. 5.7d-f, the structure generates nearly a half of an annular shape with the inner pipe corresponds to the grating with $\Psi = 90^0$ and the outer pipe corresponds to the grating with $\Psi = 74.3^0$ and $\Psi = 105.7^0$. Finally, we add the grating (Λ_2 = 5 μm) to mimic the defect of the sample. Here, we ignore the slight tilt of the grating and assume that it is parallel to the β-axis. The equation in direction cosine for the three superimposed gratings can be expressed as

$$\alpha_{m,n,k} = -\alpha_i + \frac{m\lambda}{\Lambda_3} sin\Psi + \frac{k\lambda}{\Lambda_2}, \beta_{m,n,k} = -\beta_i + \frac{m\lambda}{\Lambda_3} cos\Psi + \frac{n\lambda}{\Lambda_1}, z_{m,n} = \sqrt{1 - (\alpha_{m,n,k}^2 + \beta_{m,n,k}^2)} \quad (5.7)$$

with k represents diffraction orders generated by the grating with Λ_2 = 5 μm. Calculating the position of diffraction orders using equation 5.7, we project them on the unit sphere and the screen as shown in Fig. 5.7h & i. Interestingly, the presence of the defect adds multiple annulus beside the main annulus with k = 0. Note that the diffraction patterns are only presented in reflection side,

to show the complete pattern in comparison with the experiment, we also need plot the positions of diffraction orders in transmission side. It is obvious that $\alpha_{trn} = \alpha_{ref}$, $\beta_{trn} = \beta_{ref}$ for $n_{trn} = n_{ref} = n_{air}$ with trn, ref represent transmission and reflection respectively. Therefore, the diffraction orders in transmission side will be symmetry to the ones in reflection side. The full diffraction patterns for both reflection side and transmission side with the incidence angle of 35° is shown in Figure 5.8, appearing full circular diffraction pattern. It is noted that the circular diffraction patterns shown in Figure 5.8 are much thicker than the ones shown in experiment (Fig. 5.6b), attributed to the uneven distribution of nanoparticle grating curvature, where only part of the grating exhibits diffraction. To support our claim, we compare the diffraction pattern

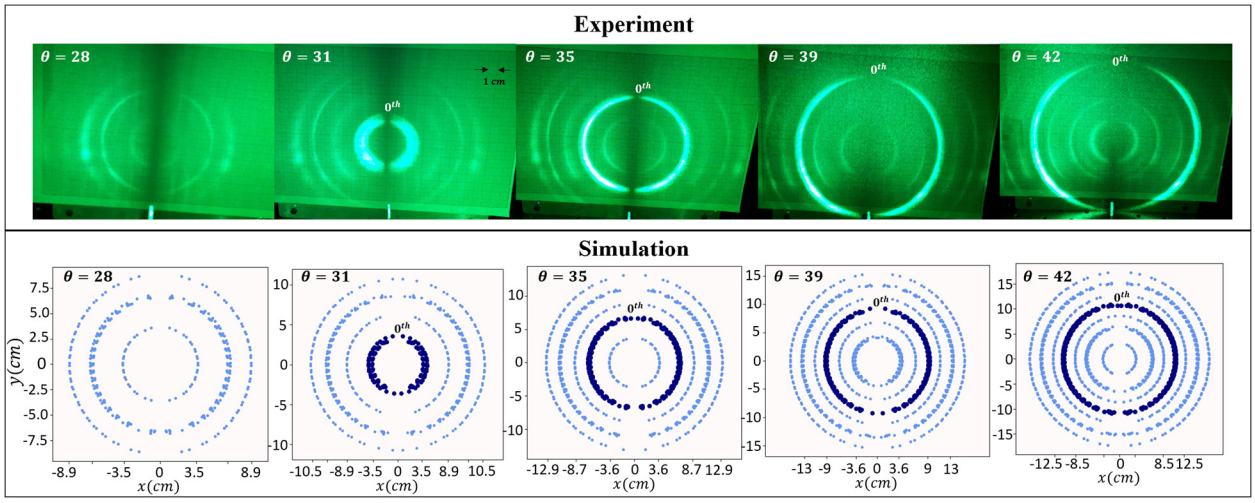

Fig. 5.9. Comparison between experiment (first row) and simulation (second row) of the far field diffraction pattern at the varying incidence angle with the experimental set up as described in Fig. 5.6b.

produced by the sample under the varying incidence angles as shown in Figure 5.9. Simulations are carried out using Equation 5.7 with the discrete values of Ψ ($83.7 \leq \psi \leq 95.7$, $74.3 \leq \psi \leq 75.3$, $104.7 \leq \psi \leq 105.7$), implying that the nanoparticle array is not uniform and the diffraction effect generated by the gratings is only accounted at the middle and the edge areas of the NPs curved lines. The 0^{th} diffraction patterns are highlighted upon $k = 0$ and $83.7 \leq \psi \leq 95.7$ (middle area of NPs grating). Comparing the experiment and simulation, one can clearly see a good agreement in the evolution of the diffraction pattern as a function of incidence angle, proving the combination diffraction effect of the three superimposed gratings in generating the unique patterns.

Interestingly, increasing laser scan speed totally rule out the circular diffraction pattern, attributed to the disappearing of the curved self-organization of nanoparticle array as shown in Fig. 5.10 & 5.11.

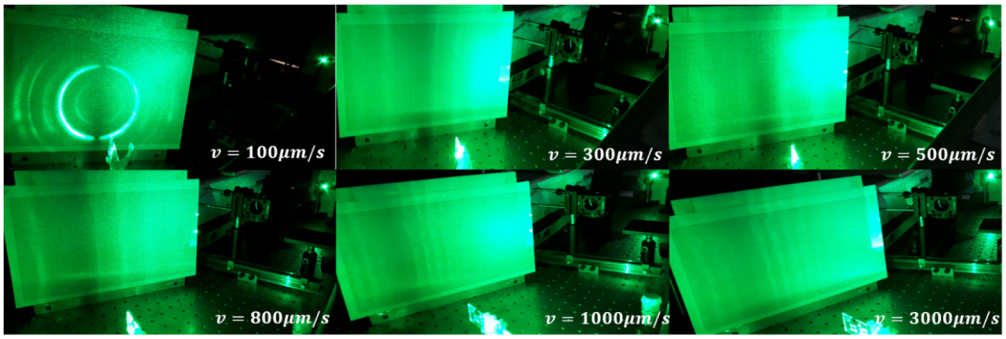

Fig. 5.10. Experimental results of the diffraction property of the samples inscribed at different scan speed (v) illuminated by and incidence with $\lambda = 514.5nm$ and $\theta = 35^0$. Only sample with the speed of 100 μm/s shows the unique circular diffractions.

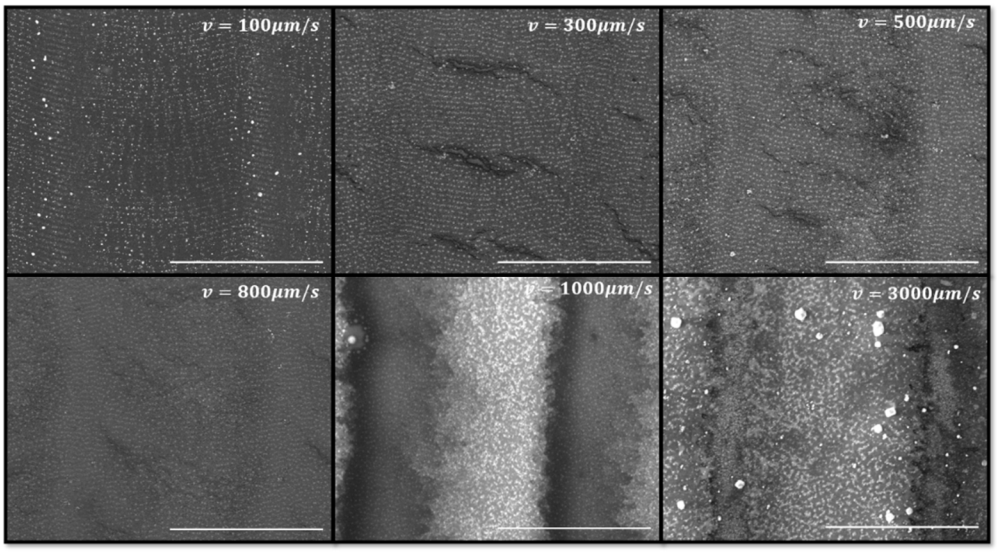

Fig. 5.11. SEM pictures of the samples inscribed by laser with different laser scanning speed (v). A periodic NPs grating curve is shown in the sample with v=100 μm which is absent in other samples. The scale bar is 10 μm.

5.6 Conclusion

This chapter studies the diffraction properties of three superimposed grating induced by laser process, including laser drawing lines, self-organized defect and self-organized nanoparticle grating. At normal incidence, the sample exhibits asymmetric diffraction patterns, resulting from the diffraction effect of laser drawing lines and the defect, where the tilt of the defect plays an important role on determining the asymmetry. In addition, under oblique incidence angle, a series of circular diffraction patterns are captured at a screen oriented perpendicular to the incidence plane and the sample. Simulations are carried out using grating equations for three gratings written in direction cosine space to reveal the combination diffraction effect of the three superimposed gratings in generating the circular diffraction patterns. These interesting diffraction properties of the laser-empowered nanostructures can find applications in display technology or security.

6 Summary and Future Perspective

6.1 Summary

Motived by the long-standing questions related to different dichroism, diffraction and color properties of laser-induced plasmonic nanomaterials, this thesis integrates comprehensive material characterizations, experiments and electromagnetic simulations to elucidate the unanswered questions and provide a deeper understanding on the underlying physics of the nanomaterial optical behaviors. The investigations are conducted on the silver titania nanocomposites processed by cw and ns lasers. In general, origins of different structural color properties are revealed and many of the optical effects are, in fact, used in industrial applications for new security or vision functionalities. Considering the wide range of the opto-structural properties of the material produced by cw and ns laser, the thesis is organized into chapters with the brief descriptions and the main results are concluded as below.

In the first chapter, the general properties of LSPR, collective plasmonic resonances and the simulation method using the expansion of T-matrix method to solve the multiple scattering problem are introduced. Following the theoretical background in chapter 1, chapter 2 presents the experimental techniques used to produce the samples, consisting of solgel-based sample preparation, laser printing set-up using continuous laser and nanosecond laser and characterization of resulting colors.

In Chapter 3, we comprehensively examine and analyze the impact of intrinsic spatial disorder and size dispersion on the optical properties of laser-induced self-organized plasmonic metasurfaces. The investigation encompasses an array of simulations conducted on regular structures, incorporating different array sizes, levels of disorder and size distributions. Furthermore, characterizations of actual sample, including SEM, TEM and Raman analysis, are also carried out to construct the real-like sample. The simulation results of the real-like sample are proved to be sufficient in reproducing the optical statistical properties of the real sample. By further investigating the near-field distribution of the sample at normal and inclined incidences, the dichroism is revealed as the result from the coupling between the dipolar mode of LSPR of

individual metallic particle and the supported guided mode excitation. These farfield and near-field investigations show that the sample inhomogeneities arising from the fabrication technique do not significantly disrupt the overall optical properties. This conclusion is further validated through the study of the different laser-induced nanostructures, exhibiting varying periods, size distribution and dichroism.

In chapter 4, we focus on the optical properties of metasurfaces induced by nanosecond laser. A wide range of different diffractive, dichroic properties and color responses are generated, which result from two main features: regular organization of metallic nanoparticles and periodic surface modulations. The morphological profiles of the samples are characterized by scanning electron microscopy and atomic force microscopy, underlying laser parameter range that produces metasurfaces exhibit diffraction, dichroism or both phenomena simultaneously. We also emphasize the significance of opto-structural parameters of the self-organized nanoparticles array in contributing to the coherent scattering intensity or diffractive efficiency. In addition, electromagnetic simulations enable us to unravel the role of near-field and far field coupling of the metallic nanoparticle array in inducing sample dichroism. Finally, different laser-empowered plasmonic images are produced, which can be visible in different observation modes, to highlight the promising of the approach in manufacturing optical devices for security or vision applications.

In chapter 5, the diffraction properties of three superimposed grating structures induced by continuous laser are investigated. Specifically, the investigated gratings consist of laser drawing lines, self-organized defects and self-organized nanoparticle gratings. At normal incidence, the sample displays asymmetric diffraction patterns, arising from the diffraction effects of the laser drawing lines and the defects, where the tilt of the defect plays an important role in determine the asymmetry. Most interestingly, when illuminated by an oblique incidence angles, sample exhibits series of circular diffraction patterns captured on a screen, which is perpendicular to both the incidence plane and the sample. The simulations, employing grating equations for the three gratings written in direction cosine space, elucidate the combination diffraction effects of the three gratings in generating the patterns.

6.2 Future Perspective

The works presented in the thesis have contributed significantly to enhance our understanding of the comprehensive optical properties of laser-induced plasmonic metasurfaces. Nevertheless, given the broad spectrum of optical properties that can exhibit from these materials, there remains room for further explorations and investigations. In particular, the works can be extended by delve deeper into refractive color behaviors, focusing on the asymmetric color responses of materials induced by cw laser versus ns laser as shown in Figure 6.1. The intriguing question of why samples induced by cw laser exhibit a larger color range on the front side compared to the back side reflection, while the behavior is entirely reversed in the case of ns laser, presents a great area for further study. My assumption is that the opto-geometrical parameters, including film compositions, film thickness, nanoparticle size and the position of the particle relative to the layers of samples, undergo different modifications under cw vs ns which subsequently induce different color responses. It could be interesting to compare the simulations results of the color responses when systematically varying one parameter at a time for both samples produced by cw and ns laser. Such investigation would enable us to draw conclusive insights into which specific parameter governs the observed properties.

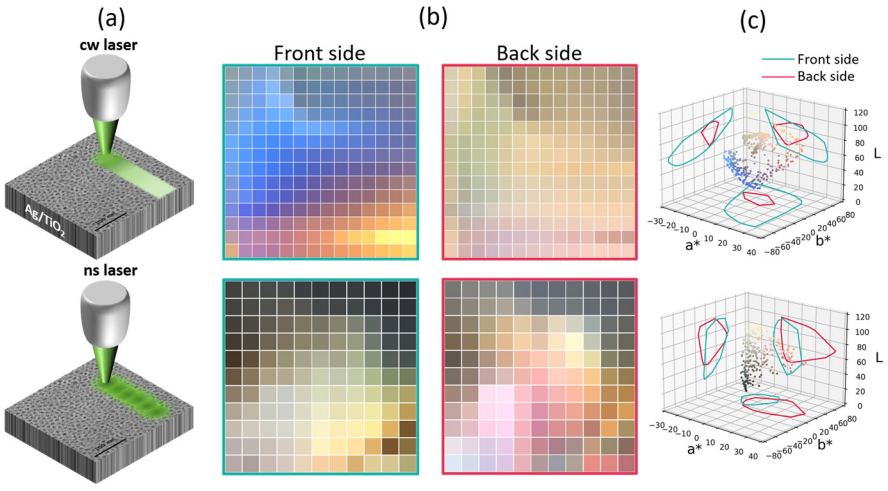

Fig. 6.1. Asymmetric color behavior of samples induced by cw laser vs ns laser. (a) Illustration of cw and ns laser processing. (b) Reflective color of front side (green outline) and back side (red outline) for samples induced by cw and ns lasers at different processing parameters. (c) The reflective colors represented in La*b* color space and their projections.

7 Annex

7.1 Average Standard Deviation

The standard deviation at each wavelength (λ) reads:

$$\sigma_\lambda = \sqrt{\frac{1}{N}\sum_{i=1}^{N=10}(Q_{i,\lambda} - \mu_\lambda)} \tag{7.1}$$

with $N = 10$ the number of simulations, $Q_{i,\lambda}$ the extinction efficiency at wavelength λ of the simulation number i and $\mu_\lambda = \frac{1}{N}\sum_{i=1}^{N=10} Q_{i,\lambda}$ is the average extinction efficiency at wavelength λ. The average relative standard deviation is then

$$\sigma = \frac{1}{N_\lambda}\sum_{\lambda=350}^{750}\frac{\sigma_\lambda}{\mu_\lambda} \tag{7.2}$$

with N_λ is the number of wavelength values.

7.2 Guided Mode Calculation

The calculation is carried out using the method proposed by C. Amra *et al.*[158] A two-layer system, similar to the one shown in figure 1 or figure 5d, but without nanoparticles is considered. n_0, n_1, n_2, n_s are the refractive indices of the superstrate, TiO_2 layer, intermediate layer and substrate. e_1 and e_2 are the thicknesses of the two layers respectively. As demonstrated by Amra et al., the poles of the complex reflection coefficient correspond to guided modes of the structure. The complex reflection coefficient is defined as: $r_0 = \frac{\tilde{n}_0 - Y_0}{\tilde{n}_0 + Y_0}$

Where $\tilde{n}_0 = \begin{cases} \frac{1}{\eta_0 \mu_{r_0}} n_0 cos\theta_0 \ (TE) \\ \frac{1}{\eta_0 \mu_{r_0}} n_0 / cos\theta_0 \ (TM) \end{cases}$ is the effective refractive index of the superstrate, θ_0 is the incidence angle, η_0 is the impedance of vacuum, μ_{r_0} is the superstrate relative permeability and Y_0 is the complex admittance at the first interface of the multilayer, which is defined as the ratio of tangential components of the electric and magnetic fields. For a multilayer system the complex admittance can be seen as the effective refractive index in a homogeneous medium. To calculate Y_0, we can apply the recursive relation:

$$Y_{j-1} = \frac{Y_j cos(\alpha_j e_j) - i\tilde{n}_j sin(\alpha_j e_j)}{cos(\alpha_j e_j) - i\left(\frac{Y_j}{\tilde{n}_j}\right) sin(\alpha_j e_j)} \tag{7.3}$$

where the subscript j represents the parameter at layer j and $\alpha_j = \sqrt{\left(\frac{2\pi n_j}{\lambda}\right)^2 - (2\pi\nu)^2}$ with $\nu = n_0 sin\theta_0/\lambda$. The equation allows us the calculate the admittance of interface $j-1$, given that the admittance of interface j is known. The admittance at substrate is simply equal to the effective refractive index: $Y_s = \tilde{n}_s$.

Having Y_0 enables us to find ν in which $\frac{1}{r(\nu)} = \frac{\tilde{n}_0(\nu)+Y_0(\nu)}{\tilde{n}_0(\nu)-Y_0(\nu)} = 0$. Finally, the effective refractive index can be calculated as $n_e = \nu\lambda$.

7.3 Silver particle refractive index

Silver permittivity obtained from modified Drude model:

$$\epsilon(\omega) = \epsilon_{\text{ib}} - \frac{\omega_p^2 \epsilon_0}{\omega^2 + j\omega\Gamma} \tag{7.4}$$

where $\epsilon_{ib} = 3.7\epsilon_0$ is the contribution of interband transition and ϵ_0 is the vacuum permittivity, ω_p is the frequency of plasma resonance with $\hbar\omega_p = 8.89\, eV$, $\Gamma = \Gamma_0 + Av_F/r$ is the damping constant with $\Gamma_0 = 17.6$ meV the damping constant of bulk silver, $A = 1$ a constant, $v_f = 1.39\, x\, 10^6$ m/s the Fermi velocity and r the particle radius.

7.4 Duplicated structures

For all the simulations in Chapter 4, the nanoparticle arrays are reproduced from the nanoparticle distribution of the real sample and then the obtained area is duplicated four times. The duplicated samples are constructed from the obtained area with the width and height are w_y, h_x and the coordinate in xy plane is x_0, y_0, and its three copies with the same size and the coordinates are: $x_1 = x_0 + h_x + a$, $y_1 = y_0$; $x_2 = x_0$, $y_2 = y_0 + w_y + b$; $x_3 = x_0 + h_x + a$, $y_3 = y_0 + w_y + b$, with a = 300 (nm), b = 100 (nm) for the simulations in Figure 4.5 & 4.7-9 and a = 325 (nm), b = 100 (nm) for the simulations in Figure 4.13.

8 References

(1) Kinoshita, S.; Yoshioka, S.; Miyazaki, J. Physics of Structural Colors. *Rep. Prog. Phys.* **2008**, *71* (7), 076401. https://doi.org/10.1088/0034-4885/71/7/076401.

(2) Kristensen, A.; Yang, J. K. W.; Bozhevolnyi, S. I.; Link, S.; Nordlander, P.; Halas, N. J.; Mortensen, N. A. Plasmonic Colour Generation. *Nat. Rev. Mater.* **2017**, *2* (1), 16088. https://doi.org/10.1038/natrevmats.2016.88.

(3) Daqiqeh Rezaei, S.; Dong, Z.; You En Chan, J.; Trisno, J.; Ng, R. J. H.; Ruan, Q.; Qiu, C.-W.; Mortensen, N. A.; Yang, J. K. W. Nanophotonic Structural Colors. *ACS Photonics* **2021**, *8* (1), 18–33. https://doi.org/10.1021/acsphotonics.0c00947.

(4) Dumanli, A. G.; Savin, T. Recent Advances in the Biomimicry of Structural Colours. *Chem. Soc. Rev.* **2016**, *45* (24), 6698–6724. https://doi.org/10.1039/C6CS00129G.

(5) Keshavarz Hedayati, M.; Elbahri, M. Review of Metasurface Plasmonic Structural Color. *Plasmonics* **2017**, *12* (5), 1463–1479. https://doi.org/10.1007/s11468-016-0407-y.

(6) Sun, J.; Bhushan, B.; Tong, J. Structural Coloration in Nature. *RSC Adv.* **2013**, *3* (35), 14862. https://doi.org/10.1039/c3ra41096j.

(7) Kinoshita, S.; Yoshioka, S. Structural Colors in Nature: The Role of Regularity and Irregularity in the Structure. *ChemPhysChem* **2005**, *6* (8), 1442–1459. https://doi.org/10.1002/cphc.200500007.

(8) Xiong, K.; Tordera, D.; Jonsson, M. P.; Dahlin, A. B. Active Control of Plasmonic Colors: Emerging Display Technologies. *Rep. Prog. Phys.* **2019**, *82* (2), 024501. https://doi.org/10.1088/1361-6633/aaf844.

(9) Tanabe, I.; Tatsuma, T. Plasmonic Manipulation of Color and Morphology of Single Silver Nanospheres. *Nano Lett.* **2012**, *12* (10), 5418–5421. https://doi.org/10.1021/nl302919n.

(10) Neubrech, F.; Duan, X.; Liu, N. Dynamic Plasmonic Color Generation Enabled by Functional Materials. *Sci. Adv.* **2020**, *6* (36), eabc2709. https://doi.org/10.1126/sciadv.abc2709.

(11) Gu, Y.; Zhang, L.; Yang, J. K. W.; Yeo, S. P.; Qiu, C.-W. Color Generation *via* Subwavelength Plasmonic Nanostructures. *Nanoscale* **2015**, *7* (15), 6409–6419. https://doi.org/10.1039/C5NR00578G.

(12) Fu, Y.; Tippets, C. A.; Donev, E. U.; Lopez, R. Structural Colors: From Natural to Artificial Systems. *WIREs Nanomedicine Nanobiotechnology* **2016**, *8* (5), 758–775. https://doi.org/10.1002/wnan.1396.

(13) Song, M.; Wang, D.; Peana, S.; Choudhury, S.; Nyga, P.; Kudyshev, Z. A.; Yu, H.; Boltasseva, A.; Shalaev, V. M.; Kildishev, A. V. Colors with Plasmonic Nanostructures: A Full-Spectrum Review. *Appl. Phys. Rev.* **2019**, *6* (4), 041308. https://doi.org/10.1063/1.5110051.

(14) Garcia, M. A. Surface Plasmons in Metallic Nanoparticles: Fundamentals and Applications. *J. Phys. Appl. Phys.* **2012**, *45* (38), 389501. https://doi.org/10.1088/0022-3727/45/38/389501.

(15) Jiang, N.; Zhuo, X.; Wang, J. Active Plasmonics: Principles, Structures, and Applications. *Chem. Rev.* **2018**, *118* (6), 3054–3099. https://doi.org/10.1021/acs.chemrev.7b00252.

(16) Kelly, K. L.; Coronado, E.; Zhao, L. L.; Schatz, G. C. The Optical Properties of Metal Nanoparticles: The Influence of Size, Shape, and Dielectric Environment. *J. Phys. Chem. B* **2003**, *107* (3), 668–677. https://doi.org/10.1021/jp026731y.

(17) Mayer, K. M.; Hafner, J. H. Localized Surface Plasmon Resonance Sensors. *Chem. Rev.* **2011**, *111* (6), 3828–3857. https://doi.org/10.1021/cr100313v.

(18) Petryayeva, E.; Krull, U. J. Localized Surface Plasmon Resonance: Nanostructures, Bioassays and Biosensing—A Review. *Anal. Chim. Acta* **2011**, *706* (1), 8–24. https://doi.org/10.1016/j.aca.2011.08.020.

(19) Murray, W. A.; Barnes, W. L. Plasmonic Materials. *Adv. Mater.* **2007**, *19* (22), 3771–3782. https://doi.org/10.1002/adma.200700678.

(20) Kumar, K.; Duan, H.; Hegde, R. S.; Koh, S. C. W.; Wei, J. N.; Yang, J. K. W. Printing Colour at the Optical Diffraction Limit. *Nat. Nanotechnol.* **2012**, *7* (9), 557–561. https://doi.org/10.1038/nnano.2012.128.

(21) Roberts, A. S.; Pors, A.; Albrektsen, O.; Bozhevolnyi, S. I. Subwavelength Plasmonic Color Printing Protected for Ambient Use. *Nano Lett.* **2014**, *14* (2), 783–787. https://doi.org/10.1021/nl404129n.

(22) Kravets, V. G.; Kabashin, A. V.; Barnes, W. L.; Grigorenko, A. N. Plasmonic Surface Lattice Resonances: A Review of Properties and Applications. *Chem. Rev.* **2018**, *118* (12), 5912–5951. https://doi.org/10.1021/acs.chemrev.8b00243.

(23) Utyushev, A. D.; Zakomirnyi, V. I.; Rasskazov, I. L. Collective Lattice Resonances: Plasmonics and Beyond. *Rev. Phys.* **2021**, *6*, 100051. https://doi.org/10.1016/j.revip.2021.100051.

(24) Choi, D.; Shin, C. K.; Yoon, D.; Chung, D. S.; Jin, Y. W.; Lee, L. P. Plasmonic Optical Interference. *Nano Lett.* **2014**, *14* (6), 3374–3381. https://doi.org/10.1021/nl5008823.

(25) Yakovlev, A. V.; Milichko, V. A.; Vinogradov, V. V.; Vinogradov, A. V. Inkjet Color Printing by Interference Nanostructures. *ACS Nano* **2016**, *10* (3), 3078–3086. https://doi.org/10.1021/acsnano.5b06074.

(26) Li, K.; Wang, J.; Cai, W.; He, H.; Liu, J.; Yin, Z.; Luo, D.; Mu, Q.; Gérard, D.; Liu, Y. J. Electrically Switchable Structural Colors Based on Liquid-Crystal-Overlaid Aluminum Anisotropic Nanoaperture Arrays. *Opt. Express* **2022**, *30* (18), 31913. https://doi.org/10.1364/OE.461887.

(27) Vynck, K.; Pacanowski, R.; Agreda, A.; Dufay, A.; Granier, X.; Lalanne, P. The Visual Appearances of Disordered Optical Metasurfaces. *Nat. Mater.* **2022**, *21*, 1035–1041. https://doi.org/10.1038/s41563-022-01255-9.

(28) Hsu, C. W.; Zhen, B.; Qiu, W.; Shapira, O.; DeLacy, B. G.; Joannopoulos, J. D.; Soljačić, M. Transparent Displays Enabled by Resonant Nanoparticle Scattering. *Nat. Commun.* **2014**, *5* (1), 3152. https://doi.org/10.1038/ncomms4152.

(29) Song, M.; Kudyshev, Z. A.; Yu, H.; Boltasseva, A.; Shalaev, V. M.; Kildishev, A. V. Achieving Full-Color Generation with Polarization-Tunable Perfect Light Absorption. *Opt. Mater. Express* **2019**, *9* (2), 779. https://doi.org/10.1364/OME.9.000779.

(30) Nishi, H.; Tatsuma, T. Full-Color Scattering Based on Plasmon and Mie Resonances of Gold Nanoparticles Modulated by Fabry–Pérot Interference for Coloring and Image Projection. *ACS Appl. Nano Mater.* **2019**, *2* (8), 5071–5078. https://doi.org/10.1021/acsanm.9b00990.

(31) Wu, B.; Liu, Z.; Liu, X.; Liu, G.; Tang, P.; Yuan, W.; Fu, G. Large-Scale Reflective Optical Janus Color Materials. *Nanotechnology* **2020**, *31* (22), 225301. https://doi.org/10.1088/1361-6528/ab7649.

(32) Chen, J.; Wang, Z.; Liu, C.; Chen, Z.; Tang, X.; Wu, Q.; Zhang, S.; Song, G.; Cong, S.; Chen, Q.; Zhao, Z. Mimicking Nature's Butterflies: Electrochromic Devices with Dual-Sided Differential Colorations. *Adv. Mater.* **2021**, *33* (14), 2007314. https://doi.org/10.1002/adma.202007314.

(33) England, G. T.; Russell, C.; Shirman, E.; Kay, T.; Vogel, N.; Aizenberg, J. The Optical Janus Effect: Asymmetric Structural Color Reflection Materials. *Adv. Mater.* **2017**, *29* (29), 1606876. https://doi.org/10.1002/adma.201606876.

(34) Kim, T.; Yu, E.-S.; Bae, Y.-G.; Lee, J.; Kim, I. S.; Chung, S.; Lee, S.-Y.; Ryu, Y.-S. Asymmetric Optical Camouflage: Tuneable Reflective Colour Accompanied by the Optical Janus Effect. *Light Sci. Appl.* **2020**, *9* (1), 175. https://doi.org/10.1038/s41377-020-00413-5.

(35) Heydari, E.; Sperling, J. R.; Neale, S. L.; Clark, A. W. Plasmonic Color Filters as Dual-State Nanopixels for High-Density Microimage Encoding. *Adv. Funct. Mater.* **2017**, *27* (35), 1701866. https://doi.org/10.1002/adfm.201701866.

(36) Li, Z.; Clark, A. W.; Cooper, J. M. Dual Color Plasmonic Pixels Create a Polarization Controlled Nano Color Palette. *ACS Nano* **2016**, *10* (1), 492–498. https://doi.org/10.1021/acsnano.5b05411.

(37) Destouches, N.; Sharma, N.; Vangheluwe, M.; Dalloz, N.; Vocanson, F.; Bugnet, M.; Hébert, M.; Siegel, J. Laser-Empowered Random Metasurfaces for White Light Printed Image Multiplexing. *Adv. Funct. Mater.* **2021**, *31* (18), 2010430. https://doi.org/10.1002/adfm.202010430.

(38) Dalloz, N.; Le, V. D.; Hebert, M.; Eles, B.; Flores Figueroa, M. A.; Hubert, C.; Ma, H.; Sharma, N.; Vocanson, F.; Ayala, S.; Destouches, N. Anti-Counterfeiting White Light Printed Image Multiplexing by Fast Nanosecond Laser Processing. *Adv. Mater.* **2022**, *34* (2), 2104054. https://doi.org/10.1002/adma.202104054.

(39) Guay, J.-M.; Calà Lesina, A.; Côté, G.; Charron, M.; Poitras, D.; Ramunno, L.; Berini, P.; Weck, A. Laser-Induced Plasmonic Colours on Metals. *Nat. Commun.* **2017**, *8* (1), 16095. https://doi.org/10.1038/ncomms16095.

(40) Zhu, X.; Engelberg, J.; Remennik, S.; Zhou, B.; Pedersen, J. N.; Uhd Jepsen, P.; Levy, U.; Kristensen, A. Resonant Laser Printing of Optical Metasurfaces. *Nano Lett.* **2022**, *22*, 2786–2792. https://doi.org/10.1021/acs.nanolett.1c04874.

(41) Veiko, V. P.; Andreeva, Y.; Van Cuong, L.; Lutoshina, D.; Polyakov, D.; Sinev, D.; Mikhailovskii, V.; Kolobov, Y. R.; Odintsova, G. Laser Paintbrush as a Tool for Modern Art. *Optica* **2021**, *8* (5), 577. https://doi.org/10.1364/OPTICA.420074.

(42) Zhang, Y.; Zhang, Q.; Ouyang, X.; Lei, D. Y.; Zhang, A. P.; Tam, H.-Y. Ultrafast Light-Controlled Growth of Silver Nanoparticles for Direct Plasmonic Color Printing. *ACS Nano* **2018**, *12* (10), 9913–9921. https://doi.org/10.1021/acsnano.8b02868.

(43) Hwang, J. S.; Arthanari, S.; Ko, P.; Jung, K.; Park, J.-E.; Youn, H.; Yang, M.; Kim, S.-W.; Lee, H.; Kim, Y.-J. Plasmonic Color Printing via Bottom-Up Laser-Induced Photomodification Process. *ACS Appl. Mater. Interfaces* **2022**, *14* (26), 30315–30323. https://doi.org/10.1021/acsami.2c04217.

(44) Roberts, A. S.; Novikov, S. M.; Yang, Y.; Chen, Y.; Boroviks, S.; Beermann, J.; Mortensen, N. A.; Bozhevolnyi, S. I. Laser Writing of Bright Colors on Near-Percolation Plasmonic Reflector Arrays. *ACS Nano* **2019**, *13* (1), 71–77. https://doi.org/10.1021/acsnano.8b07541.

(45) Florian, C.; Kirner, S. V.; Krüger, J.; Bonse, J. Surface Functionalization by Laser-Induced Periodic Surface Structures. *J. Laser Appl.* **2020**, *32* (2), 022063. https://doi.org/10.2351/7.0000103.

(46) Bonse, J.; Hohm, S.; Kirner, S. V.; Rosenfeld, A.; Kruger, J. Laser-Induced Periodic Surface Structures— A Scientific Evergreen. *IEEE J. Sel. Top. QUANTUM Electron.* **2017**, *23* (3), 15. https://doi.org/doi.org/10.1109/JSTQE.2016.2614183.

(47) Destouches, N.; Crespo-Monteiro, N.; Vitrant, G.; Lefkir, Y.; Reynaud, S.; Epicier, T.; Liu, Y.; Vocanson, F.; Pigeon, F. Self-Organized Growth of Metallic Nanoparticles in a Thin Film under Homogeneous and Continuous-Wave Light Excitation. *J Mater Chem C* **2014**, *2* (31), 6256–6263. https://doi.org/10.1039/C4TC00971A.

(48) Sharma, N.; Vangheluwe, M.; Vocanson, F.; Cazier, A.; Bugnet, M.; Reynaud, S.; Vermeulin, A.; Destouches, N. Laser-Driven Plasmonic Gratings for Hiding Multiple Images. *Mater. Horiz.* **2019**, *6* (5), 978–983. https://doi.org/10.1039/C9MH00017H.

(49) Liu, Z.; Destouches, N.; Vitrant, G.; Lefkir, Y.; Epicier, T.; Vocanson, F.; Bakhti, S.; Fang, Y.; Bandyopadhyay, B.; Ahmed, M. Understanding the Growth Mechanisms of Ag Nanoparticles Controlled by Plasmon-Induced Charge Transfers in Ag-TiO_2 Films. *J. Phys. Chem. C* **2015**, *119* (17), 9496–9505. https://doi.org/10.1021/acs.jpcc.5b01350.

(50) Ma, H.; Bakhti, S.; Rudenko, A.; Vocanson, F.; Slaughter, D. S.; Destouches, N.; Itina, T. E. Laser-Generated Ag Nanoparticles in Mesoporous TiO_2 Films: Formation Processes and Modeling-Based Size Prediction. *J. Phys. Chem. C* **2019**, *123* (42), 25898–25907. https://doi.org/10.1021/acs.jpcc.9b05561.

(51) Eles, B.; Rouquette, P.; Siegel, J.; Amra, C.; Lumeau, J.; Moreau, A.; Hubert, C.; Zerrad, M.; Destouches, N. Mechanisms Driving Self-Organization Phenomena in Random Plasmonic

Metasurfaces under Multipulse Femtosecond Laser Exposure: A Multitime Scale Study. *Nanophotonics* **2022**, *11* (10), 2303–2318. https://doi.org/10.1515/nanoph-2022-0023.

(52) Liu, Z.; Siegel, J.; Garcia-Lechuga, M.; Epicier, T.; Lefkir, Y.; Reynaud, S.; Bugnet, M.; Vocanson, F.; Solis, J.; Vitrant, G.; Destouches, N. Three-Dimensional Self-Organization in Nanocomposite Layered Systems by Ultrafast Laser Pulses. *ACS Nano* **2017**, *11* (5), 5031–5040. https://doi.org/10.1021/acsnano.7b01748.

(53) Sharma, N.; Destouches, N.; Florian, C.; Serna, R.; Siegel, J. Tailoring Metal-Dielectric Nanocomposite Materials with Ultrashort Laser Pulses for Dichroic Color Control. *Nanoscale* **2019**, *11* (40), 18779–18789. https://doi.org/10.1039/C9NR06763A.

(54) Ma, H.; Dalloz, N.; Habrard, A.; Sebban, M.; Sterl, F.; Giessen, H.; Hebert, M.; Destouches, N. Predicting Laser-Induced Colors of Random Plasmonic Metasurfaces and Optimizing Image Multiplexing Using Deep Learning. *ACS Nano* **2022**, *16* (6), 9410–9419. https://doi.org/10.1021/acsnano.2c02235.

(55) Miyata, M.; Hatada, H.; Takahara, J. Full-Color Subwavelength Printing with Gap-Plasmonic Optical Antennas. *Nano Lett.* **2016**, *16* (5), 3166–3172. https://doi.org/10.1021/acs.nanolett.6b00500.

(56) Chowdhury, S. N.; Nyga, P.; Kudyshev, Z. A.; Garcia Bravo, E.; Lagutchev, A. S.; Kildishev, A. V.; Shalaev, V. M.; Boltasseva, A. Lithography-Free Plasmonic Color Printing with Femtosecond Laser on Semicontinuous Silver Films. *ACS Photonics* **2020**, *8* (2), 521–530. https://doi.org/10.1021/acsphotonics.0c01506.

(57) Baffou, G.; Quidant, R. Nanoplasmonics for Chemistry. *Chem. Soc. Rev.* **2014**, *43* (11), 3898. https://doi.org/10.1039/c3cs60364d.

(58) Boriskina, S. V.; Ghasemi, H.; Chen, G. Plasmonic Materials for Energy: From Physics to Applications. *Mater. Today* **2013**, *16* (10), 375–386. https://doi.org/10.1016/j.mattod.2013.09.003.

(59) Drude, P. Zur Elektronentheorie der Metalle. *Ann. Phys.* **1900**, *306* (3), 566–613. https://doi.org/10.1002/andp.19003060312.

(60) Ashcroft, N.; Mermin, N. D. *Solid State Physics*.

(61) *Optical Properties of Solids*; Elsevier, 1972. https://doi.org/10.1016/C2013-0-07656-6.

(62) Ehrenreich, H.; Philipp, H. R. Optical Properties of Ag and Cu. *Phys. Rev.* **1962**, *128* (4), 1622–1629. https://doi.org/10.1103/PhysRev.128.1622.

(63) Bohren, C. F.; Huffman, D. R. *Absorption and Scattering of Light by Small Particles*; Wiley: New York, 1983.

(64) Kreibig, U.; Vollmer, M. *Optical Properties of Metal Clusters*; Toennies, J. P., Gonser, U., Osgood, R. M., Panish, M. B., Sakaki, H., Lotsch, H. K. V., Series Eds.; Springer Series in Materials Science; Springer Berlin Heidelberg: Berlin, Heidelberg, 1995; Vol. 25. https://doi.org/10.1007/978-3-662-09109-8.

(65) Kreibig, U.; Vollmer, M. *OPTICAL ABSORPTION OF SMALL METALLIC PARTICLES*; Springer.

(66) Maier, S. A. *Plasmonics: Fundamentals and Applications*; Springer US: New York, NY, 2007. https://doi.org/10.1007/0-387-37825-1.

(67) Mie, G. Beiträge zur Optik trüber Medien, speziell kolloidaler Metallösungen. *Ann. Phys.* **1908**, *330* (3), 377–445. https://doi.org/10.1002/andp.19083300302.

(68) Coronado, E. A.; Encina, E. R.; Stefani, F. D. Optical Properties of Metallic Nanoparticles: Manipulating Light, Heat and Forces at the Nanoscale. *Nanoscale* **2011**, *3* (10), 4042. https://doi.org/10.1039/c1nr10788g.

(69) Egel, A. Accurate Optical Simulation of Disordered Scattering Layers for Light Extraction from Organic Light Emitting Diodes, Karlsruhe Institute of Technology (KIT), Karlsruhe, Germany, 2018.

(70) Mackowski, D. The Extension of Mie Theory to Multiple Spheres. In *The Mie Theory*; Hergert, W., Wriedt, T., Eds.; Springer Series in Optical Sciences; Springer Berlin Heidelberg: Berlin, Heidelberg, 2012; Vol. 169, pp 223–256. https://doi.org/10.1007/978-3-642-28738-1_8.

(71) Doicu, A.; Wriedt, T.; Eremin, Y. *Light Scattering by Systems of Particles: Null-Field Method with Discrete Sources: Theory and Programs*; Springer series in optical sciences; Springer: Berlin ; New York, 2006.

(72) Egel, A.; Czajkowski, K. M.; Theobald, D.; Ladutenko, K.; Kuznetsov, A. S.; Pattelli, L. SMUTHI: A Python Package for the Simulation of Light Scattering by Multiple Particles near or between Planar Interfaces. *J. Quant. Spectrosc. Radiat. Transf.* **2021**, *273*, 107846. https://doi.org/10.1016/j.jqsrt.2021.107846.

(73) Cruzan, O. R. TRANSLATIONALADDITION THEOREMS FOR SPHERICAL VECTOR WAVE FUNCTIONS. No. 1, 8.

(74) Boström, A., Kristensson, G., & Ström, S. Transformation Properties of Plane, Spherical and Cylindrical Scalar and Vector Wave Functions. In *In V. V. Varadan, A. Lakhtakia, & V. K. Varadan (Eds.), Acoustic, Electromagnetic and Elastic Wave Scattering, Field Representations and Introduction to Scattering*; Elsevier, 1991; Vol. Vol. 1, pp 165–210.

(75) Born, M. Electromagnetic Theory of Propagation, Interference and Diffraction of Light.

(76) Ko, D. Y. K.; Sambles, J. R. Scattering Matrix Method for Propagation of Radiation in Stratified Media: Attenuated Total Reflection Studies of Liquid Crystals. *J. Opt. Soc. Am. A* **1988**, *5* (11), 1863. https://doi.org/10.1364/JOSAA.5.001863.

(77) Bay, M.; Vignolini, S.; Vynck, K. PyLlama – Python Toolkit for the Electromagnetic Modelling of Multilayered Anisotropic Media. *Comput. Phys. Commun.* **2022**, *273*, 108256.

(78) Waterman, P. C. Matrix Formulation of Electromagnetic Scattering. *Proc. IEEE* **1965**, *53* (8), 805–812. https://doi.org/10.1109/PROC.1965.4058.

(79) Mishchenko, M. I.; Zakharova, N. T.; Khlebtsov, N. G.; Videen, G.; Wriedt, T. Comprehensive Thematic T-Matrix Reference Database: A 2015–2017 Update. *J. Quant. Spectrosc. Radiat. Transf.* **2017**, *202*, 240–246. https://doi.org/10.1016/j.jqsrt.2017.08.007.

(80) Bertrand, M.; Devilez, A.; Hugonin, J.-P.; Lalanne, P.; Vynck, K. Global Polarizability Matrix Method for Efficient Modeling of Light Scattering by Dense Ensembles of Non-Spherical Particles in Stratified Media. *Journal of the Optical Society of America A*.

(81) Meier, M.; Wokaun, A. Enhanced Fields on Large Metal Particles: Dynamic Depolarization. *Opt. Lett.* **1983**, *8* (11), 581. https://doi.org/10.1364/OL.8.000581.

(82) Nordlander, P.; Oubre, C.; Prodan, E.; Li, K.; Stockman, M. I. Plasmon Hybridization in Nanoparticle Dimers. *Nano Lett.* **2004**, *4* (5), 899–903. https://doi.org/10.1021/nl049681c.

(83) Halas, N. J.; Lal, S.; Chang, W.-S.; Link, S.; Nordlander, P. Plasmons in Strongly Coupled Metallic Nanostructures. *Chem. Rev.* **2011**, *111* (6), 3913–3961. https://doi.org/10.1021/cr200061k.

(84) Cherqui, C.; Bourgeois, M. R.; Wang, D.; Schatz, G. C. Plasmonic Surface Lattice Resonances: Theory and Computation. *Acc. Chem. Res.* **2019**, *52* (9), 2548–2558. https://doi.org/10.1021/acs.accounts.9b00312.

(85) Ross, M. B.; Mirkin, C. A.; Schatz, G. C. Optical Properties of One-, Two-, and Three-Dimensional Arrays of Plasmonic Nanostructures. *J. Phys. Chem. C* **2016**, *120* (2), 816–830. https://doi.org/10.1021/acs.jpcc.5b10800.

(86) Wang, W.; Ramezani, M.; Väkeväinen, A. I.; Törmä, P.; Rivas, J. G.; Odom, T. W. The Rich Photonic World of Plasmonic Nanoparticle Arrays. *Mater. Today* **2018**, *21* (3), 303–314. https://doi.org/10.1016/j.mattod.2017.09.002.

(87) Quaranta, G.; Basset, G.; Martin, O. J. F.; Gallinet, B. Recent Advances in Resonant Waveguide Gratings. *Laser Photonics Rev.* **2018**, *12* (9), 1800017. https://doi.org/10.1002/lpor.201800017.

(88) Christ, A.; Tikhodeev, S. G.; Gippius, N. A.; Kuhl, J.; Giessen, H. Waveguide-Plasmon Polaritons: Strong Coupling of Photonic and Electronic Resonances in a Metallic Photonic Crystal Slab. *Phys. Rev. Lett.* **2003**, *91* (18), 183901. https://doi.org/10.1103/PhysRevLett.91.183901.

(89) Zentgraf, T.; Zhang, S.; Oulton, R. F.; Zhang, X. Ultranarrow Coupling-Induced Transparency Bands in Hybrid Plasmonic Systems. *Phys. Rev. B* **2009**, *80* (19), 195415. https://doi.org/10.1103/PhysRevB.80.195415.

(90) Rodriguez, S. R. K.; Schaafsma, M. C.; Berrier, A.; Gómez Rivas, J. Collective Resonances in Plasmonic Crystals: Size Matters. *Phys. B Condens. Matter* **2012**, *407* (20), 4081–4085. https://doi.org/10.1016/j.physb.2012.03.053.

(91) Rodriguez, S. R. K.; Murai, S.; Verschuuren, M. A.; Rivas, J. G. Light-Emitting Waveguide-Plasmon Polaritons. *Phys. Rev. Lett.* **2012**, *109* (16), 166803. https://doi.org/10.1103/PhysRevLett.109.166803.

(92) Murai, S.; Verschuuren, M. A.; Lozano, G.; Pirruccio, G.; Rodriguez, S. R. K.; Rivas, J. G. Hybrid Plasmonic-Photonic Modes in Diffractive Arrays of Nanoparticles Coupled to Light-Emitting Optical Waveguides. *Opt. Express* **2013**, *21* (4), 4250. https://doi.org/10.1364/OE.21.004250.

(93) Palinski, T. J.; Vyhnalek, B. E.; Hunter, G. W.; Tadimety, A.; Zhang, J. X. J. Mode Switching With Waveguide-Coupled Plasmonic Nanogratings. *IEEE J. Sel. Top. Quantum Electron.* **2021**, *27* (1), 1–10. https://doi.org/10.1109/JSTQE.2020.3019023.

(94) DeVoe, H. Optical Properties of Molecular Aggregates. I. Classical Model of Electronic Absorption and Refraction. *J. Chem. Phys.* **1964**, *41* (2), 393–400. https://doi.org/10.1063/1.1725879.

(95) DeVoe, H. Optical Properties of Molecular Aggregates. II. Classical Theory of the Refraction, Absorption, and Optical Activity of Solutions and Crystals. *J. Chem. Phys.* **1965**, *43* (9), 3199–3208. https://doi.org/10.1063/1.1697294.

(96) Laor, U.; Schatz, G. C. The Role of Surface Roughness in Surface Enhanced Raman Spectroscopy (SERS): The Importance of Multiple Plasmon Resonances. *Chem. Phys. Lett.* **1981**, *82* (3), 566–570. https://doi.org/10.1016/0009-2614(81)85442-5.

(97) Meier, M.; Liao, P. F.; Wokaun, A. Enhanced Fields on Rough Surfaces: Dipolar Interactions among Particles of Sizes Exceeding the Rayleigh Limit. *J. Opt. Soc. Am. B* **1985**, *2* (6), 931. https://doi.org/10.1364/JOSAB.2.000931.

(98) Carron, K. T.; Lehmann, H. W.; Fluhr, W.; Meier, M.; Wokaun, A. Resonances of Two-Dimensional Particle Gratings in Surface-Enhanced Raman Scattering. *J. Opt. Soc. Am. B* **1986**, *3* (3), 430. https://doi.org/10.1364/JOSAB.3.000430.

(99) Markel, V. A. Coupled-Dipole Approach to Scattering of Light from a One-Dimensional Periodic Dipole Structure. *J. Mod. Opt.* **1993**, *40* (11), 2281–2291. https://doi.org/10.1080/09500349314552291.

(100) Zou, S.; Janel, N.; Schatz, G. C. Silver Nanoparticle Array Structures That Produce Remarkably Narrow Plasmon Lineshapes. *J. Chem. Phys.* **2004**, *120* (23), 10871–10875. https://doi.org/10.1063/1.1760740.

(101) Zou, S.; Schatz, G. C. Narrow Plasmonic/Photonic Extinction and Scattering Line Shapes for One and Two Dimensional Silver Nanoparticle Arrays. *J. Chem. Phys.* **2004**, *121* (24), 12606. https://doi.org/10.1063/1.1826036.

(102) Auguié, B.; Barnes, W. L. Collective Resonances in Gold Nanoparticle Arrays. *Phys. Rev. Lett.* **2008**, *101* (14), 143902. https://doi.org/10.1103/PhysRevLett.101.143902.

(103) Humphrey, A. D.; Meinzer, N.; Starkey, T. A.; Barnes, W. L. Surface Lattice Resonances in Plasmonic Arrays of Asymmetric Disc Dimers. *ACS Photonics* **2016**, *3* (4), 634–639. https://doi.org/10.1021/acsphotonics.5b00727.

(104) Kravets, V. G.; Schedin, F.; Grigorenko, A. N. Extremely Narrow Plasmon Resonances Based on Diffraction Coupling of Localized Plasmons in Arrays of Metallic Nanoparticles. *Phys. Rev. Lett.* **2008**, *101* (8), 087403. https://doi.org/10.1103/PhysRevLett.101.087403.

(105) Chu, Y.; Schonbrun, E.; Yang, T.; Crozier, K. B. Experimental Observation of Narrow Surface Plasmon Resonances in Gold Nanoparticle Arrays. *Appl. Phys. Lett.* **2008**, *93* (18), 181108. https://doi.org/10.1063/1.3012365.

(106) García de Abajo, F. J.; Sáenz, J. J.; Campillo, I.; Dolado, J. S. Site and Lattice Resonances in Metallic Hole Arrays. *Opt. Express* **2006**, *14* (1), 7. https://doi.org/10.1364/OPEX.14.000007.

(107) Martín-Moreno, L.; García-Vidal, F. J.; Lezec, H. J.; Pellerin, K. M.; Thio, T.; Pendry, J. B.; Ebbesen, T. W. Theory of Extraordinary Optical Transmission through Subwavelength Hole Arrays. *Phys. Rev. Lett.* **2001**, *86* (6), 1114–1117. https://doi.org/10.1103/PhysRevLett.86.1114.

(108) Biswas, S.; Duan, J.; Nepal, D.; Park, K.; Pachter, R.; Vaia, R. A. Plasmon-Induced Transparency in the Visible Region via Self-Assembled Gold Nanorod Heterodimers. *Nano Lett.* **2013**, *13* (12), 6287–6291. https://doi.org/10.1021/nl403911z.

(109) Abass, A.; Rodriguez, S. R.-K.; Gómez Rivas, J.; Maes, B. Tailoring Dispersion and Eigenfield Profiles of Plasmonic Surface Lattice Resonances. *ACS Photonics* **2014**, *1* (1), 61–68. https://doi.org/10.1021/ph400072z.

(110) Le-Van, Q.; Zoethout, E.; Geluk, E.; Ramezani, M.; Berghuis, M.; Gómez Rivas, J. Enhanced Quality Factors of Surface Lattice Resonances in Plasmonic Arrays of Nanoparticles. *Adv. Opt. Mater.* **2019**, *7* (6), 1801451. https://doi.org/10.1002/adom.201801451.

(111) Porto, J. A.; García-Vidal, F. J.; Pendry, J. B. Transmission Resonances on Metallic Gratings with Very Narrow Slits. *Phys. Rev. Lett.* **1999**, *83* (14), 2845–2848. https://doi.org/10.1103/PhysRevLett.83.2845.

(112) Bendaña, X. M.; Lozano, G.; Pirruccio, G.; Gómez Rivas, J.; García de Abajo, F. J. Excitation of Confined Modes on Particle Arrays. *Opt. Express* **2013**, *21* (5), 5636. https://doi.org/10.1364/OE.21.005636.

(113) Yu, A.; Li, W.; Wang, Y.; Li, T. Surface Lattice Resonances Based on Parallel Coupling in Metal-Insulator-Metal Stacks. *Opt. Express* **2018**, *26* (16), 20695. https://doi.org/10.1364/OE.26.020695.

(114) van Beijnum, F.; van Veldhoven, P. J.; Geluk, E. J.; de Dood, M. J. A.; 't Hooft, G. W.; van Exter, M. P. Surface Plasmon Lasing Observed in Metal Hole Arrays. *Phys. Rev. Lett.* **2013**, *110* (20), 206802. https://doi.org/10.1103/PhysRevLett.110.206802.

(115) Wang, D.; Guan, J.; Hu, J.; Bourgeois, M. R.; Odom, T. W. Manipulating Light–Matter Interactions in Plasmonic Nanoparticle Lattices. *Acc. Chem. Res.* **2019**, *52* (11), 2997–3007. https://doi.org/10.1021/acs.accounts.9b00345.

(116) Hakala, T. K.; Rekola, H. T.; Väkeväinen, A. I.; Martikainen, J.-P.; Nečada, M.; Moilanen, A. J.; Törmä, P. Lasing in Dark and Bright Modes of a Finite-Sized Plasmonic Lattice. *Nat. Commun.* **2017**, *8* (1), 13687. https://doi.org/10.1038/ncomms13687.

(117) Offermans, P.; Schaafsma, M. C.; Rodriguez, S. R. K.; Zhang, Y.; Crego-Calama, M.; Brongersma, S. H.; Gómez Rivas, J. Universal Scaling of the Figure of Merit of Plasmonic Sensors. *ACS Nano* **2011**, *5* (6), 5151–5157. https://doi.org/10.1021/nn201227b.

(118) Danilov, A.; Tselikov, G.; Wu, F.; Kravets, V. G.; Ozerov, I.; Bedu, F.; Grigorenko, A. N.; Kabashin, A. V. Ultra-Narrow Surface Lattice Resonances in Plasmonic Metamaterial Arrays for Biosensing Applications. *Biosens. Bioelectron.* **2018**, *104*, 102–112. https://doi.org/10.1016/j.bios.2017.12.001.

(119) Guo, K.; Lozano, G.; Verschuuren, M. A.; Gómez Rivas, J. Control of the External Photoluminescent Quantum Yield of Emitters Coupled to Nanoantenna Phased Arrays. *J. Appl. Phys.* **2015**, *118* (7), 073103. https://doi.org/10.1063/1.4928616.

(120) Lozano, G.; Louwers, D. J.; Rodríguez, S. R.; Murai, S.; Jansen, O. T.; Verschuuren, M. A.; Gómez Rivas, J. Plasmonics for Solid-State Lighting: Enhanced Excitation and Directional Emission of Highly Efficient Light Sources. *Light Sci. Appl.* **2013**, *2* (5), e66–e66. https://doi.org/10.1038/lsa.2013.22.

(121) Wang, H.; Wang, X.; Yan, C.; Zhao, H.; Zhang, J.; Santschi, C.; Martin, O. J. F. Full Color Generation Using Silver Tandem Nanodisks. *ACS Nano* **2017**, *11* (5), 4419–4427. https://doi.org/10.1021/acsnano.6b08465.

(122) Si, G.; Zhao, Y.; Lv, J.; Lu, M.; Wang, F.; Liu, H.; Xiang, N.; Huang, T. J.; Danner, A. J.; Teng, J.; Liu, Y. J. Reflective Plasmonic Color Filters Based on Lithographically Patterned Silver Nanorod Arrays. *Nanoscale* **2013**, *5* (14), 6243. https://doi.org/10.1039/c3nr01419c.

(123) Linden, S.; Kuhl, J.; Giessen, H. Controlling the Interaction between Light and Gold Nanoparticles: Selective Suppression of Extinction. *Phys. Rev. Lett.* **2001**, *86* (20), 4688–4691. https://doi.org/10.1103/PhysRevLett.86.4688.

(124) Rodriguez, S. R. K.; Chen, Y. T.; Steinbusch, T. P.; Verschuuren, M. A.; Koenderink, A. F.; Rivas, J. G. From Weak to Strong Coupling of Localized Surface Plasmons to Guided Modes in a Luminescent Slab. *Phys. Rev. B* **2014**, *90* (23), 235406. https://doi.org/10.1103/PhysRevB.90.235406.

(125) Zhou, W.; Suh, J. Y.; Hua, Y.; Odom, T. W. Hybridization of Localized and Guided Modes in 2D Metal–Insulator–Metal Nanocavity Arrays. *J. Phys. Chem. C* **2013**, *117* (6), 2541–2546. https://doi.org/10.1021/jp306972j.

(126) Kamakura, R.; Murai, S.; Ishii, S.; Nagao, T.; Fujita, K.; Tanaka, K. Plasmonic–Photonic Hybrid Modes Excited on a Titanium Nitride Nanoparticle Array in the Visible Region. *ACS Photonics* **2017**, *4* (4), 815–822. https://doi.org/10.1021/acsphotonics.6b00763.

(127) Nguyen-Huu, N.; Lo, Y.-L.; Chen, Y.-B. Color Filters Featuring High Transmission Efficiency and Broad Bandwidth Based on Resonant Waveguide-Metallic Grating. *Opt. Commun.* **2011**, *284* (10–11), 2473–2479. https://doi.org/10.1016/j.optcom.2011.01.035.

(128) Bauer, C.; Giessen, H. Tailoring the Plasmonic Fano Resonance in Metallic Photonic Crystals. *Nanophotonics* **2020**, *9* (2), 523–531. https://doi.org/10.1515/nanoph-2019-0335.

(129) Zhang, X.; Ma, X.; Dou, F.; Zhao, P.; Liu, H. A Biosensor Based on Metallic Photonic Crystals for the Detection of Specific Bioreactions. *Adv. Funct. Mater.* **2011**, *21* (22), 4219–4227. https://doi.org/10.1002/adfm.201101366.

(130) Xu, Y.; Bai, P.; Zhou, X.; Akimov, Y.; Png, C. E.; Ang, L.; Knoll, W.; Wu, L. Optical Refractive Index Sensors with Plasmonic and Photonic Structures: Promising and Inconvenient Truth. *Adv. Opt. Mater.* **2019**, *7* (9), 1801433. https://doi.org/10.1002/adom.201801433.

(131) Juodėnas, M.; Tamulevičius, T.; Henzie, J.; Erts, D.; Tamulevičius, S. Surface Lattice Resonances in Self-Assembled Arrays of Monodisperse Ag Cuboctahedra. *ACS Nano* **2019**, *13* (8), 9038–9047. https://doi.org/10.1021/acsnano.9b03191.

(132) Ross, M. B.; Ku, J. C.; Blaber, M. G.; Mirkin, C. A.; Schatz, G. C. Defect Tolerance and the Effect of Structural Inhomogeneity in Plasmonic DNA-Nanoparticle Superlattices. *Proc. Natl. Acad. Sci.* **2015**, *112* (33), 10292–10297. https://doi.org/10.1073/pnas.1513058112.

(133) Gupta, V.; Probst, P. T.; Goßler, F. R.; Steiner, A. M.; Schubert, J.; Brasse, Y.; König, T. A. F.; Fery, A. Mechanotunable Surface Lattice Resonances in the Visible Optical Range by Soft Lithography Templates and Directed Self-Assembly. *ACS Appl Mater Interfaces* **2019**, 8.

(134) Auguié, B.; Barnes, W. L. Diffractive Coupling in Gold Nanoparticle Arrays and the Effect of Disorder. *Opt. Lett.* **2009**, *34* (4), 401. https://doi.org/10.1364/OL.34.000401.

(135) Nishijima, Y.; Khurgin, J. B.; Rosa, L.; Fujiwara, H.; Juodkazis, S. Randomization of Gold Nano-Brick Arrays: A Tool for SERS Enhancement. *Opt. Express* **2013**, *21* (11), 13502. https://doi.org/10.1364/OE.21.013502.

(136) Ponomareva, E.; Volk, K.; Mulvaney, P.; Karg, M. Surface Lattice Resonances in Self-Assembled Gold Nanoparticle Arrays: Impact of Lattice Period, Structural Disorder, and Refractive Index on Resonance Quality. *Langmuir* **2020**, *36* (45), 13601–13612. https://doi.org/10.1021/acs.langmuir.0c02430.

(137) Schokker, A. H.; Koenderink, A. F. Statistics of Randomized Plasmonic Lattice Lasers. *ACS Photonics* **2015**, *2* (9), 1289–1297. https://doi.org/10.1021/acsphotonics.5b00226.

(138) Zhang, F.; Tang, F.; Xu, X.; Adam, P.-M.; Martin, J.; Plain, J. Influence of Order-to-Disorder Transitions on the Optical Properties of the Aluminum Plasmonic Metasurface. *Nanoscale* **2020**, *12* (45), 23173–23182. https://doi.org/10.1039/D0NR06334G.

(139) Nadar, L.; Destouches, N.; Crespo-Monteiro, N.; Sayah, R.; Vocanson, F.; Reynaud, S.; Lefkir, Y.; Capoen, B. Multicolor Photochromism of Silver-Containing Mesoporous Films of Amorphous or Anatase TiO2. *J. Nanoparticle Res.* **2013**, *15* (11), 2048. https://doi.org/10.1007/s11051-013-2048-9.

(140) Nadar, L.; Sayah, R.; Vocanson, F.; Crespo-Monteiro, N.; Boukenter, A.; Joao, S. S.; Destouches, N. Influence of Reduction Processes on the Colour and Photochromism of Amorphous Mesoporous TiO2 Thin Films Loaded with a Silver Salt. *Photochem. Photobiol. Sci.* **2011**, *10* (11), 1810–1816. https://doi.org/10.1039/c1pp05172e.

(141) *CIELAB color space*. wikipedia. https://en.wikipedia.org/wiki/CIELAB_color_space.

(142) *CIE 1931 color space*. wikipedia. https://en.wikipedia.org/wiki/CIE_1931_color_space.

(143) Sarkar, S.; Gupta, V.; Kumar, M.; Schubert, J.; Probst, P. T.; Joseph, J.; König, T. A. F. Hybridized Guided-Mode Resonances via Colloidal Plasmonic Self-Assembled Grating. *ACS Appl. Mater. Interfaces* **2019**, *11* (14), 13752–13760. https://doi.org/10.1021/acsami.8b20535.

(144) Zhukovsky, S. V.; Babicheva, V. E.; Uskov, A. V.; Protsenko, I. E.; Lavrinenko, A. V. Enhanced Electron Photoemission by Collective Lattice Resonances in Plasmonic Nanoparticle-Array Photodetectors and Solar Cells. *Plasmonics* **2014**, *9* (2), 283–289. https://doi.org/10.1007/s11468-013-9621-z.

(145) Koo, W. H.; Youn, W.; Zhu, P.; Li, X.-H.; Tansu, N.; So, F. Light Extraction of Organic Light Emitting Diodes by Defective Hexagonal-Close-Packed Array. *Adv. Funct. Mater.* **2012**, *22* (16), 3454–3459. https://doi.org/10.1002/adfm.201200876.

(146) Lozano, G.; Grzela, G.; Verschuuren, M. A.; Ramezani, M.; Rivas, J. G. Tailor-Made Directional Emission in Nanoimprinted Plasmonic-Based Light-Emitting Devices. *Nanoscale* **2014**, *6*, 9223–9229.

(147) Koirala, I.; Shrestha, V. R.; Park, C.-S.; Lee, S.-S.; Choi, D.-Y. Polarization-Controlled Broad Color Palette Based on an Ultrathin One-Dimensional Resonant Grating Structure. *Sci. Rep.* **2017**, *7* (1), 40073. https://doi.org/10.1038/srep40073.

(148) Khlopin, D.; Laux, F.; Wardley, W. P.; Martin, J.; Wurtz, G. A.; Plain, J.; Bonod, N.; Zayats, A. V.; Dickson, W.; Gérard, D. Lattice Modes and Plasmonic Linewidth Engineering in Gold and Aluminum Nanoparticle Arrays. *J. Opt. Soc. Am. B* **2017**, *34* (3), 691. https://doi.org/10.1364/JOSAB.34.000691.

(149) Zhu, X.; Yan, W.; Levy, U.; Mortensen, N. A.; Kristensen, A. Resonant Laser Printing of Structural Colors on High-Index Dielectric Metasurfaces. *Sci. Adv.* **2017**, *3* (5), e1602487. https://doi.org/10.1126/sciadv.1602487.

(150) Volk, K.; Fitzgerald, J. P. S.; Ruckdeschel, P.; Retsch, M.; König, T. A. F.; Karg, M. Reversible Tuning of Visible Wavelength Surface Lattice Resonances in Self-Assembled Hybrid Monolayers. *Adv. Opt. Mater.* **2017**, *5* (9), 1600971. https://doi.org/10.1002/adom.201600971.

(151) Mayer, M.; Schnepf, M. J.; König, T. A. F.; Fery, A. Colloidal Self-Assembly Concepts for Plasmonic Metasurfaces. *Adv. Opt. Mater.* **2019**, *7* (1), 1800564. https://doi.org/10.1002/adom.201800564.

(152) Destouches, N.; Martínez-García, J.; Hébert, M.; Crespo-Monteiro, N.; Vitrant, G.; Liu, Z.; Trémeau, A.; Vocanson, F.; Pigeon, F.; Reynaud, S.; Lefkir, Y. Dichroic Colored Luster of Laser-Induced Silver Nanoparticle Gratings Buried in Dense Inorganic Films. *J. Opt. Soc. Am. B* **2014**, *31* (11), C1. https://doi.org/10.1364/JOSAB.31.0000C1.

(153) Liu, Z.; Epicier, T.; Lefkir, Y.; Vitrant, G.; Destouches, N. HAADF-STEM Characterization and Simulation of Nanoparticle Distributions in an Inhomogeneous Matrix: STEM OF NPs

IN AN INHOMOGENEOUS MATRIX. *J. Microsc.* **2017**, *266* (1), 60–68. https://doi.org/10.1111/jmi.12519.

(154) Liu, Z.; Vitrant, G.; Lefkir, Y.; Bakhti, S.; Destouches, N. Laser Induced Mechanisms Controlling the Size Distribution of Metallic Nanoparticles. *Phys. Chem. Chem. Phys.* **2016**, *18* (35), 24600–24609. https://doi.org/10.1039/C6CP03415B.

(155) Eilers, P. H. C. A Perfect Smoother. *Anal. Chem.* **2003**, *75* (14), 3631–3636. https://doi.org/10.1021/ac034173t.

(156) He, S.; Zhang, W.; Liu, L.; Huang, Y.; He, J.; Xie, W.; Wu, P.; Du, C. Baseline Correction for Raman Spectra Using an Improved Asymmetric Least Squares Method. *Anal Methods* **2014**, *6* (12), 4402–4407. https://doi.org/10.1039/C4AY00068D.

(157) Wokaun, A.; Gordon, J. P.; Liao, P. F. Radiation Damping in Surface-Enhanced Raman Scattering. *Phys. Rev. Lett.* **1982**, *48* (14), 957–960. https://doi.org/10.1103/PhysRevLett.48.957.

(158) Amra, C.; Lequime, M.; Zerrad, M. *Electromagnetic Optics of Thin-Film Coatings: Light Scattering, Giant Field Enhancement, and Planar Microcavities*, 1st ed.; Cambridge University Press, 2020. https://doi.org/10.1017/9781108772372.

(159) Cheng, F.; Gao, J.; Luk, T. S.; Yang, X. Structural Color Printing Based on Plasmonic Metasurfaces of Perfect Light Absorption. *Sci. Rep.* **2015**, *5* (1), 11045. https://doi.org/10.1038/srep11045.

(160) Duempelmann, L.; Casari, D. Color Rendering Plasmonic Aluminum Substrates with Angular Symmetry Breaking. *ACS Nano* **2015**, *9* (12), 12383–12391. https://doi.org/doi.org/10.1021/acsnano.5b05710.

(161) Jiang, H.; Kaminska, B. Scalable Inkjet-Based Structural Color Printing by Molding Transparent Gratings on Multilayer Nanostructured Surfaces. *ACS Nano* **2018**, *12* (4), 3112–3125. https://doi.org/10.1021/acsnano.7b08580.

(162) Clausen, J. S.; Højlund-Nielsen, E.; Christiansen, A. B.; Yazdi, S.; Grajower, M.; Taha, H.; Levy, U.; Kristensen, A.; Mortensen, N. A. Plasmonic Metasurfaces for Coloration of Plastic Consumer Products. *Nano Lett.* **2014**, *14* (8), 4499–4504. https://doi.org/10.1021/nl5014986.

(163) Caligiuri, V.; Patra, A.; De Santo, M. P.; Forestiero, A.; Papuzzo, G.; Aceti, D. M.; Lio, G. E.; Barberi, R.; De Luca, A. Hybrid Plasmonic/Photonic Nanoscale Strategy for Multilevel Anticounterfeit Labels. *ACS Appl. Mater. Interfaces* **2021**, *13* (41), 49172–49183. https://doi.org/10.1021/acsami.1c13701.

(164) Liu, H.; Xu, J.; Wang, H.; Liu, Y.; Ruan, Q.; Wu, Y.; Liu, X.; Yang, J. K. W. Tunable Resonator-Upconverted Emission (TRUE) Color Printing and Applications in Optical Security. *Adv. Mater.* **2019**, *31* (15), 1807900. https://doi.org/10.1002/adma.201807900.

(165) Hong, W.; Yuan, Z.; Chen, X. Structural Color Materials for Optical Anticounterfeiting. *Small* **2020**, *16* (16), 1907626. https://doi.org/10.1002/smll.201907626.

(166) Duempelmann, L.; Luu-Dinh, A.; Gallinet, B.; Novotny, L. Four-Fold Color Filter Based on Plasmonic Phase Retarder. *ACS Photonics* **2016**, *3* (2), 190–196. https://doi.org/10.1021/acsphotonics.5b00604.

(167) Mohammadi, R.; Ochs, M.; Andrieu-Brunsen, A.; Vogel, N. Effect of Asymmetry on Plasmon Hybridization and Sensing Capacities of Hole-Disk Arrays. *J. Phys. Chem. C* **2020**, *124* (4), 2609–2618. https://doi.org/10.1021/acs.jpcc.9b10229.

(168) Ng, R. J. H.; Krishnan, R. V.; Wang, H.; Yang, J. K. W. Darkfield Colors from Multi-Periodic Arrays of Gap Plasmon Resonators. *Nanophotonics* **2020**, *9* (2), 533–545. https://doi.org/10.1515/nanoph-2019-0414.

(169) Manzano, C. V.; Ramos, D.; Pethö, L.; Bürki, G.; Michler, J.; Philippe, L. Controlling the Color and Effective Refractive Index of Metal-Anodic Aluminum Oxide (AAO)–Al Nanostructures: Morphology of AAO. *J. Phys. Chem. C* **2018**, *122* (1), 957–963. https://doi.org/10.1021/acs.jpcc.7b11131.

(170) Zhu, X.; Vannahme, C.; Højlund-Nielsen, E.; Mortensen, N. A.; Kristensen, A. Plasmonic Colour Laser Printing. *Nat. Nanotechnol.* **2016**, *11* (4), 325–329. https://doi.org/10.1038/nnano.2015.285.

(171) Zhang, Y.; Liang, Z.; Zhang, A. P.; Tam, H. Direct Printing of Micropatterned Plasmonic Substrates of Size-Controlled Gold Nanoparticles by Precision Photoreduction. *Adv. Opt. Mater.* **2021**, *9* (1), 2001368. https://doi.org/10.1002/adom.202001368.

(172) Wang, Y.; Ren, F.; Ding, T. Generation of High Quality, Uniform and Stable Plasmonic Colorants via Laser Direct Writing. *Adv. Opt. Mater.* **2020**, *8* (12), 2000164. https://doi.org/10.1002/adom.202000164.

(173) Andreeva, Ya. M.; Luong, V. C.; Lutoshina, D. S.; Medvedev, O. S.; Mikhailovskii, V. Yu.; Moskvin, M. K.; Odintsova, G. V.; Romanov, V. V.; Shchedrina, N. N.; Veiko, V. P. Laser Coloration of Metals in Visual Art and Design. *Opt. Mater. Express* **2019**, *9* (3), 1310. https://doi.org/10.1364/OME.9.001310.

(174) Tsai, C.-Y.; Lin, J.-W.; Wu, C.-Y.; Lin, P.-T.; Lu, T.-W.; Lee, P.-T. Plasmonic Coupling in Gold Nanoring Dimers: Observation of Coupled Bonding Mode. *Nano Lett.* **2012**, *12* (3), 1648–1654. https://doi.org/10.1021/nl300012m.

(175) Yang, S.-C.; Kobori, H.; He, C.-L.; Lin, M.-H.; Chen, H.-Y.; Li, C.; Kanehara, M.; Teranishi, T.; Gwo, S. Plasmon Hybridization in Individual Gold Nanocrystal Dimers: Direct Observation of Bright and Dark Modes. *Nano Lett.* **2010**, *10* (2), 632–637. https://doi.org/10.1021/nl903693v.

(176) Jain, P. K.; Huang, W.; El-Sayed, M. A. On the Universal Scaling Behavior of the Distance Decay of Plasmon Coupling in Metal Nanoparticle Pairs: A Plasmon Ruler Equation. *Nano Lett.* **2007**, *7* (7), 2080–2088. https://doi.org/10.1021/nl071008a.

(177) Bakhti, S.; Destouches, N.; Tishchenko, A. V. Coupled Mode Modeling To Interpret Hybrid Modes and Fano Resonances in Plasmonic Systems. *ACS Photonics* **2015**, *2* (2), 246–255. https://doi.org/10.1021/ph500356n.

(178) Loewen, E. G.; Popov, E. *Diffraction Gratings and Applications*; Optical engineering; Dekker: New York, NY, 1997.

(179) Bonod, N.; Neauport, J. Diffraction Gratings: From Principles to Applications in High-Intensity Lasers. *Adv. Opt. Photonics* **2016**, *8* (1), 156. https://doi.org/10.1364/AOP.8.000156.

(180) Moreno, I.; Davis, J. A.; Pascoguin, B. M. L.; Mitry, M. J.; Cottrell, D. M. Vortex Sensing Diffraction Gratings. 3.

(181) Sahoo, P. K.; Sarkar, S.; Joseph, J. High Sensitivity Guided-Mode-Resonance Optical Sensor Employing Phase Detection. *Sci. Rep.* **2017**, *7* (1), 7607. https://doi.org/10.1038/s41598-017-07843-z.

(182) Li, X.; Tang, B.; Wu, B.; Hsu, C.; Wang, X. Highly Sensitive Diffraction Grating of Hydrogels as Sensors for Carbon Dioxide Detection. *Ind. Eng. Chem. Res.* **2021**, *60* (12), 4639–4649. https://doi.org/10.1021/acs.iecr.1c00211.

(183) Rößler, F.; Kunze, T.; Lasagni, A. F. Fabrication of Diffraction Based Security Elements Using Direct Laser Interference Patterning. *Opt. Express* **2017**, *25* (19), 22959. https://doi.org/10.1364/OE.25.022959.

(184) Song, Q.; Pigeon, Y. E.; Heggarty, K. Faceted Gratings for an Optical Security Feature. *Appl. Opt.* **2020**, *59* (4), 910. https://doi.org/10.1364/AO.378122.

(185) Park, S.; Won Hahn, J. Plasmonic Data Storage Medium with Metallic Nano-Aperture Array Embedded in Dielectric Material. *Opt. Express* **2009**, *17* (22), 20203. https://doi.org/10.1364/OE.17.020203.

(186) Zheng, J.; Ye, Z.-C.; Sun, N.-L.; Zhang, R.; Sheng, Z.-M.; Shieh, H.-P. D.; Zhang, J. Highly Anisotropic Metasurface: A Polarized Beam Splitter and Hologram. *Sci. Rep.* **2015**, *4* (1), 6491. https://doi.org/10.1038/srep06491.

(187) Huang, L.; Chen, X.; Mühlenbernd, H.; Zhang, H.; Chen, S.; Bai, B.; Tan, Q.; Jin, G.; Cheah, K.-W.; Qiu, C.-W.; Li, J.; Zentgraf, T.; Zhang, S. Three-Dimensional Optical Holography Using a Plasmonic Metasurface. *Nat. Commun.* **2013**, *4* (1), 2808. https://doi.org/10.1038/ncomms3808.

(188) Tamulevičius, T.; Juodėnas, M.; Klinavičius, T.; Paulauskas, A.; Jankauskas, K.; Ostreika, A.; Žutautas, A.; Tamulevičius, S. Dot-Matrix Hologram Rendering Algorithm and Its Validation through Direct Laser Interference Patterning. *Sci. Rep.* **2018**, *8* (1), 14245. https://doi.org/10.1038/s41598-018-32294-5.

(189) Yang, L.; Karlsson, M. Effective Method for Fast and Detailed Analysis of Holographic Patterns over a Large Area. *Appl. Opt.* **2017**, *56* (26), 7491. https://doi.org/10.1364/AO.56.007491.

(190) Mu, C.-T.; Chen, C.-H. Diffractive Distortion of a Pixelated Computer-Generated Hologram with Oblique Illumination. *Appl. Opt.* **2020**, *59* (24), 7153. https://doi.org/10.1364/AO.394650.

(191) Su, Y.; Cai, Z.; Wu, K.; Shi, L.; Zhou, F.; Chen, H.; Wu, J. Projection-Type Multiview Holographic Three-Dimensional Display Using a Single Spatial Light Modulator and a Directional Diffractive Device. *IEEE Photonics J.* **2018**, *10* (5), 1–12. https://doi.org/10.1109/JPHOT.2018.2871936.

(192) Bonod, N.; Popov, E.; Li, L.; Chernov, B. Unidirectional Excitation of Surface Plasmons by Slanted Gratings. *Opt. Express* **2007**, *15* (18), 11427. https://doi.org/10.1364/OE.15.011427.

(193) Lima, C. R. A.; Soares, L. L.; Cescato, L.; Gobbi, A. L. Reflecting Polarizing Beam Splitter. *Opt. Lett.* **1997**, *22* (4), 203. https://doi.org/10.1364/OL.22.000203.

(194) Yu, H.; Duerr, G.; Huber, R.; Bahr, M.; Schwarze, T.; Brandl, F.; Grundler, D. Omnidirectional Spin-Wave Nanograting Coupler. *Nat. Commun.* **2013**, *4* (1), 2702. https://doi.org/10.1038/ncomms3702.

(195) Bonse, J.; Gräf, S. Maxwell Meets Marangoni—A Review of Theories on Laser-Induced Periodic Surface Structures. *Laser Photonics Rev.* **2020**, *14* (10), 2000215. https://doi.org/10.1002/lpor.202000215.

(196) Ageev, E. I.; Veiko, V. P.; Vlasova, E. A.; Karlagina, Y. Y.; Krivonosov, A.; Moskvin, M. K.; Odintsova, G. V.; Pshenichnov, V. E.; Romanov, V. V.; Yatsuk, R. M. Controlled Nanostructures Formation on Stainless Steel by Short Laser Pulses for Products Protection against Falsification. *Opt. Express* **2018**, *26* (2), 2117. https://doi.org/10.1364/OE.26.002117.

(197) Jwad, T.; Penchev, P.; Nasrollahi, V.; Dimov, S. Laser Induced Ripples' Gratings with Angular Periodicity for Fabrication of Diffraction Holograms. *Appl. Surf. Sci.* **2018**, *453*, 449–456. https://doi.org/10.1016/j.apsusc.2018.04.277.

(198) Hamad, S.; Bharati Moram, S. S.; Yendeti, B.; Podagatlapalli, G. K.; Nageswara Rao, S. V. S.; Pathak, A. P.; Mohiddon, M. A.; Soma, V. R. Femtosecond Laser-Induced, Nanoparticle-Embedded Periodic Surface Structures on Crystalline Silicon for Reproducible and Multi-Utility SERS Platforms. *ACS Omega* **2018**, *3* (12), 18420–18432. https://doi.org/10.1021/acsomega.8b02629.

(199) Heitz, J.; Plamadeala, C.; Muck, M.; Armbruster, O.; Baumgartner, W.; Weth, A.; Steinwender, C.; Blessberger, H.; Kellermair, J.; Kirner, S. V.; Krüger, J.; Bonse, J.; Guntner, A. S.; Hassel, A. W. Femtosecond Laser-Induced Microstructures on Ti Substrates for Reduced Cell Adhesion. *Appl. Phys. A* **2017**, *123* (12), 734. https://doi.org/10.1007/s00339-017-1352-0.

(200) Lange, K.; Schulz-Ruhtenberg, M.; Caro, J. Platinum Electrodes for Oxygen Reduction Catalysis Designed by Ultrashort Pulse Laser Structuring. *ChemElectroChem* **2017**, *4* (3), 570–576. https://doi.org/10.1002/celc.201600630.

(201) Huang, C.; Bell, R.; Tsubaki, A.; Zuhlke, C. A.; Alexander, D. R. Condensation and Subsequent Freezing Delays as a Result of Using Femtosecond Laser Functionalized Surfaces. *J. Laser Appl.* **2018**, *30* (1), 011501. https://doi.org/10.2351/1.4986058.

(202) Crespo-Monteiro, N.; Destouches, N.; Epicier, T.; Balan, L.; Vocanson, F.; Lefkir, Y.; Michalon, J.-Y. Changes in the Chemical and Structural Properties of Nanocomposite

Ag:TiO $_2$ Films during Photochromic Transitions. *J. Phys. Chem. C* **2014**, *118* (41), 24055–24061. https://doi.org/10.1021/jp505702g.

(203) Moharam, M. G.; Gaylord, T. K.; Grann, E. B.; Pommet, D. A. Formulation for Stable and Efficient Implementation of the Rigorous Coupled-Wave Analysis of Binary Gratings. *J. Opt. Soc. Am. A* **1995**, *12* (5), 1068. https://doi.org/10.1364/JOSAA.12.001068.

(204) Rumpf, R. C. IMPROVED FORMULATION OF SCATTERING MATRICES FOR SEMI-ANALYTICAL METHODS THAT IS CONSISTENT WITH CONVENTION. *Prog. Electromagn. Res. B* **2011**, *35*, 241–261. https://doi.org/10.2528/PIERB11083107.

(205) Harvey, J. E.; Pfisterer, R. N. Understanding Diffraction Grating Behavior: Including Conical Diffraction and Rayleigh Anomalies from Transmission Gratings. *Opt. Eng.* **2019**, *58* (08), 1. https://doi.org/10.1117/1.OE.58.8.087105.

(206) Harvey, J. E.; Vernold, C. L. Description of Diffraction Grating Behavior in Direction Cosine Space. *Appl. Opt.* **1998**, *37* (34), 8158. https://doi.org/10.1364/AO.37.008158.

List of publications

Peer-reviewed articles

• N. Dalloz, V. D. Le, M. Hebert, B. Eles, M. A. Flores Figueroa, C. Hubert, H. Ma, N. Sharma, F. Vocanson, S. Ayala, N. Destouches, « Anti-Counterfeiting White Light Printed Image Multiplexing by Fast Nanosecond Laser Processing », Adv. Mater. 2022, 34, 2104054.

• V. D. Le, B. Eles, N. Dalloz, M. A. Flores Figueroa, F. Vocanson, C. Hubert, N. Destouches, « Understanding and exploiting the laser-induced optical properties of quasi-random plasmonic metasurfaces », in revision.

• V. D. Le, Y. Lefkir, N. Destouches «Hybridization between plasmonic and photonic modes in laser-induced self-organized quasi-random plasmonic metasurfaces» submitted

• V. D. Le, J-P. Colombier, F. Vocanson, C. Hubuer, N. Destouches « Optical diffraction properties of three-superimposed self-organized nanostructures induced by laser process » to be submitted

Patent

S. Ayala, N. Destouches, M. Hébert, N. Dalloz, V. D. Le, "Method of generating a palette for use in a printing process and printing method", submitted on 14/03/2023 under the number 23315050.7

Conference Proceeding

• V. D. Le, B. Eles, N. Dalloz, M. A. Flores Figueroa, F. Vocanson, Y. Lefkir, N. Destouches, « Direct color printing on Ag: TiO_2 thin films induced by nanosecond laser pulses », Proc. SPIE, 12202, Nanoengineering: Fabrication, Properties, Optics, Thin Films, and Devices XIX, 1220207 (3 October 2022); doi.org/10.1117/12.2632435

International Conference

• V. D. Le, Y. Lefkir, N. Destouches, « Laser induced self-organized quasi-random plasmonic nanomaterials: hybridization of plasmonic and photonic modes », Nanophotonics and Micro/Nano

Optics International Conference 2022 (Nanop 2022), 25-27 October 2022, Paris, France (Presentation)

- N. Dalloz, V. D. Le, M. Hebert, B. Eles, M. A. Flores Figueroa, C. Hubert, H. Ma, N. Sharma, F. Vocanson, S. Ayala, N. Destouches, « Anti-counterfeiting laser printing on plasmonic metasurfaces », International Sol-Gel Conference Solgel 2022, 24 – 29 July 2022, Lyon, France. (Poster)

- M. A. Flores Figueroa, N. Dalloz, F. Vocanson, V. D. Le, M. Hebert, B. Eles, C. Hubert, H. Ma, N. Sharma, S. Ayala, N. Destouches, « Color multiplexed images printed on plasmonic TiO2: Ag nanocomposite films », International Sol-Gel Conference Solgel 2022, 24 – 29 July 2022, Lyon, France. (Poster)

- V. D. Le, B. Eles, N. Dalloz, M. A. Flores Figueroa, F. Vocanson, N. Destouches, « Controlling diffraction and dichroism of plasmonic metamaterials with nanosecond laser pulses », 12th International Conference on Metamaterials (META 2022), Torremolinos, Spain, July 19 - 22, 2022. (Poster)

- V. D. Le, N. Destouches, « Mode coupling in laser-induced self-organized quasi-random metallic nanoparticles arrays embedded in thin films », 5th International Workshop on Metallic Nano-Objects (MNO 2021), Saint-Etienne, France, November 17 - 19, 2021. (Presentation)

- V. D. Le, Colombier, J.P, N. Destouches, « Circular diffraction produced by three superimposed self-organized periodic patterns », 5th International Workshop on Metallic Nano-Objects (MNO 2021), Saint-Etienne, France, November 17 - 19, 2021. (Poster)

- V. D. Le, Bakhti. S, N. Destouches, « Optical Properties of Self-Organized Ag/TiO2 Composite Illuminated by Continuous Light Wave », Paris-Saclay/ Munich Summer School on Surface Plasmons (PSM-SP), Paris, France, July 12 - 16, 2021. (Poster)

- V. D. Le, Bakhti. S, N. Destouches, « Asymmetric optical behavior of nanocomposite Ag/TiO_2 films induced by continuous laser », *Colloquium on The Physics and Applications of Metasurfaces*, Corsica, France, June 14 - 18, 2021. (Poster)

National Conference

- V. D. Le, B. Eles, N. Dalloz, M. A. Flores Figueroa, F. Vocanson, Y. Lefkir, N. Destouches, « Controlling dichroism, diffraction and colors of nanomaterials with laser processing », C'Nano, Poitiers, France, March 15 - 17, 2023. (Poster)

- V. D. Le, B. Eles, M. A. Flores Figueroa, F. Vocanson, Y. Lefkir, N. Destouches, « Métamatériaux plasmoniques auto-organisés quasi-aléatoires induits par laser : l'effet optique asymétrique », French Photonics Day, 20-21 October 2022, Saint Etienne, France. (Poster)

- N. Sharma, N. Dalloz, V. D. Le, B. Eles, M. Hébert and N. Destouches, "Optical properties and applications of laser-induced random plasmonic metasurfaces", Journées plénières 2021 du GDR Plasmonique Active, 28-29 Jun., 2021, Troyes (oral)